IMPROVING THE THERMOELECTRIC PERFORMANCE OF POLYMER NANOCOMPOSITE THIN FILMS

A Dissertation

by

DANIEL LAWRENCE STEVENS

Submitted to the Office of Graduate and Professional Studies of
Texas A&M University
in partial fulfillment of the requirements for the degree of

DOCTOR OF PHILOSOPHY

Chair of Committee,	Jaime C. Grunlan
Committee Members,	Sarbajit Banerjee
	Matthew T. Sheldon
	Jodie Lutkenhaus
Head of Department,	Simon W. North

December 2020

Major Subject: Chemistry

Copyright 2020 Daniel L. Stevens

ABSTRACT

Thermoelectricity is a promising alternative energy generation method as it captures dissipated thermal energy and converts it into useful electrical energy. The most common thermoelectric materials are inorganic semiconductors, but these compounds have issues of scarcity, toxicity and mechanical rigidity. In an effort to create good performing thermoelectrics, while combatting the issues faced with traditional materials, polymer nanocomposites comprised of carbonaceous nanofillers (*i.e.* carbon nanotubes and graphene) and conducting polymers have been prepared using layer-by-layer assembly. While films deposited using layer-by-layer assembly exhibit good thermoelectric performance, there is a limited number of strategies to improve these materials other than selecting different film constituents. This dissertation describes two novel strategies – post-deposition thermal treatment and salt doping – to improve the thermoelectric performance of these films that could aid in the realization of organic thermoelectric devices at low operating temperatures.

DEDICATION

This dissertation is dedicated to my mother, Uncle Dan, brother, and friends for their support throughout this chapter in my life.

ACKNOWLEDGEMENTS

I would like to express my gratitude to my Ph.D. advisor, Dr. Jaime Grunlan, for his feedback in my research directions and investment into helping me develop as a scientist. I would have been unable to complete my degree in this timeframe without his guidance. Next, I would like to thank my committee members, Dr. Sarbajit Banerjee, Dr. Matthew T. Sheldon, and Dr. Jodie Lutkenhaus, for their expert opinion and scrutiny on my research. I am especially thankful to Dr. Banerjee who let me use his equipment to help portions of my research described in this dissertation. I am especially thankful for Geethal Gamage and Dr. Zhifeng Ren, our collaborators at the University of Houston, who helped complete Hall Effect and temperature-dependent transport studies that helped make my research of much better quality.

I am very thankful for the various graduate students, post-docs, and visiting professors I have had the pleasure to interact with during my time in Dr. Grunlan's group. I am thankful for the friendship and scientific discussion that each of them provided in my developing career. I am thankful for the undergraduates – Aaron Parra and Adrian Ortiz – for their hard work and dedication on my research projects. I would not be where I am today without the help of a supportive group and hardworking undergraduates. I would also like to thank my undergraduate research mentor – Dr. Mary E. Anderson – who initially sparked my interest in scientific research. Her mentorship (and patience) made my first research experience more rewarding than I could have possibly imagined.

Last, but certainly not least, I would like to thank my family and friends. In particular, I could not have completed my degree without the love and support from my mother and uncle.

They were always there for me when I needed it most, and I am forever thankful for them. I would like to thank to my friends here I have made during my time in College Station. The relationships we have built I believe are ones to last a lifetime. I would also like to thank my friends back in Michigan for their friendship and support during this time. If it were not for everyone mentioned in this acknowledgement section, I would not be the position I am in today.

CONTRIBUTORS AND FUNDING SOURCES

Contributors

This dissertation was supported by a doctoral committee comprised of Professor Jaime C. Grunlan as advisor, Professors Sarbajit Banerjee and Matthew Sheldon of the Department of Chemistry, and Professor Jodie Lutkenhaus of the Department of Chemical Engineering.

Collaborative work discussed in Chapters IV and V were accomplished with Professor Zhifeng Ren and his student, Geethal Gamage, who are affiliated with the Texas Center of Superconductivity at the University of Houston. Aaron Parra helped prepare samples and measure their thermoelectric properties in the research described in Chapter III, and Adrian Ortiz prepared samples and measured the film thickness and thermoelectric properties in the research described in Chapter V.

Funding Sources

The doctoral research presented here was supported by Texas A&M Engineering Experiment Station (TEES) and the Texas A&M Research Development Fund (RDF).

TABLE OF CONTENTS

LIST OF FIGURES

Page

LIST OF TABLES

Page

CHAPTER I

INTRODUCTION

1.1 Background

Renewable energy technologies are receiving significant attention in order to meet our global energy demands from our increasing standard of living that is estimated to be in upwards of 48% by 2040.[1] In 2019, approximately 100 quadrillion Btu of energy was produced in the United States alone, with 80% coming from fossil fuels.[2] In the consumption of fossil fuels, a majority of the generated energy is dissipated as waste heat. The transportation and industrial sectors result in the excessive waste heat for this reason. As of 2018, 68% of generated energy was being wasted as heat, , which is a major issue due to the aforementioned global energy demand.[2–4]

Alternative energy sources only make up 11% of the total energy being generated, which is comprised of biomass, geothermal, hydroelectric, solar, and wind energies. While some of these technologies have a similar cost to fossil fuels (e.g. wind and geothermal), some of these are more costly to implement.[5] With the prevalence of dissipated thermal energy, temperature gradients are widely observable and can be exploited for alternative energy generation. Temperature differentials found in everyday life are generally too small for thermal energy harvesting techniques (*e.g.* geothermal) to recycle it,[6] so other techniques must be considered.

Thermoelectric energy conversion is a waste heat recycling technology that can capture heat and convert it into useful voltage without the use of moving parts. The thermoelectric performance of a material is evaluated with a dimensionless figure of merit, $ZT = S^2\sigma T \kappa^{-1}$, where S is the Seebeck coefficient ($V K^{-1}$), σ is the electrical conductivity ($S m^{-1}$), T is the absolute temperature (K), and κ is the thermal conductivity ($W m^{-1} K^{-1}$), respectively. For an ideal

thermoelectric material, its Seebeck coefficient and electrical conductivity should be maximized to allow for the highest electrical energy generation that can move freely through the material. On the other hand, the thermal conductivity should be minimized to maintain the temperature gradient formed on opposite ends of the material. Research into improving the thermoelectric performance has been immensely challenging due to the conflicting dependence of carrier concentration in S and σ. Additionally, the value of σ is directly correlated with κ. These interdependencies have limited the thermoelectric performance of bulk thermoelectric materials.[7,8]

One method of weakening the interdependencies between thermoelectric variables is to engineer nanostructured domains in the material to provide more boundaries that preferentially scatter phonons or filter low energy electrons.[9,10] The former strategy serves to lower κ without inhibiting the other variables, while the latter one increases S by a greater magnitude than it decreases σ. Nanostructuring can be used to decrease some dimensions of a material so small that they yield size-dependent properties, which creates a more favorable electronic density of states in addition to reducing κ. This strategy has been demonstrated in many instances for inorganic heterostructures.[9,11–13] Hochbaum et al. demonstrated that an ordered array of silicon nanowires allows for sharp features in the electronic density of states near the Fermi level, which results in more favorable thermoelectric transport.[12]

Currently, binary and ternary inorganic semiconductors result in the best thermoelectric performance (ex. Bi_2Te_3, PbTe, $Cu_{12}Sb_4S_{13}$, BiSbTe, etc.)[14–16] Despite their outstanding properties, these materials have toxicity, scarcity, and mechanical rigidity issues when used as ingots. Recently, flexible thin films of Bi_2Te_3 have been fabricated, but their performance is much lower than a traditional ingot.[17] To combat these drawbacks, organic nanocomposites composed of

polymers and carbonaceous nanofillers (*e.g.* graphene and carbon nanotubes) have been shown to exhibit good n-type and p-type behavior.[3]

While many methods have been used to prepare thermoelectric nanocomposites, such as *in situ* polymerization or polymer emulsions, few provide the precise nanoscale control offered by layer-by-layer (LbL) assembly.[18–21] LbL deposition allows for the nanoscale buildup of the multilayer film through cyclical exposure to positively and negatively charged film components through surface charge reversal. Multilayer films prepared by LbL assembly can make use of a variety of attractive interactions, such as electrostatic,[22] hydrogen bonding,[23] π-π interactions,[24] and covalent bonding.[25] Many variables influence LbL deposition by altering the solution pH, ionic strength, concentration, and temperature during deposition.[26,27] Thermoelectric materials prepared using LbL assembly containing double-walled carbon nanotubes and graphene have been shown to produce power factors much higher than other nanocomposite preparation methods.[28,29] The work described in this dissertation aims to expand the toolbox to improve the thermoelectric performance of polymer nanocomposites, as well as to systematically investigate the performance to understand the influence of the various thermal and doping treatment.

1.2 Objective and Dissertation Outline

The work described in this dissertation serves to introduce new methods of post-deposition thermal treatment and salt doping, to improve the thermoelectric performance of layer-by-layer deposited thin films.

Chapter II introduces the significance of the field of thermoelectrics and details some of the underlying concepts that makes improving thermoelectric performance challenging.

Additionally, a literature review of thermoelectric polymer nanocomposites is provided, as well as the future challenges that must be overcome to make this field impactful on a societal level.

Chapter III describes a post-deposition thermal treatment conducted on a film containing poly(diallyldimethylammonium chloride) (PDDA) , poly(3,4 – ethylenedioxythiophene) :(poly(styrene sulfonate) (PEDOT:PSS), double-walled carbon nanotubes (DWNT), and graphene that were heated to various temperatures to study the influence of film degradation on thermoelectric properties. Degrading the insulating polymer, while maintain the carbon nanotube-graphene network, improves the thermoelectric power factor by one order of magnitude.

Chapter IV demonstrates how thermoelectric properties are improved by removing insulating PSS by adding KBr to the PEDOT:PSS-DWNT deposition solution. KBr addition was evaluated systematically as a function of concentration to understand its effects on TE properties of these films. At the optimum dopant concentration, the six-fold increase in power factor came from the greater proportion of conductive materials (*i.e.* PEDOT and DWNT) that were incorporated into the multilayer film.

Chapter V addresses the influence of cation size on the salt doping strategy addressed in Chapter IV. Simple monovalent salts of LiCl, NaCl, KCl, and CsCl were investigated. The power factor is improved almost five-fold by doping with cesium chloride as compared to the undoped control. Larger cations provide a more efficient doping due to their interactions with DWNT in solution.

Chapter VI summarizes the significance of the work described in this dissertation as well as provides some future directions to improve thermoelectric performance by increasing the options for n-type stabilizers for carbon nanotubes and graphene. Additionally, initial investigations of the additive influence of the strategies presented are evaluated.

CHAPTER II

LITERATURE REVIEW

2.1 Introduction

Thermoelectric energy generation is a wonderful renewable energy source because it can directly convert the excessive amount of waste heat produced by fossil fuels into electrical energy without any moving parts. Thermoelectric materials have been extensively researched since the 1960s,[30,31] and research into improving their performance is ongoing. As shown in **Figure 2.1**, ZT (*i.e.* the thermoelectric efficiency of a material) values improved dramatically after Hicks and Dresselhaus demonstrated that the performance could be greatly improved by introducing nanoscale features that exhibit size-dependent properties.[32–34] While materials were being used for niche applications before this discovery, the large improvements in ZT that followed show promise of a lower cost of implementation.[35,36] Even though the nanostructuring effects have vastly improved the thermoelectric performance of state-of-the-art materials (*i.e.* inorganic semiconductors), they have considerable drawbacks of toxicity, scarcity, and mechanical rigidity. Organic materials comprised of conducting polymers, carbon nanotubes, and/or graphene address these drawbacks, while still exhibiting good thermoelectric performance. This chapter outlines the fundamental concepts behind thermoelectricity, as well as provides in-depth discussion of the different types of inorganic semiconductors, organic semiconductors, and nanocomposite materials.

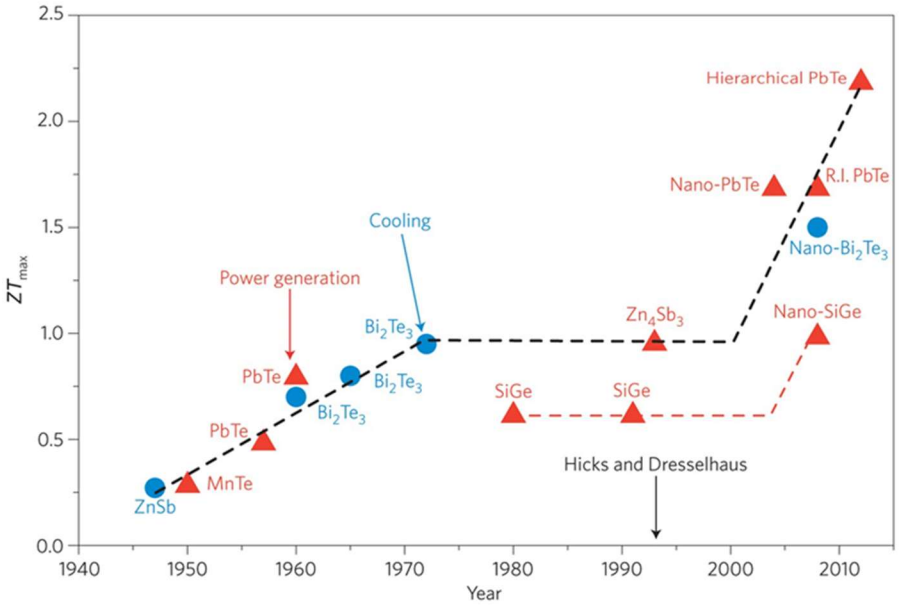

Figure 2.1. Record ZT values reported for thermoelectric materials intended for refrigeration (blue dots) and power generation (red triangles). The large increase in thermoelectric efficiency reported after 2000 followed the seminal work from Hicks and Dresselhaus.[33,34,37] Reprinted with permission from Heremans, J. P.; Dresselhaus, M. S.; Bell, L. E.; Morelli, D. T. When Thermoelectrics Reached the Nanoscale. *Nature Nanotechnology* **2013**, *8* (7), 471 – 473.

2.2 Thermoelectric Transport

The thermoelectric effect is based on the Seebeck, Peltier, and Thomson effects. The Seebeck effect, discovered by Thomas Johann Seebeck in 1821, describes the voltage generation of a material from a temperature gradient.[38] Jean Charles Peltier discovered the Peltier effect 13 years later,[39,40] which is the ability of a material to generate a temperature gradient from a supplied voltage. Lastly, the Thomson effect describes the evolution of heat when an electrical current passes through a material containing a temperature differential at opposite ends.[41] The most important of these discoveries for this dissertation is the Seebeck effect, as power generation is the primary goal of the novel work described in Chapters III, IV, and V. As such, the Seebeck effect will receive the most attention out of the three in the following discussion.

The connection between the Seebeck, Peltier, and Thomson effects is that both electrical charge and thermal energy are simultaneously being transported in the material. In an intrinsic

semiconductor placed across a temperature gradient, the distribution of holes and electrons on the hot and cold sides of the material is uneven due to the variations in the Fermi distribution function for the different temperatures at the hot and cold ends of the material.[35,42] In response to the varying distribution in the Fermi distribution function, these carriers diffuse from the hot side to the cold side to establish thermal equilibrium in the material.[43] As a result, the carriers on the cold side of the film develop an electrochemical potential due to the voltage accumulation from carrier transport. Voltage accumulation is commonly accompanied by a gain in entropy from populating higher energy states on the cold side of the material. The diffusion rate of the hot carriers depends on their activation energy, the probability of the initial and final states involved in transport, and the scattering lifetime of the carriers. A lower activation energy corresponds to a higher diffusion rate and a higher current. This charge carrier diffusion continues until electrostatic equilibrium in the material is achieved, which is when the sum of the free energies of the charge carriers reaches a minimum.[42,44] Additionally, the transport of the charge carriers is accompanied by the transport of thermal carriers, which causes the material to reach a thermal equilibrium as well.

2.2.1 Thermoelectric Transport

The amount of voltage that is generated from the transport of charge carriers per unit temperature is known as the Seebeck coefficient, which is expressed by the following equation:

$$S = \frac{\Delta V}{\Delta T} \qquad (2.1)$$

where S is the Seebeck coefficient, V is the voltage generated, and T is the temperature differential between the hot and cold ends of the material. In other words, the per unit temperature generated in a heat-driven system from the thermal gradient that is balanced in equilibrium with the electric field that creates a flow of opposing charge carriers. As described previously, the Seebeck coefficient also represents the amount of

entropy (i.e. energy) that is transported by the carriers.[45] The sign of the Seebeck coefficient indicates the primary electrical charge carrier within the material. A negative Seebeck coefficient means that electrons are the dominant charge carrier, while a positive Seebeck coefficient indicates that holes (*i.e.* the positively charged carriers that form when an electron is thermally excited from the valence band to the conduction band of a semiconductor) are the dominant charge carrier.[46] The sign convention for the Seebeck coefficient is also expressed with respect to the voltage moving from the hot side to the cold side. Another equation for the Seebeck coefficient that specifically applies to degenerate semiconductors is shown below:

$$S = \frac{8\pi^2 {k_B}^2}{3eh^2} m^* T \left(\frac{\pi}{3n}\right)^{\frac{2}{3}} \qquad (2.2)$$

where e is the elementary charge of an electron, h is Planck's constant, k_b is Boltzmann's constant, m* is the effective mass of the charge carrier, and n is the charge carrier density (*i.e.* the number of charge carriers per unit volume).[3,47] Equation 2.2 shows that the Seebeck coefficient inversely relates to the carrier density. When more charge carriers are transporting the same energy, the average energy transported per carrier is lower.

Another variable that is important in assessing thermoelectric performance is the electrical conductivity, which is the expression of how well free electrons flow through the material. A higher electrical conductivity corresponds to easier electron flow. The electrical conductivity (σ) is calculated from the inverse of the resistivity, which is calculated by measuring the resistance of the length of the material divided by the cross-sectional area. This measurement can be done through two points or four points of contact with the latter being preferred to minimize the contact resistance from the wires. A common way of determining the electrical conductivity, especially of thin films, is by using a four-point probe technique that is represented in Figure 2.2. In this arrangement, a set current flows through two probes, while the other two measure the voltage response of the film. The voltage that is generated per unit current is used to calculate a value known as the sheet resistance (R_s), which is effectively the "thickness-dependent resistance". The sheet resistance of the film is determined by the following equation:

$$R_s = C\left(\frac{V}{I}\right) \quad (2.3)$$

where V is the voltage, I is the current, and C is the correction factor that depends on the spacing between the probes (as well as the dimensions of the sample of interest).[28,48–50] After determining R_s, the electrical conductivity is calculated using:

$$\sigma = \frac{1}{R_s t} \quad (2.4)$$

where t is the thickness of the sample. While the above equations are important for determining the electrical conductivity, there is another important expression, especially for elucidating trends in thermoelectric performance:

$$\sigma = en\mu \quad (2.5)$$

where n is the carrier density, μ is the carrier mobility, and e is the elementary charge of an electron. Equation 2.5 shows that the carrier density and carrier mobility (*i.e.* the amount of friction electrons experience when moving through a material) directly correlate with the electrical conductivity. Intuitively, the increase in electrical carriers whose movement occurs with less friction (*i.e.* greater carrier mobility) will result in a larger electrical conductivity.

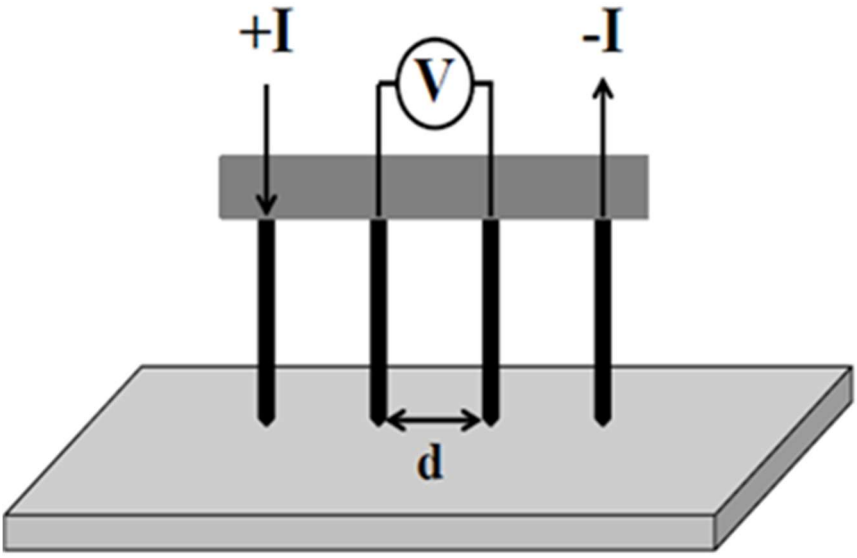

Figure 2.2. Schematic of the four-point probe measurement. The current flows through the two outer probes, while the two inner probes measure the voltage response. All of these probes are separated by a specific spacing (d).[28,51] Adapted with permission from Cho, C.; Stevens, B.; Hsu, J-H.; Bureau, R.; Hagen, D. A.; Regev, O.; Yu, C.; Grunlan, J. C. Completely Organic Multilayer Thin Film With Thermoelectric Power Factor Rivaling Inorganic Tellurides. *Adv. Mater.* **2015**, *27*, 2996 – 3001.

During the transport of charge carriers, thermal carriers move through the material as well, which is referred to as the thermal conductivity. The total thermal conductivity of a material is the sum of the electronic and lattice components (κ_e and κ_L, respectively). The lattice contributions are related to the heat capacity and phonon mean free path of the material, while the electronic contribution is inversely related to the electrical conductivity by a proportionality constant called the Lorenz number.[3,7,8] The thermal conductivity of a material is a measure of how well the thermal gradient is maintained during thermoelectric transport, which then affects how much voltage accumulation occurs at the cold end. Since easier electron flow is advantageous to thermoelectric performance, research efforts prioritize the development of strategies that minimize κ_L.

Overall, the main method of assessing the thermoelectric performance of a material is done so through combining the aforementioned variables into a dimensionless figure of merit:

$$ZT = \frac{S^2 \sigma T}{\kappa} \qquad (2.6)$$

where S is the Seebeck coefficient (V K^{-1}), σ is the electrical conductivity (S m^{-1}), κ is the thermal conductivity, and T is the absolute temperature (K) of the material. An ideal thermoelectric material would generate the maximum amount of voltage per unit temperature (i.e. maximize S), with the charge carriers being highly delocalized (i.e. maximize σ), while maintaining the temperature gradient established in the material (i.e. minimize κ). In this way, the ideal thermoelectric material is approached by a "phonon glass electron crystal" strategy.[52,53] However, S, σ, κ are all interrelated in a negative way. Equations **2.2** and **2.5** express how S and σ are anticorrelated. The carrier density is inversely correlated for S, while it is directly correlated for σ. This physical limitation has been a challenge for researchers. Additionally, improvements in the electrical conductivity are compromised by the larger thermal conductivity according to the Wiedemann-Franz law. In light of these interdependencies, optimal thermoelectric performance was previously achieved by optimizing the carrier density of the material, as shown in **Figure 2.3**. Ultimately, finding the optimum carrier density has limited the development of practical thermoelectric materials.

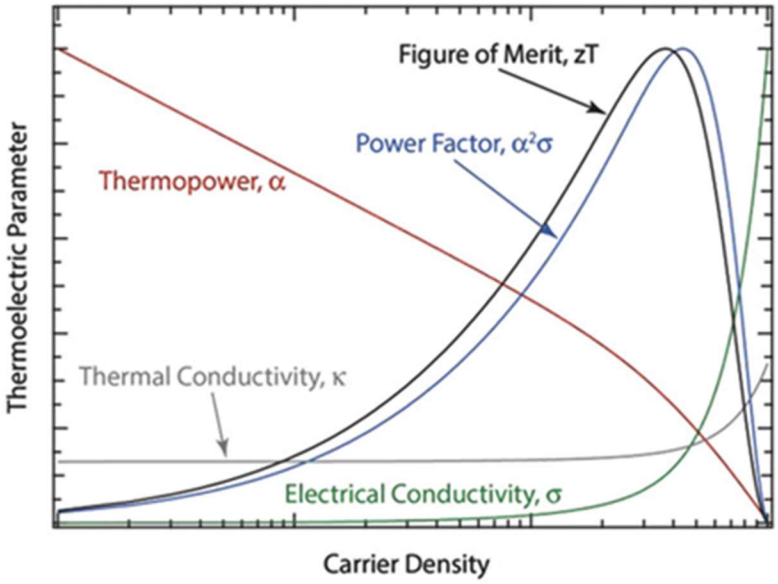

Figure 2.3. How the variables that determine thermoelectric performance affect each other as a function of the carrier density.[3] Adapted with permission from Blackburn, J. L.; Ferguson, A. J.; Cho, C.; Grunlan, J. C. Carbon-Nanotube-Based Thermoelectric Materials and Devices. *Adv. Mater.* **2018**, *30* (11), 1704386.

2.2.2 Overcoming the Limitations of Traditional Thermoelectric Materials

As shown in **Figure 2.1**, improvements in ZT were realized after two 1993 publications from Hicks and Dresselhaus presented how thermoelectric transport is altered when nanostructures are introduced in a material.[33,34] Reducing the dimensions of a material to the nanoscale were reported to introduce size-dependent or quantum confinement effects that provide an effective way of tuning the electronic density of states (DOS).[54,55] The DOS are important in thermoelectric transport because the placement and occupancy of these available states near the Fermi level directly affect the magnitude of the Seebeck coefficient. This strategy has been demonstrated in many state-of-the-art materials.[9,11,12,16] For example, constructing an ordered array of metallic nanowires allows for a greater asymmetry in the DOS near the Fermi level that improves thermoelectric transport.[56,57] Creating nanoscale interfaces also shows an additional benefit by

creating more scattering events for heat-carrying phonons. These boundaries reduce the mean free path of the phonons, thereby reducing κ, without a significant decrease in the Seebeck coefficient or electrical conductivity. Poudel et al. demonstrated that simply ball milling BiSbTe, followed by densifying it into a pellet by spark plasma sintering, improved the ZT by approximately 40% due to the reduction of the phonon mean free path through grain boundary engineering (**Figure 2.4a-b**).[9] Engineering interfaces within a material can also selectively filter low energy electrons depending on the energy level at that interface, as shown in **Figure 2.4c-e**. These boundaries serve to lower the number of carriers that participate in electron conduction, which results in a larger S due to the increase in transported energy per charge carrier.[10] However, due to the decreased number of charge carriers, the electrical conductivity typically decreases slightly. Despite the lowered electrical conductivity, the power factor (and therefore ZT) of the material is improved.

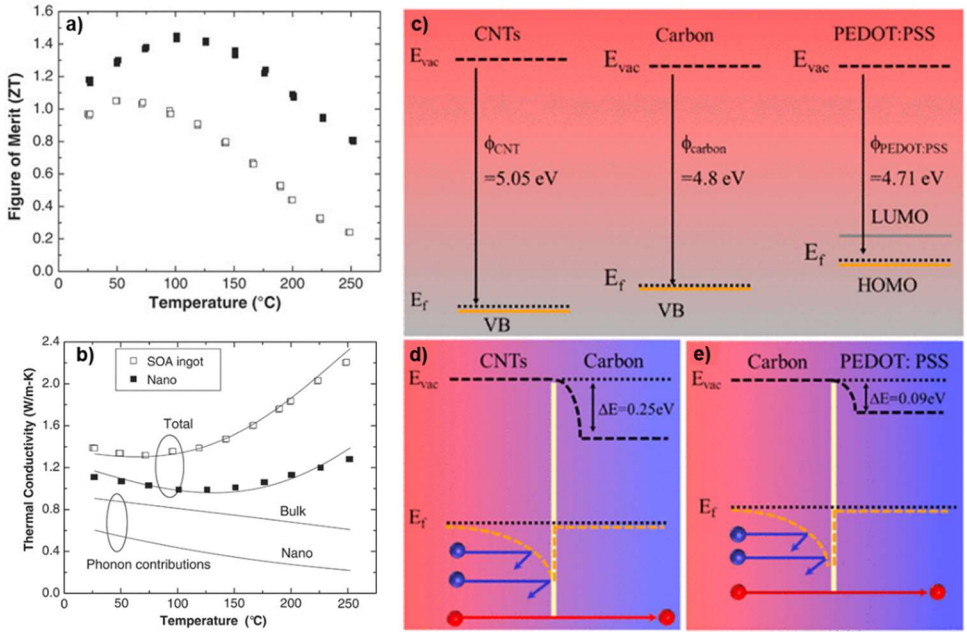

Figure 2.4. (a) ZT and **(b)** thermal conductivity as a function of temperature for BiSbTe samples with and without nanoscale inclusions.[9] The increase in ZT from nanoscale features was shown to be a function of phonon scattering. **(c)** Work functions for carbon nanotubes, adventitious carbon, and PEDOT:PSS. **(d)** CNT/carbon contact and **(e)** carbon/PEDOT:PSS contact that demonstrate low-energy electron filtering.[10] Adapted with permission from Poudel, B.; Hao, Q.; Ma, Y.; Lan, Y.; Minnich, A.; Yu, B.; Yan, X.; Wang, D.; Muto, A.; Vashaee, D.; Chen, X.; Liu, J.; Dresselhaus, M. S.; Chen, G.; Ren, Z. High-Thermoelectric Performance of Nanostructured Bismuth Antimony Telluride Bulk Alloys *Science*, **2008**, *320* (5876), 634 – 638 and Li, D.; Luo, C.; Chen, Y.; Feng, D.; Gon, Y.; Pan, C.; He, J. High Performance Polymer Thermoelectric Composite Achieved by Carbon-Coated Carbon Nanotubes Network *ACS Appl. Energy Mater.* **2019**, *2* (4), 2427 – 2434.

2.3 Inorganic Thermoelectric Materials

Throughout the early stages of thermoelectric research, the effects of thermoelectric materials were studied in bulk solids. At the time, an ideal candidate for thermoelectric transport was a highly conducting semiconductor with a relatively narrow band gap and a high carrier mobility, with a ZT close to 1.[42,43] Tellurium-based binary semiconductors of MnTe and PbTe were some of the first thermoelectric materials developed for power generation in the 1950s.[31,58,59] One of the most successful thermoelectric inorganic semiconductors developed for refrigeration applications was Bi_2Te_3 due to its layered structure from the covalent bonds from between the in-

plane Bi and Te, as well as dispersion forces between these layers and low band gap of 0.16 eV.[14,40,42] High carrier mobilities and anisotropic transport are a result of its layered structure, but its optimum thermoelectric performance occurs well above room temperature.[42] To address this issue, alloys prepared with Se and Sb dopants for the Te and Bi crystalline sites, respectively, were incorporated into the lattice.[9,60] The improved ZT values came from the diminished thermal conductivity values arising from the scattering of acoustic phonons. Since the introduction of the nanostructuring strategy, the ZT values of these components, nanostructured materials of PbTe and Bi_2Te_3 and their alloys have seen at least a 50 % improvement in ZT.[9,11]

Another important class of inorganic thermoelectric materials is Half-Heuslers. These materials are composed of three different elements in a 1:1:1 stoichiometry that have three overlapping face-centered cubic lattices that similar to zinc blende structures.[16,61,62] In particular, preparing nanocomposites of these materials has been shown to reduce the thermal conductivity by incorporating grain boundaries separated by a nanoscale distance.[63] A report by Yan et al. reported a Half-Heusler nanocomposite, that was prepared by hot pressing a ball-milled $Zr_{0.5}Hf_{0.5}CoSb_{0.8}Sn_{0.2}$ compound, increased its ZT from 0.5 to 0.8 at 700 °C due to the reduced thermal conductivity.[64] Additionally, materials where dopant atoms are introduced into the lattice is another way to modify the carrier concentration and produce defects that ultimately serve to scatter phonons. For example, Zhu et al. found that introducing more Ti into a TaFeSb-based Half Heusler leads to a larger electrical conductivity and a smaller thermal conductivity due to the lower phonon velocity.[65]

Other promising inorganic materials tend to be those with a cubic structure due to their large band degeneracy.[61,65] Prominent examples in the literature are skutterudites and tetrahedrites. The unit cell of skutterudites have a large vacancy in the body center that can host a number of

atoms to drastically alter the thermoelectric properties.[52,66] In particular, skutterudites with body centers that are partially filled with electron donors can exhibit lower thermal conductivities and larger power factors as compared to completely filled skutterudites. Indium-filled $CoSb_3$ materials are a good example because the electron donating character of In results in a dramatic increase in the Seebeck coefficient, while distortions from accommodating the In in the lattice increase phonon scattering.[66] A greater proportion of occupying these vacancies results in continual improvements in power factor until a saturation point where adding more of the host atom does not change the lattice parameters. Tetrahedrites ($Cu_{12}Sb_4S_{13}$) are a naturally occurring mineral that is commonly found mixed with tennantite ($Cu_{12}As_4S_{13}$).[15,67] In addition to its cubic structure, tetrahedrite is composed of earth-abundant elements and has a relatively low cost. Its highly symmetric unit cell of three separate atoms makes it amenable to a wide array of dopants on either the Cu, Sb, or even S sites. Doping tetrahedrite with atoms such as Zn, Ni, or Mn on the Cu sites result in ZT values near 1.0 by increasing the Seebeck coefficient and decreasing the thermal conductivity.[67,68] While synthetic tetrahedrites can be prepared with viable thermoelectric efficiency, it has been suggested that using it directly from its mineral form may be a suitable option too.[69] **Figure 2.5** shows the common crystal structures of well-known Half-Heuslers, skutterudites, and tetrahedrite structures.

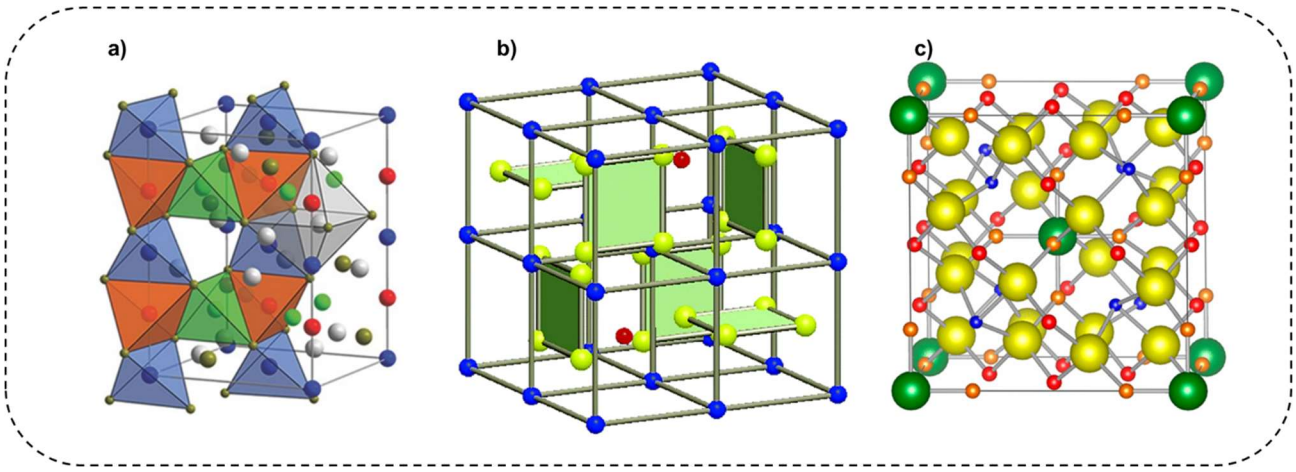

Figure 2.5. Unit cells of (a) Half-Heusler,[70] (b) skutterudite,[66] and (c) tetrahedrite compounds.[15] Adapted with permission from Li, D.; Zhao, H.; Li, S.; Wei, B.; Shuai, J.; Shi, C. Xi, X.; Sun, P.; Meng, S.; Gu, L.; Ren, Z.; Chen, X. Atomic Disorders Induced by Silver and Magnesium Ion Migrations Favor High Thermoelectric Performance in α-MgAgSb-Based Materials. *Adv. Funct. Mater.* **2015**, *25* (41), 6478 – 6488, He, T.; Chen, J.; Rosenfeld, H. D.; Subramanian, M. A. Thermoelectric Properties of Indium-Filled Skutterudites. *Chem. Mater.* **2006**, *18* (3), 759–762, and Weller, D. P.; Stevens, D. L.; Kunkel, G. E.; Ochs, A. M.; Holder, C. F.; Morelli, D. T.; Anderson, M. E. Thermoelectric Performance of Tetrahedrite Synthesized by a Modified Polyol Process. *Chem. Mater.* **2017**, *29* (4), 1656–1664.

Although inorganic thermoelectric materials have exhibited ZT values well above 1, these materials suffer from issues pertaining to their scarcity,[71] toxicity,[72] mechanical rigidity, and energy intensive processing methods.[9] These issues have impeded their widespread use. Furthermore, their maximum efficiencies typically lie at temperatures above 350 K, which further limits their practical use. In order to create thermoelectric materials that overcome these drawbacks, implementing other materials must be explored.

2.4 Organic Thermoelectric Materials

Thermoelectric materials prepared from polymers and their composites are an interesting new avenue of exploration due to their relatively inexpensive solution-processing, mechanical flexibility, elemental abundance, and tailorable electronic energy levels. One very noteworthy

advantage of polymer and polymer nanocomposite thermoelectric materials is that they typically have very low thermal conductivities (~0.5 W m^{-1} K^{-1}).[7] Maximizing the thermoelectric performance of these materials is primarily focused on improving the power factor ($S^2\sigma$) because they tend to have much lower carrier concentrations than their inorganic counterparts.

2.4.1 Polymeric Thermoelectric Materials

Improvements in the thermoelectric performance of polymer thermoelectric materials has been focused on increasing the electrical conductivity to raise their power factors into a competitive range. Many of these polymers are comprised of a rigid and conjugated backbone that feature side groups that vary the packing of polymer chains, which strongly influence the electrical conductivity of the material.[73] Improving the electrical conductivity of polymers is conceptualized similarly to inorganic thermoelectrics, as it primarily lies in modulating the energy gap between the highest occupied molecular orbital (HOMO) and lowest unoccupied molecular orbital (LUMO). The HOMO and LUMO energy levels can be tailored in multiple ways. One strategy involves introducing side chains with various electron donating or withdrawing groups. Electron donating groups increase the energy of the HOMO and decrease the energy of the LUMO, while electron withdrawing groups do the opposite. This strategy has been demonstrated with derivatives of common polymers used for thermoelectric applications.[74,75] Furthermore, this strategy has even been extended to complex copolymers with monomers containing different energy levels to result in different band gaps that stem from the difference in the energy levels between the respective molecules. Molecular dopants can be added as another strategy to modify the HOMO and LUMO levels of a polymer. P-type molecular dopants require electron withdrawing character, while n-type molecular dopants require electron donating character. P-type dopants require the LUMO

level that is at a lower energy than the HOMO of the material, whereas n-type dopants need a HOMO that is at a higher energy level than the LUMO of the material. N-type doping is a particular challenge for organic materials due to the oxidative susceptibility of a material that has a high energy HOMO.[7,76]

An additional consideration of organic semiconductors is the volume of the dopant. Since doping tends to work by donating or withdrawing electron density to or from the polymer backbone, the volume the dopant occupies can affect the intermolecular packing of the polymer.[77,78] The energy structure of polymeric semiconductors that results from doping tends to have a higher amount of defects and impurities, which results in band broadening that influences the charge transport of these materials.[7,79] Typical transport in organic semiconductors is often described by either the hopping of carriers between electronic states or a mobility edge-based model.[47,80,81] The former suggests that there is an activation energy required for a charge carrier to hop to the next available electronic state, while the latter model is related to the degree of disorder in the material, as described by Anderson localization.[47] Similarly to inorganic semiconductors, a large amount of doping can cause the Fermi level to shift into either band, which can cause a drastic decrease in the Seebeck coefficient.[82]

The chemical structures of commonly used polymers for thermoelectric applications are shown in **Figure 2.6**. A majority of these conducting polymers have low Seebeck coefficients and charge carrier density, with the exception of iodide-doped polyacetylene,[83,84] but air stability issues completely limit the practicality of its application. The next most promising conductive polymer is poly (3,4, -ethylenedioxythiophene): poly (styrene sulfonate) (PEDOT:PSS), which has been widely demonstrated to yield good thermoelectric performance. PEDOT:PSS is a water-dispersible, polymer complex that exhibits p-type transport and is prepared by polymerizing EDOT

in the presence of PSS.[85,86] The ionic stabilization PSS imparts to PEDOT in water allows it to be easily processed for practical thermoelectric applications.

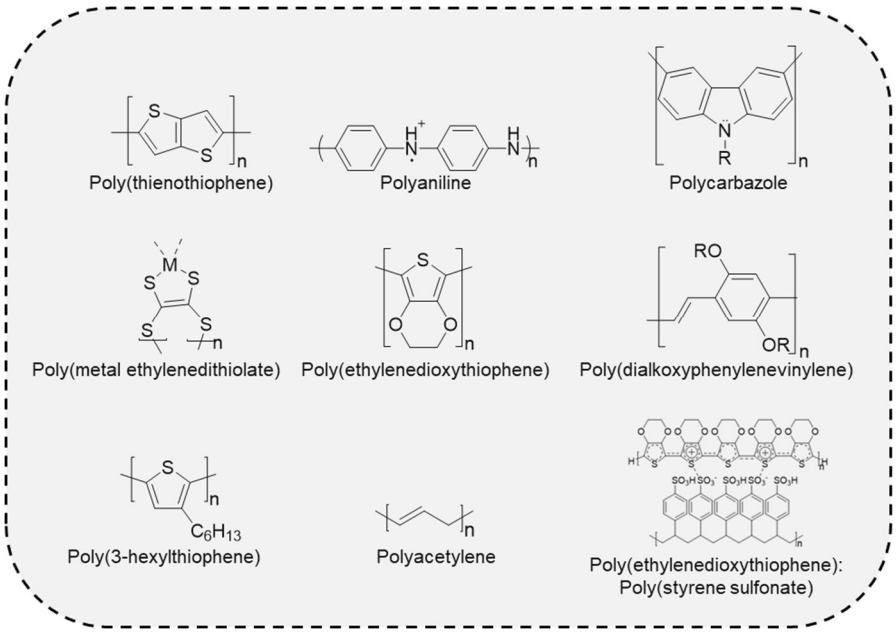

Figure 2.6. Chemical structures of common conducting polymers.[79] Adapted with permission from Poehler, T. O.; Katz, H. E. Prospects for Polymer-Based Thermoelectrics: State of the Art and Theoretical Analysis. *Energy Environ. Sci.* **2012**, *5* (8), 8110.

The electrostatic interactions from PSS that stabilize PEDOT in water are also important in improving thermoelectric properties. Deprotonated SO_3^- groups on PSS add additional positive charge carriers in the thiophene backbone of PEDOT, which serves to tune the electrical conductivity by changing the charge carrier density.[82,87] At moderate levels of PSS oxidation, these positive charge carriers are referred to as polarons, which are delocalized over a small number of repeat units. Reaching a large extent of oxidation leads to the formation of bipolarons, where the number of localized polarons form pairs and become delocalized over the entire backbone of the polymer, resulting in a larger electrical conductivity.[87,88] Using acid doping to fully oxidize PSS,

followed by subsequent base treatment to "dedope" PEDOT:PSS, has resulted in power factors in the 10^2 μW m^{-1} K^{-2} range, which is very respectable for an organic material.[82] In addition, electrochemical studies of PEDOT prepared in the presence of a PEG copolymer resulted in a ZT of 1.02 at an optimized carrier density.[89]

Another way of improving the performance of PEDOT:PSS-based thermoelectric materials is to modify the dopant volume by either polymerizing PEDOT in the presence of a different stabilizing ion, or by removing PSS with a solvent treatment. The former strategy was demonstrated by Bubnova et al., where they synthesized PEDOT in the presence of tosylate instead of PSS.[86] This study demonstrated that using tosylate instead of PSS as the ionic stabilizer/dopant for PEDOT gave the sample semimetallic properties as opposed to semiconducting properties, which resulted in a higher Seebeck coefficient and electrical conductivity. Although semimetals typically have no real band gap and an extremely small electronic DOS near the Fermi level, the increase in carrier mobility was enough to result in a larger Seebeck coefficient.

The usage of an external polar solvent serves to compete with the ionic stabilization of PEDOT from PSS to increase the thermoelectric performance of PEDOT:PSS. Previous reports suggest a hydrogen bonding mechanism for the solvent removal, but this mechanism has not been fully substantiated.[90] Highly polar solvents (*e.g.* ethylene glycol and DMSO) have resulted in improved thermoelectric performance by removing PSS chains, where a majority of its sulfonate groups are protonated as they do not contribute any charge carriers.[90,91] Removing more of the insulating PSS serves to promote π-π stacking of PEDOT chains, and this morphological change is enough to achieve an electrical conductivity in excess of 2,000 S cm^{-1}.[73] The thermoelectric properties of PEDOT:PSS-based thin films are summarized in **Table 2.1**.

Table 2.1. Summary of the thermoelectric properties of PEDOT:PSS-based films.

Sample	S ($\mu V K^{-1}$)	σ ($S cm^{-1}$)	κ ($W m^{-1} K^{-1}$)	Power Factor ($\mu W m^{-1} K^{-2}$)/ZT	Reference
Pristine PEDOT:PSS	15-18	<1	N/A	N/A	[92]
PEDOT Nanowires	7-40	30-120	N/A	N/A/ N/A	[93]
DMSO	960	73	0.22	469/ 0.42	[91]
DMSO/Ethylene Glycol	298	14.2	0.4	N/A/ 0.01	[94]
Ethylene Glycol	870	62	0.23	~340/0.28	[91]
$ZnCl_2$ in DMF	26.1	1400	NA	98.2	[92]
$InCl_3$	N/A	95.5	N/A	N/A	[95]
EMIM:TCB	N/A	2,103	N/A	N/A	[73]
TSA, then Hydrazine	49.3	1310	N/A	318.4/ N/A	[87]
HCl, then NaOH	39.2	2170	N/A	334/ N/A	[82]
PEDOT:Tos	55	1,500	0.37	454 / 0.25	[86]
PP-PEDOT	80-190	1,354	0.37	1,270/ 1.02	[89]

2.4.2 Polymer Nanocomposite Materials

While PEDOT:PSS-based thermoelectric materials have demonstrated great promise, the usage of polymer nanocomposite materials is exceptionally interesting. As stated previously,

nanocomposites provide more scattering events for phonons associated with electronic carriers and the matrix that results in a lower thermal conductivity. In addition, particular nanomaterials can often contribute a higher electrical conductivity than the polymer alone. Inorganic-organic hybrid films containing polymers prepared by physical mixing with Bi_2Te_3 have shown a fivefold increase in the power factor relative to the sample without the inorganic filler.[96] See et al. added Te nanorods to PEDOT:PSS that dramatically improved the power factor of the composite film from 0.05 to 70.9 $\mu W\ m^{-1}\ K^{-2}$.[97] Both of these studies are demonstrations of a reasonable strategy to improve the Seebeck coefficient up to one order of magnitude as compared to the polymer alone. Most composite materials obey Bergmann's hypothesis, which states that the ZT of a composite cannot be greater than that of the filler.[98] It has been suggested that this hypothesis was with conventional composite preparation methods that do not account for the quantum confinement and nanocomposite strategies presented by Hicks and Dresselhaus.[33,98] More recent reports have suggested that interfacial effects make the carrier transport in thermoelectric nanocomposites more efficient.[29,88,99] These interfacial effects also increase the number of charge carriers that increase the electrical conductivity. Previous work suggests that understanding these nanoscale effects is crucial to maximizing thermoelectric performance of polymer nanocomposites.

2.5 Carbon Nanofiller-Based Thermoelectric Composites

High performing thermoelectric polymer nanocomposites containing carbonaceous nanofillers (*e.g.* carbon nanotubes and graphene) have been demonstrated recently.[3] When isolated, these nanofillers are estimated to have electrical and thermal conductivities in the 10^4 S cm^{-1} and 10^3 W $m^{-1}\ K^{-1}$ ranges, respectively.[100] While the individual properties of these materials

are promising, their practical potential lies in being able to process them to yield the best performing nanocomposite.

2.5.1 Carbonaceous Nanofillers

In 1992, simulations of a 1-dimensional rope of sp^2 hybridized carbon atoms were suggested to give remarkable size-dependent electronic structures.[32,101] These simulations were demonstrated experimentally the following year when two independent reports presented the preparation of these structures that were coined single-walled carbon nanotubes.[102,103] In response, researchers investigated the promising nanotube properties, including diameter-dependent optical and electrical band gaps and high carrier mobility.[55,104] However, it was not until 2002 when O'Connell et al. developed a way to disperse SWNTs in water using micelle-forming surfactants.[105] Since that time, researchers have been developing new ways to disperse and prepare SWNT-containing materials for many applications including sensing,[106] biological imaging,[107] photovoltaic,[108] and thermoelectric applications.[29,109]

Graphene is an atom thick sp^2 hybridized two-dimensional sheet of carbon atoms. It has become one of the most studied materials due to its promising electrical and thermal properties that arise from its unique structure.[110] While its structure yields very high electron mobilities that are good for electrical conductivity, the band structure around the Fermi level gives graphene a low Seebeck coefficient. Band structure calculations reveal that graphene is a semiconductor with a bandgap of 0 eV due to an equal amount of electron and hole carriers. The ambipolar nature of pristine graphene allows for facile tuning of the band structure.[19,110] Optimizing its band structure in conjunction with altering the processing and doping strategies provides maximum thermoelectric performance. **Figure 2.7**. shows the structure of carbon nanotubes and graphene.

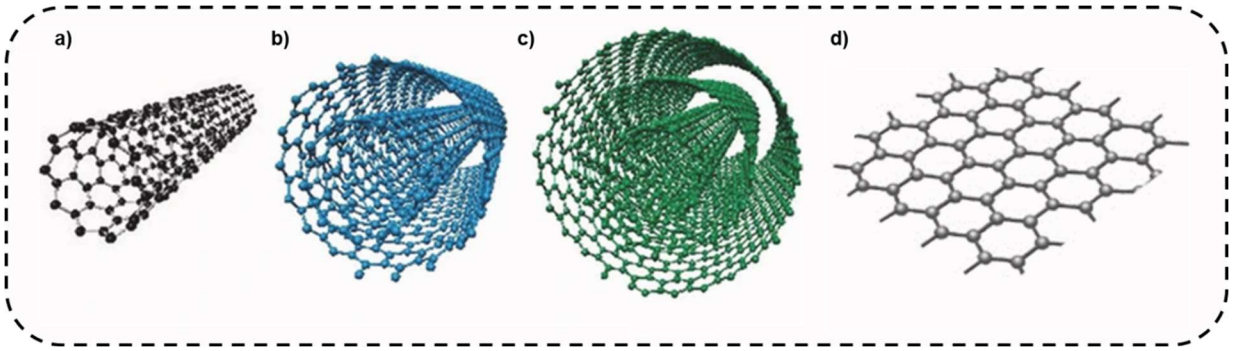

Figure 2.7. Structures of **(a)** single-walled carbon nanotubes, **(b)** double-walled carbon nanotubes, **(c)** multi-walled carbon nanotubes, and **(d)** graphene.[19,111] Adapted with permission from Zhang, K.; Zhang, Y.; Wang, S. Enhancing Thermoelectric Properties of Organic Composites through Hierarchical Nanostructures. *Sci. Rep.* **2013**, *3* (1), 3448 and Labulo, A. H.; Martincigh, B. S.; Omondi, B.; Nyamori, V. O. Advances in Carbon Nanotubes as Efficacious Supports for Palladium-Catalysed Carbon–Carbon Cross-Coupling Reactions. *J. Mater. Sci.* **2017**, *52* (16), 9225–9248.

2.5.2 Carbon Nanotube- and Graphene-Based Composites

Thermoelectric properties of polymer nanocomposite films prepared with carbon nanotubes and/or graphene are summarized in **Table 2.2**. Carbon nanotube-based composites commonly use polymers as the matrix to provide favorable optical and mechanical properties. For example, PDDA has been used to prepare a transparent SWNT-based nanocomposite with high electrical conductivity.[49,50] Previously, carbon nanotubes incorporated as the filler in thermoelectric segregated network composites (SNC) generated excellent thermoelectric properties.[112–114] These composites are based on percolation theory that describes the formation of a network in a polymer nanocomposite.[115,116] The electrical conductivity increases dramatically when a critical filler concentration is reached, and then it stays constant as more filler is added. This critical filler concentration indicates that percolation has been attained (*i.e.* that a continuous network throughout the material has been reached). Initial composites from percolation theory

featured dispersed fillers that were homogeneously exfoliated in the matrix, whereas a SNC contains particles that reduce the volume fraction the fillers can occupy.[112] As a result, SNC's have a much lower percolation threshold than random dispersed networks.[117] The thermoelectric performance of these composites were improved by gradually swapping insulating polymer matrices for semiconducting small molecules (*e.g. meso*-tetra(4-carboxyphenyl) porphyrin) and intrinsically conducting stabilizers (*e.g.* PEDOT:PSS). The power factor improved from 42.8 to 500 $\mu W\ m^{-1}\ K^{-2}$ in composites that used DWNT as the conductive filler.[51] SWNT samples prepared from direct synthesis methods provide larger Seebeck coefficients and electrical conductivities by maintaining the SWNT length that is lost during processing in aqueous conditions.[3] Furthermore, composites prepared with DWNT have been shown to have greater electrical conductivity due to fewer defects than SWNT, as shown with Raman spectroscopy.[29,118]

Graphene-based composites have been prepared by powder mixing, solution dispersion, and *in-situ* polymerization. Powder mixing tends to yield very poor thermoelectric properties, as mechanical mixing does not effectively disperse the nanoplatelets.[119] Solution dispersion with a surfactant may help disperse or align conjugated polymers such as polyaniline to yield a high electrical conductivity. As compared to powder mixing, the electrical conductivity for a PANi/graphene composite exhibits a seven-fold improvement.[120] However, the solution dispersion strategy results in a lower Seebeck coefficient than the powder mixing strategy, which is likely due to a larger carrier density as the mechanism for improvement in the electrical conductivity. In general, the relatively low Seebeck coefficients exhibited by both strategies indicate a minimal alteration in the electronic structure of graphene that stems from a low doping efficiency. Using *in*-situ polymerization can yield electrical conductivities in the 10^3 S cm^{-1} range for poly(aniline) (PANi)/graphene and PEDOT/rGO composites.[121,122] Furthermore, using different morphologies

of graphene can yield an electrical conductivity of 3,677 S cm^{-1}.[123] Combining carbon nanotube and graphene fillers in the same composite result in a conductive network that can better span three dimensions. The combination of these fillers leads to a reduction in contact resistance while creating more interfaces which improve both the electrical conductivity and Seebeck coefficient, respectively.[29,124,125]

Table 2.2. Thermoelectric properties of carbon nanotube- and graphene-based polymer nanocomposites.

Materials	Preparation Method	S ($\mu V K^{-1}$)	σ ($S cm^{-1}$)	Power Factor ($\mu W m^{-1} K^{-2}$)	Reference
PEI/SWNT/$NaBH_4$	Simple Mixing	-80	20	12.8	[126]
P3HT/SWNT	Simple Mixing	32	275	95	[18]
PEI/SWNT/PEI	Polymer Emulsion	15	-100	15	[127]
PEDOT:PSS/ SWNT/PVAc	Polymer Emulsion	41	1350	160	[112]
PEDOT:PSS/ DWNT/TCPP	Polymer Emulsion	70	960	500	[51]
PANi/SWNT	*In Situ* Polymerization	40	125	20	[121]
PEDOT:PSS/ graphene/MWNT	*In Situ* Polymerization	42	780	151	[128]
P3HT/SWNT	Spin Coating	2760	31	267	[128]
PANi/SWNT	Electrochemical Deposition	31.53	45.4	6.5	[129]
PANi/PSS-graphene/PANi/ SDBS-DWNT	Layer-by-Layer Assembly	130	1080	1825	[28]
PANI/PEDOT:PSS -graphene/PANi/ PEDOT:PSS - DWNT	Layer-by-Layer Assembly	120	1885	2710	[29]
BPEI – DWNT/ PVP- graphene	Layer-by-Layer Assembly	-80	300	190	[24]

2.5.3 Layer-by-Layer Assembly

Although the methods described in Section 2.5.2 has been used to achieve power factors in the 10^2 μW m^{-1} K^{-2} range, even better performance can be realized by using layer-by-layer (LbL) assembly (**Figure 2.8a**). LbL deposition is a thin film assembly technique that was founded by Iler in 1966.[130] He deposited oppositely charged colloidal particles on a substrate, but the technique was largely dormant until reinvigorated by Decher et al. using polymers with charged repeat units (*i.e.* polyelectrolytes).[131] LbL assembly allows for the nanoscale buildup of thin multilayer films through cyclical exposure to solutions of the cationic and anionic components, relying on overcompensation of the surface charge from the prior deposition step. Recently, studies on the buildup of polyelectrolyte multilayers reveal that the association of oppositely charged polyelectrolytes is favored due to the entropic gain of counterion expulsion as opposed to electrostatic forces (**Figure 2.8b**).[132] These films can be prepared using a myriad of other attractive forces, including hydrogen bonding, π-π stacking, and covalent bonding.[23–25] In addition, these coatings have been prepared from a wide variety of ingredients, such as polyelectrolytes, nanoparticles, conjugated polymers, clays, and proteins on a wide variety of substrates.[28,133,134] Solution pH, ionic strength, concentration, and deposition temperature, are used to alter growth and properties of these LbL-deposited films.[22,27]

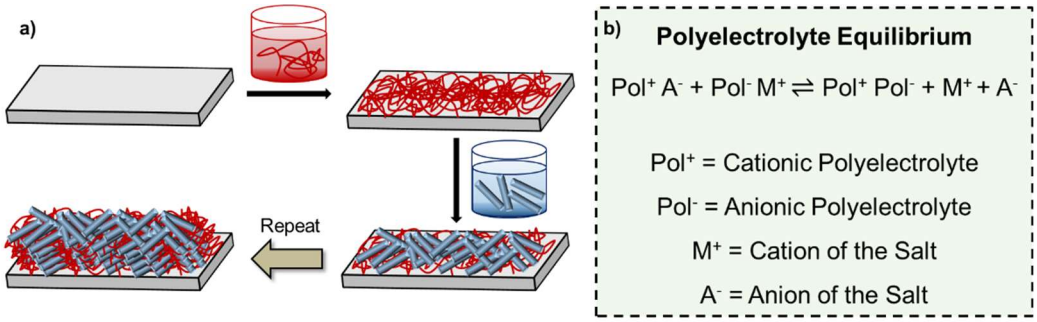

Figure 2.8. (a) General schematic of layer-by-layer assembly. This preparation of a bilayer system (i.e. two deposition solutions) can be extended to quadlayers (i.e. four deposition solutions). **(b)** A general description of the equilibrium around polyelectrolyte complexation.

A key component that is commonly affected with these deposition variables is the charge density of the film constituent. In the case of polyelectrolytes, a polymer with a lower charge density results in a chain conformation with a more random coil, while a higher charge density will cause it to be more elongated due to electrostatic repulsion between the charged repeat units. Polymers that are deposited as random coils lead to a thicker and more porous LbL film, while an elongated rigid rod-like conformation leads to a thinner and denser film.[135] The many variables, chemistries, and attractive forces available for depositing films using LbL assembly makes it an attractive method for preparing thermoelectric nanocomposites.

The application of layer-by-layer assembly to carbon nanotube-based thermoelectrics was first demonstrated by Rivadulla et al., where SWNT were dispersed in poly (allylamine hydrochloride) (PAH), resulting in PAH chains physisorbed to the outside wall of the SWNTs. Next, the PAH-wrapped SWNT was coated with PSS, followed by LbL assembly until the desired number of PAH/PSS layers were deposited. This study demonstrated that altering the spacing between carbon nanotubes using a wrapped polymer film affects the distance between the nanotubes, film density, and film thickness, which alter the Seebeck coefficient and electrical

conductivity.[136,137] Add sentence about power factor, although this study was to gain fundamental understanding)

Cho et al. deposited quadlayers of polyaniline (PANi), graphene stabilized by PSS, PANi, and DWNT stabilized by sodiumdodecylbenzenesulfonate. A 470 nm thick 40 quadlayer (QL) film exhibits an electrical conductivity of 1,080 S cm^{-1} and a Seebeck coefficient of 130 μV K^{-1}, resulting in a power factor of 1,825 μW m^{-1} K^{-2}. This large power factor is attributed to two primary factors: (1) the interfacial interactions between PANi and DWNT from π-π stacking that was demonstrated by a red shift of the benzenoid transition of PANi in its electronic spectrum (**Figure 2.9a**) and (2) The reduced contact resistance from the graphene-carbon nanotube contacts that form during deposition that was revealed by TEM imaging (**Figure 2.9b,c**).[28]

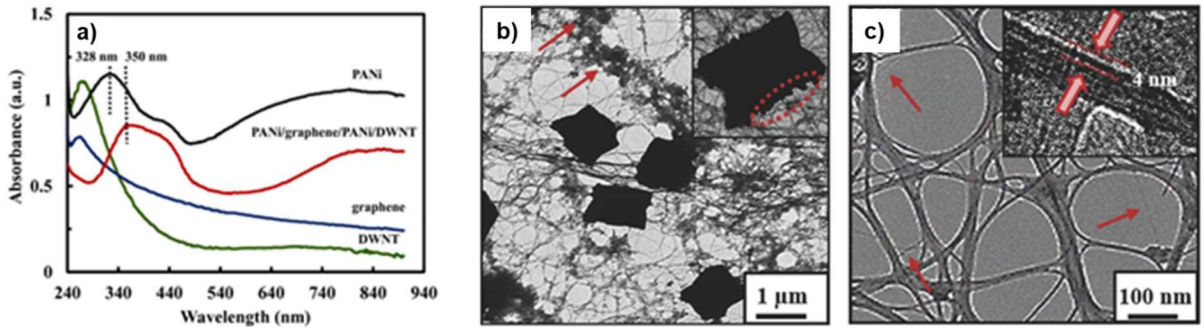

Figure 2.9. (a) Electronic spectra of PANi, graphene, DWNT, and the quadlayer film. **(b,c)** TEM images of a 4 QL PANi/PEDOT:PSS – graphene/ PANi/ PEDOT:PSS – DWNT film.[28,29] Adapted with permission from Cho, C.; Stevens, B.; Hsu, J. H.; Bureau, R.; Hagen, D. A.; Regev, O.; Yu, C.; Grunlan, J. C. Completely Organic Multilayer Thin Film with Thermoelectric Power Factor Rivaling Inorganic Tellurides. *Adv. Mater.* **2015**, *27* (19), 2996–3001 and Cho, C.; Wallace, K. L.; Tzeng, P.; Hsu, J. H.; Yu, C.; Grunlan, J. C. Outstanding Low Temperature Thermoelectric Power Factor from Completely Organic Thin Films Enabled by Multidimensional Conjugated Nanomaterials. *Adv. Energy Mater.* **2016**, *6* (7), 1502168.

It should be noted that the bilayer films comprised of only one of the carbon fillers (*i.e.* PANi/PSS-graphene and PANi/SDBS-DWNT) only gave power factors of 0.08 and 765 μW m^{-1} K^{-2}, respectively. The beneficial morphology from incorporating both fillers results in a larger carrier mobility and a constant carrier concentration observed with Hall Effect measurements that suggest a low energy charge carrier filtering mechanism.[8,28] Improvements on this study were realized by using PEDOT:PSS as a more conductive surfactant to stabilize DWNT and graphene in solution. This substitution produces a power factor of 2710 μW m^{-1} K^{-2} with 80 QL of PANi/PEDOT:PSS-graphene/PANi/PEDOT:PSS-DWNT. Using a planar and conjugated polymer like PEDOT during deposition results in a greater electrical conductivity without a substantial decrease in the Seebeck coefficient.[29]

LbL assembly has been used to prepare n-type thermoelectric films by using surfactants for DWNT and graphene that have been previously demonstrated as n-type dopants. These surfactants have heteroatoms (typically nitrogen) that have lone pairs of electrons that donate electron density to the carbon nanofillers. Cho et al. used branched polyethyleneimine (BPEI) as a surfactant for DWNT and polyvinylpyrrolidone (PVP) as a surfactant for graphene.[24] While most films prepared using LbL assembly occur from ingredients with charged units, the buildup of this film is driven by π-π interactions and van der Waals forces between the film ingredients. An 80 BL film exhibits a Seebeck coefficient of -80 μV K^{-1} and an electrical conductivity of 300 S cm^{-1}, resulting in a power factor of 190 μW m^{-1} K^{-2}. Additionally, this film showed good air stability with the Seebeck coefficient dropping from 80 to 50 μV K^{-1} after 90 days, while other films have completely lost their n-type behavior in this timeframe.[138,139]

The air stability from this system is believed to be due to the high concentration of BPEI in the BPEI-DWNT deposition solution as well as the exfoliated graphene that may create a more

tortuous pathway for oxygen diffusion.[24] The n-type performance was improved by lowering the concentration of insulating BPEI and exchanging the PVP-graphene solution for water-stable graphene oxide (GO). After LbL assembly was conducted using BPEI-DWNT and GO, the film was subjected to a thermal treatment to reduce the graphene oxide and restore most of its conjugated structure. Using both of these techniques resulted in a power factor of 400 $\mu W\ m^{-1}K^{-2}$, but this film has much worse air stability.[140] Its air stability was improved by depositing a quadlayer system composed of BPEI, poly(acrylic acid) (PAA), and montmorillonite (MMT) clay on top of the thermoelectric film to create a "stacked" LbL coating (**Figure 2.10a**).[141] The 5 QL BPEI/PAA/BPEI/MMT coating dramatically improved the air stability of this film, while the power factor was only decreased by 25% (**Figure 2.10b,c**).

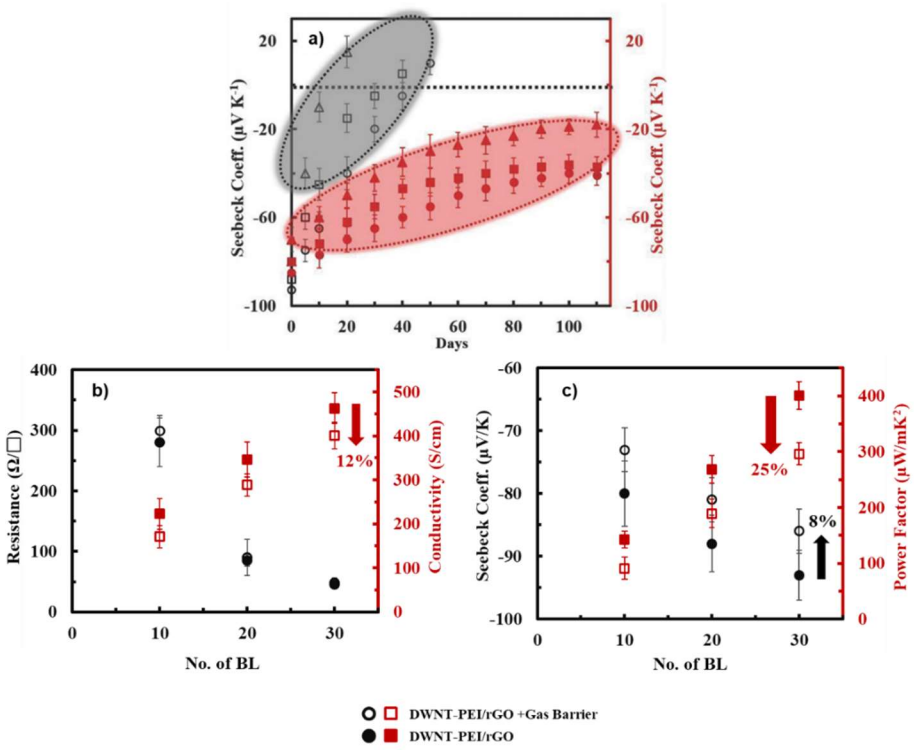

Figure 2.10. (a) Air stability with (red shapes) and without (black shapes) a gas barrier coating deposited on top of the PEI-DWNT/rGO film. **(b,c)** Thermoelectric properties before (closed shapes) and after (open shapes) the deposition of the gas barrier film.[140] Adapted with permission from Cho, C.; Bittner, N.; Choi, W.; Hsu, J.; Yu, C.; Grunlan, J. C. Thermally Enhanced N-Type Thermoelectric Behavior in Completely Organic Graphene Oxide-Based Thin Films. *Adv. Electron. Mater.* **2019**, 5 (11), 1800465.

2.6 Present Work

Layer-by-layer assembly is a promising polymer nanocomposite processing method for preparing thermoelectric materials with competitive power factors. While the previously discussed LbL-deposited thermoelectric composites exhibit good performance, the toolbox for improving them has been limited to changing the surfactant used to disperse these materials. Chapters III, IV, and V discuss post-deposition thermal and pre-deposition salt doping strategies to improve thermoelectric performance without changing the surfactant used to stabilize the carbon nanofillers. Both strategies result in dramatic improvements in power factor, and their ease of implementation allows them to be easily scalable towards depositing these systems over a larger area.

CHAPTER III

THERMOELECTRIC PERFORMANCE IMPROVEMENT OF POLYMER NANOCOMPOSITES BY SELECTIVE THERMAL DEGRADATION*

3.1 Introduction

The thermoelectric performance of organic materials can be improved by a variety of post-assembly treatments. For example, PEDOT:PSS-based materials can be improved through chemical and vapor treatments by altering the packing of PEDOT chains.[142] In addition, many thermal treatments have been shown to improve the thermoelectric performance by various mechanisms. Wang et al. observed a 20% increase in the power factor of a polyaniline/tellurium nanorod composite material using thermal annealing due to the modified carrier concentration imparted by the solvent trapped in the material.[143] Pura et al. showed that the annealing atmosphere plays a large role in improving the properties of TiO_2 nanoparticles.[144] They observed that annealing these nanoparticles in air increased the Seebeck coefficient, while an increased electrical conductivity was observed when the annealing was conducted under vacuum. Thermal treatments on various metal oxides (*e.g.* $Ca_3Co_4O_9$) result in reduced electrical conductivity due to electron/hole recombination from oxygen vacancies in the material, which results in a lower carrier concentration.[145,146]

*Reprinted with permission from Stevens, D. L.; Parra, A.; and Grunlan, J. C. Thermoelectric Performance Improvement of Polymer Nanocomposites by Selective Thermal Degradation, *ACS Applied Energy Materials* **2019**, *2* (8), 5975-5982.

Wolfe et al. reported a simultaneous increase in the Seebeck coefficient and electrical conductivity using a nickel ethanetetrathiolate polymer blend under mild annealing conditions (160 °C) due to the removal of the residual solvent that improves chain packing.[147]

In this chapter, a thermal treatment strategy of degrading the insulating components required to template the network of conductive nanofillers is presented. A 20 quadlayer PDDA/PEDOT:PSS-graphene/PDDA/PEDOT:PSS-DWNT film, with a thickness of approximately 20 nm (heated at 425 °C for 1 hour in argon), gives a simultaneous increase in the Seebeck coefficient and electrical conductivity to produce a power factor of 168 $\mu W\ m^{-1}\ K^{-2}$, which is an order of magnitude higher than the unheated control. This strategy for improving thermoelectric performance is attributed to the removal of insulating PDDA and PSS, while maintaining the interconnected conjugated network formed by carbon nanotubes and graphene. Thermogravimetric analysis (TGA) and X-ray photoelectron spectroscopy (XPS) demonstrate that PDDA and PSS are the primary components being removed at and below 425 °C. Ultraviolet photoelectron spectroscopy (UPS) analysis shows that the increase in the Seebeck coefficient is due to the Fermi level shift toward the valence band and a greater asymmetry in the density of states around the Fermi level. This strategy of thermally degrading insulating components can likely be used in a variety of organic materials to achieve improved thermoelectric behavior.

3.2 Experimental

3.2.1 Materials

Poly(diallyldimethylammonium chloride) (PDDA) (M_w = 200,000 – 350,000 g/mol, 20 wt % aqueous solution) was purchased from Sigma-Aldrich (Milwaukee, WI). Poly (3,4-ethylenedioxythiophene): poly (styrene sulfonate) (PEDOT:PSS) was purchased from Heraeus Precious Metals (Clevios PH 1000, Hanau, Germany). Double-walled carbon nanotubes (DWNT) were purchased from Continental Carbon Nanotechnologies Inc. (XB type, 1 μm length and 2 nm diameter, Houston TX) and graphene was purchased from XG Sciences (CX_750, platelet diameters of ≤ 2 μm and a thickness of ~3 nm, Lansing, MI). Silicon wafers (p-type, 100, University Wafer, Boston, MA), glass microscope slides (VWR International, Radnor, PA), and gold-coated silicon wafers (50 nm film, Substrata, Kitchener, ON) were used as the substrates for this study. Ti/Au quartz plated crystals were purchased from Maxtek, Inc. (Cypress, CA) for quartz crystal microbalance (QCM) measurements.

3.2.2 Preparation of Graphene and DWNT Suspensions

Water-based suspensions of 0.05 wt % DWNT and 0.1% graphene were made in 18 MΩ deionized (DI) water containing 0.06 wt % PEDOT:PSS. After suspending graphene and DWNT in PEDOT:PSS using a mortar and pestle, they were bath sonicated for 30 minutes each, followed by tip sonication in an ice bath for 30 minutes at a power of 15 W. This sonication cycle was repeated to ensure the suspensions were completely homogenized. The DWNT- PEDOT:PSS and graphene-PEDOT:PSS solutions were centrifuged at 4000 rpm for 20 minutes. The supernatant was decanted and used for coating.

3.2.3 Assembly of Multilayer and Dropcast Films

All substrates were cleaned with DI water, methanol, DI water, and then dried with compressed air. They were subsequently cleaned in a plasma chamber (Atto Plasma System, Thierry, Royal Oak, MI) to impart a negative surface charge before film deposition. LbL assembly was conducted using an automated coating system.[148] The substrate was initially submerged in a 0.25 wt % PDDA solution for 5 minutes, followed by rinsing with DI water and drying with compressed air. This initial deposition procedure was carried out identically for the PEDOT:PSS – graphene solution. The film was then dipped again into 0.25 wt % PDDA and finally the PEDOT:PSS – DWNT solution, for 1 minute each, with the same rinsing and drying procedure. The end of this sequence results in one PDDA/ PEDOT:PSS – graphene/ PDDA/ PEDOT:PSS – DWNT quadlayer (QL). For subsequent cycles, all immersion times were 1 minute. The pH of each solution was left unaltered. This coating procedure was followed identically on all substrates used in this study. PEDOT:PSS films were prepared by drop casting ~ 2 mL of the reagent solution onto a silicon wafer, followed by drying at 105 °C overnight. The PDDA:PSS complex was prepared by following a previously reported procedure.[149]

3.2.4 Film Characterization

Thickness of QL films deposited on Si wafers was measured using an α-SE ellipsometer (J.A. Woolam Co. Lincoln, NE) with a 632.8 nm laser held at a 70 ° angle. Mass deposited onto Ti/Au plated quartz crystals was monitored using a QCM (Inficon, East Syracuse, NY) between a frequency range of 3.8 – 6 MHz. The quartz crystal was left to stabilize for 5 minutes after each dipping cycle. Raman spectra on 20 QL films deposited on silicon wafers were collected using a

Jobin-Yvon Horiba Labram HR instrument (Piscataway, NJ) paired with an Olympus BX41 optical microscope (Waltham, MA). A 514.5 nm Ar-ion laser was used as the excitation source. The degradation of the multilayer film was studied using a Q50 TGA (TA instruments, New Castle, DE). The multilayer film sample (~5 mg), composed of 50 QL films deposited on glass slides removed with a razor blade, was heated at a rate of 10 °C $min.^{-1}$ and held at 150, 300, 375, and 425 °C for 60 minutes, under $N_{2(g)}$. Scanning electron microscopy (SEM) images were collected for 20 QL films deposited on Si wafers using a JEOL JSM-7500F field-emission scanning electron microscope (Peabody, MA). XPS spectra of 20 QL and drop-cast PEDOT:PSS films deposited on Si wafers were taken with an Omicron XPS/UPS system (Denver, CO) using a monochromatized DAR Mg X-ray source at 1253.6 eV, with an energy resolution of 0.8 eV. Reported XPS peaks were calibrated to the adventitious carbon in the C 1s peak at 284.8 eV. UPS spectra of 20 QL films deposited on gold-coated silicon wafers were collected with the same instrument using a HIS 13 UV source at 21.2 eV. A 3 V bias was applied to access the secondary electron cutoff of each sample in order to calculate the work function.

3.2.5 Heat Treatment

The 20 QL films deposited on glass slides and Si wafers were subjected to heat treatments under an argon atmosphere using a tube furnace (ThermoFisher Scientific F21135, Dubuque, IA). After purging the apparatus with argon for 20 minutes, the samples were heated to 150, 300, 375, or 425 °C at a rate of 10 °C/min and held at that temperature for 60 minutes. The samples were cooled to 100 °C in argon to avoid any oxidation upon cooling.

3.2.6 Thermoelectric Measurements

Film resistances on 8 x 12 mm nanocomposite thin films, deposited on glass slides, were measured using a Signatone Pro 4 four-point probe (Gilroy, CA) connected using a SCB-68 I/O connector block (National Instruments, Austin, TX) to a E3644A DC Power Supply and a 2400 Keithley multimeter (Cleveland, OH) at a 10 V operating voltage. The probe tips were 0.4 mm in diameter with a separation of 1.0 mm between the tips. The sheet resistance was calculated using $R_s = 4.23(V/I)$, where 4.23 is the correction factor based on the dimensions of the substrate relative to the spacing between the probes.[48] Electrical conductivity was found by taking the inverse of the product of the thickness and the sheet resistance. Carrier concentration was determined using Hall Effect measurements, with a commercial PPMS Dynacool instrument (Quantum Design, San Diego, CA), a magnetic field of ± 3 T and an electrical current of 1 mA. The Seebeck measurement was determined by using a home-built setup where two T-type thermocouples and two copper wires were used to measure the temperature gradient and generated voltage, respectively.[28] The measurement was conducted using a Keithley 2000 multimeter, a Lakeshore model 350 temperature controller (LakeShore Cryotronics, Westerville, OH) and operated using LabVIEW. The thermoelectric voltage across the film was measured at eight temperature differentials between -10 and 10 K. The reported Seebeck coefficient was the slope of the linear fit of the generated voltage as a function of temperature gradient plot, with a correlation coefficient greater than 0.99.

3.3 Results and Discussion

3.3.1 Multilayer Film Characterization

A schematic of layer-by-layer deposition from aqueous solutions is shown in **Figure 3.1a**. The chemical structures of each of the components is shown in **Figure 3.1b**. PDDA was selected as the polycationic component due to its use in previously studied conductive LbL composite films.[49,50] PEDOT:PSS was chosen for its ability to serve as both a conductive component and anionic stabilizer for graphene and DWNT.[29] Incorporating both DWNT and graphene into a multilayer film has been shown to provide better properties than composite films of either individual ingredient.[28,29] Cyclical deposition of PDDA, PEDOT:PSS-graphene, PDDA, and PEDOT:PSS-DWNT solutions results in the multilayer film shown in **Figure 3.1c**. One full cycle of deposition results in one quadlayer (QL). The PDDA/PEDOT:PSS-graphene/PDDA/PEDOT:PSS-DWNT quadlayer assembly results in a film that exhibits consistent incremental growth in terms of thickness and mass (**Figure 3.1d-e**). This growth behavior suggests minimal interdiffusion between ingredients, and that overall, the film composition remains constant during deposition.[49,150]

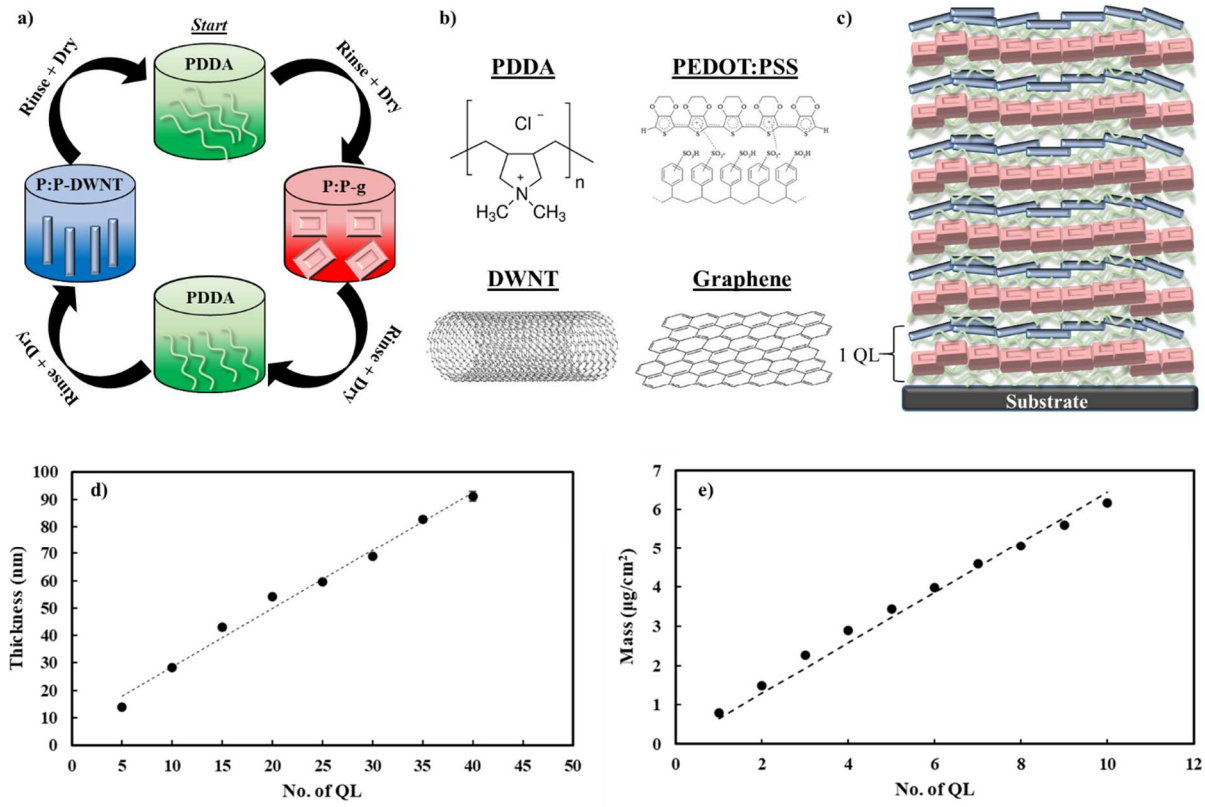

Figure 3.1. (a) Schematic of layer-by-layer assembly of thermoelectric quadlayers. **(b)** Chemical structures of the film constituents. **(c)** Schematic of the resulting multilayer film. **(d)** Film thickness and **(e)** mass as a function of quadlayers deposited.

Following deposition, assembled films were subjected to heating. The temperatures of interest were determined based on the degradation behavior of the insulating components of the film, PDDA and PSS, determined by TGA data obtained in a nitrogen gas environment **(Fig. 3.2)**. PDDA gives two distinct degradation peaks (near 300 and 400 °C), while PSS gives one major degradation peak near 300 °C. With these data in mind, the temperatures chosen were 150 (no degradation), 300 (PSS degradation), 375 (PSS degradation, with some PDDA degradation), and 425 °C (near complete degradation of all insulating components).

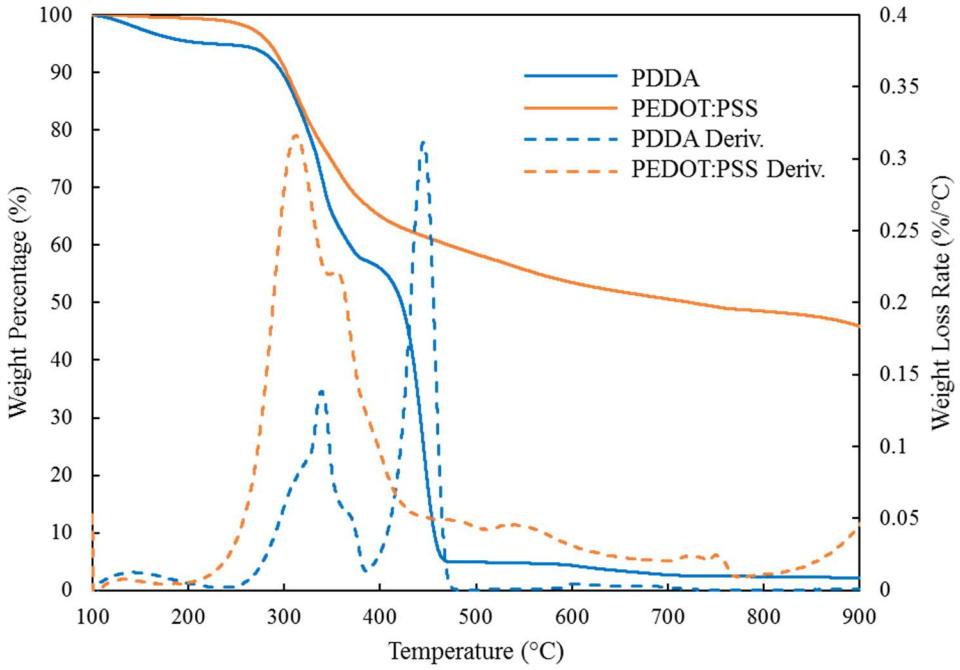

Figure 3.2. TGA curves of PDDA and PEDOT:PSS in a nitrogen atmosphere.

The thickness of 20 QL films exposed to these temperatures is shown in **Figure 3.3a**. Progressively thinner films are produced at higher temperatures due to more material being degraded and expelled from the film. **Figure 3.3b-f** shows SEM surface images of the films subjected to each temperature. Any cracks observed in these images are due to the conductive Pt/Pd coating. The samples heated at 375 and 425 °C expose underlying carbon nanotubes, which further confirms the removal of material. At the lower heating temperatures, the carbon nanofillers are fully engulfed by the insulating polymeric components used in multilayer assembly, hindering electron transport. Heating to higher temperatures uncovers the underlying conductive network of DWNT and graphene that allows for more favorable electron transport throughout the film. Raman spectra of these samples show the D-band of carbon nanotubes has a similar relative intensity to the G-band, which suggests no additional defects are created by the heat treatment **(Figure**

3.3g).[151] The large particles in these images correspond to PEDOT:PSS, whose shape is consistent with the particles observed in an SEM image of the dropcast film **(Figure 3.3h)**.

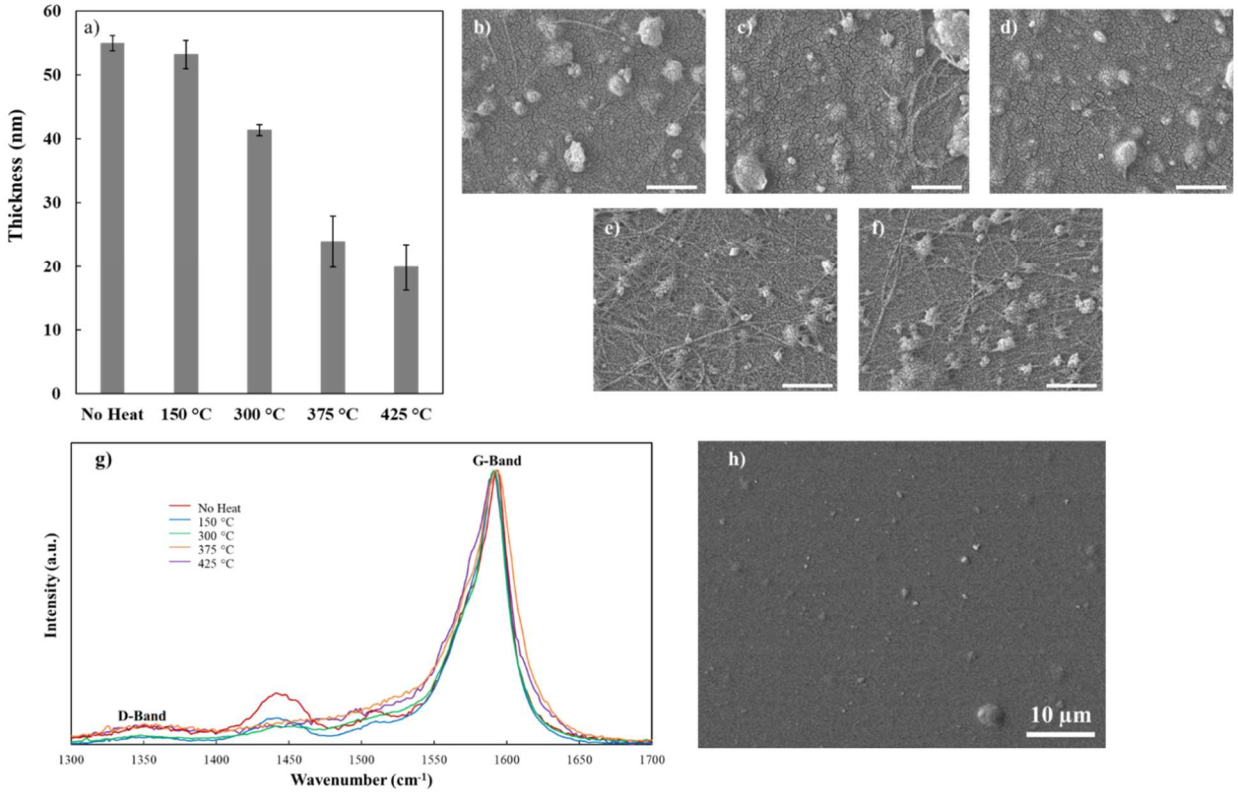

Figure 3.3. (a) Thickness of 20 QL films as a function of annealing temperature in an argon atmosphere. SEM images of 20 QL films subjected to **(b)** no thermal treatment, **(c)** 150, **(d)** 300, **(e)** 375, and **(f)** 425 °C for 60 minutes. The scale bars represent 500 nm. **(g)** Normalized Raman spectra of 20 QL samples subjected to each thermal treatment temperature. **(h)** SEM image of a drop cast PEDOT:PSS film.

Thermogravimetric analysis was conducted observe the degradation of the film components at 150 300, 375, and 425 °C under $N_{2(g)}$. In this case, 50 QL films were assembled on glass, followed by the removal of the film using a razor blade. The TGA curves in **Figure 3.4** show the QL film degradation held at a 60-minute isotherm for each of the evaluated temperatures, along with individual TGA curves of the film ingredients. These data confirm significant PDDA and PEDOT:PSS degradation at each evaluated temperature above 150 °C. The PDDA thermogram

shows significant degradation after each isotherm, but a significant amount of PEDOT:PSS remains after the isotherm at 425 °C. PEDOT is likely the primary component remaining beyond 425 °C due to the vast majority of the PDDA:PSS complex degrading at 375 °C. The PDDA:PSS complex also shows minimal degradation at 300 and 425 °C. All of these observations in degradation behavior for the PDDA:PSS complex are consistent with a previous report.[152]

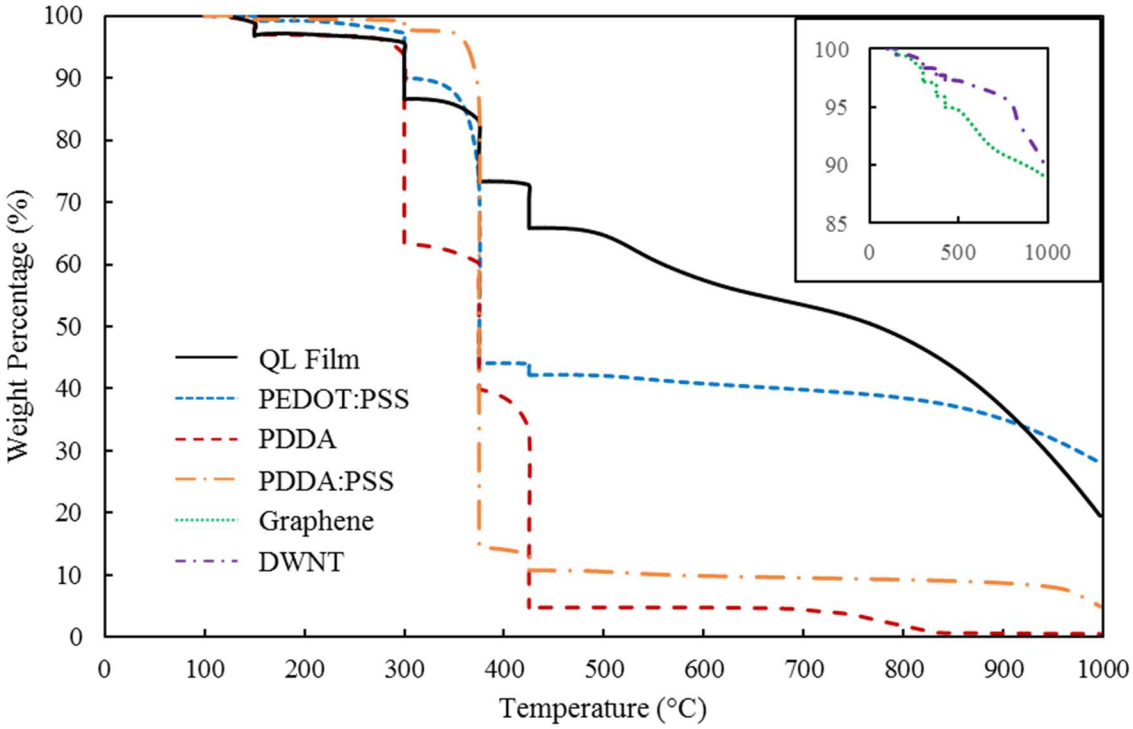

Figure 3.4. TGA of the QL film, its individual constituents, and the PDDA:PSS polyelectrolyte complex under $N_{2(g)}$. Isotherms of 60 minutes were conducted at 150, 300, 375, 425 °C.

XPS S 2p spectra were collected to further elucidate the degradation of PDDA and PSS in the film. The two separate peaks shown in **Figure 3.5** correspond to the two different binding environments of sulfur within PEDOT:PSS (the thiophene ring in PEDOT (163.9 eV) and the sulfonate group in PSS (167.6 eV)).[153–156] These spectra confirm that the PSS begins to degrade

within the multilayer first. Atomic percentages for each sulfur atom obtained from peak deconvolutions are shown in **Table 3.1**. The relative amount of the PEDOT sulfur begins to increase at 300 °C, from 13 to 27%, due to the degradation of PSS within the film. The amount of PEDOT relative to PSS reaches a maximum of 87% after exposure to 375 °C. The stark difference in sulfur atomic percentages from 300 to 375 °C suggests that the rapid PDDA:PSS complex degradation occurs at this temperature and that a majority of the PSS complexes with PDDA during film deposition. This idea is further supported by doing the same XPS analysis on thermally treated dropcast PEDOT:PSS films. After heating at 300 °C, the amount of the PEDOT sulfur increases from 29 to 79% in the film, which is supported by the TGA of PSS under nitrogen because its only major degradation occurred near 300 °C. As PEDOT does not become the majority sulfur-containing species in the multilayer film until heating to 375 °C, it is likely that the PDDA:PSS complex is being removed at 375 °C. For both the dropcast PEDOT:PSS and multilayer film, the atomic percentage of sulfur in PEDOT decrease slightly at 425 °C, as compared to 375 °C, which suggests the initial degradation of PEDOT in the film.

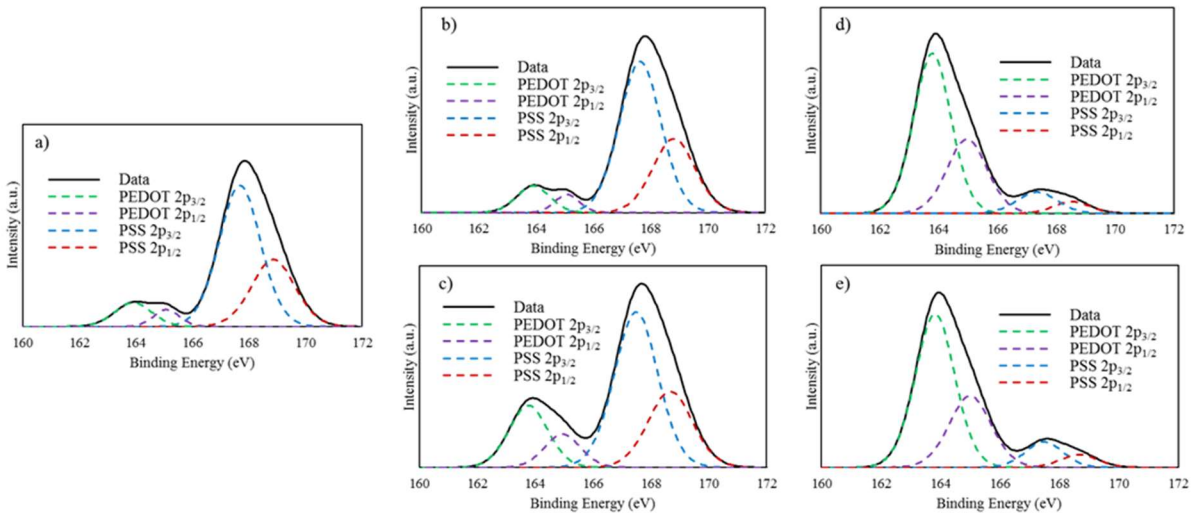

Figure 3.5. XPS S 2p spectra of 20 QL films subjected to **(a)** no thermal treatment, **(b)** 150, **(c)** 300, **(d)** 375, and **(e)** 425 °C.

Table 3.1. Atomic percentages of sulfur pertaining to PEDOT and PSS in the thermally treated 20 QL and dropcast PEDOT:PSS film.

Sample	20 QL PEDOT %	20 QL PSS %	Dropcast PEDOT %	Dropcast PSS %
No Heat	13	87	29	71
150 °C	13	87	30	70
300 °C	27	73	79	21
375 °C	87	13	88	12
425 °C	86	14	73	27

3.3.2 Thermoelectric Behavior

Thermoelectric properties were studied as a function of heat treatment temperature to determine how different extents of film degradation affect performance. **Figure 3.6a** shows the changes in sheet resistance and electrical conductivity. The electrical conductivity increases slightly (from 63.5 ± 2.6 S cm^{-1} to 78.1 ± 4.7 S cm^{-1}) after heating at 150 °C, which is likely due to film densification through water removal.[147] The conductivity after heating at 300 °C yields a much lower value of 38.0 ± 1.4 S cm^{-1}, and is attributed to the dissociation of the quaternary ammonium salt to chloromethane and the trivalent nitrogen repeat unit no longer associated in the PDDA:PSS complex.[157] The formation of more insulating molecules from this dissociation is assumed to reduce the electrical conductivity. After removing the PDDA:PSS complex by heating at 375 °C, a conductivity of 170 ± 13 S cm^{-1} is achieved. The maximum conductivity of 342 ± 23 S cm^{-1} is achieved at 425 °C, owing to the near complete degradation of PDDA and PSS in the film, as confirmed by TGA **(Figure 3.4)**. This five-fold improvement in conductivity further suggests that the nanoparticle network is maintained, which is also supported by SEM images **(Figure 3.3e-f)**.

Seebeck coefficient and power factor as a function of treatment temperature are shown in **Figure 3.6b**. The Seebeck coefficient increases up to a maximum value of 79 ± 3 μV K^{-1} after exposure to 375 °C, but then decreases to 70 ± 2 μV K^{-1} after heating at 425 °C. The removal of insulating material increases the electron carrier concentration within the film, which typically reduces the Seebeck value.[155] In this case, the removal of the PDDA:PSS complex at 375 °C complex results in a 35% increase in Seebeck coefficient compared to the unheated control, which suggests an increase in carrier mobility. The beginning of PEDOT degradation at 425 °C is likely compromising carrier mobility along the polymer backbone, which may explain the lower Seebeck

value observed at this temperature. Despite the lower Seebeck value, the calculated power factor increases from 16.9 ± 0.8 μW m^{-1} K^{-2} to 168 ± 11 μW m^{-1} K^{-2} after heating at 425 °C. In addition to the marked improvement in power factor upon degrading a majority of the insulating material, the S and σ increase simultaneously, which is not commonly observed in thermoelectric materials. This behavior was previously reported for carbon nanotube-graphene composites and was attributed to the increase in carrier mobility caused by the lower contact resistance between the DWNT and graphene in the film.[28,29,125]

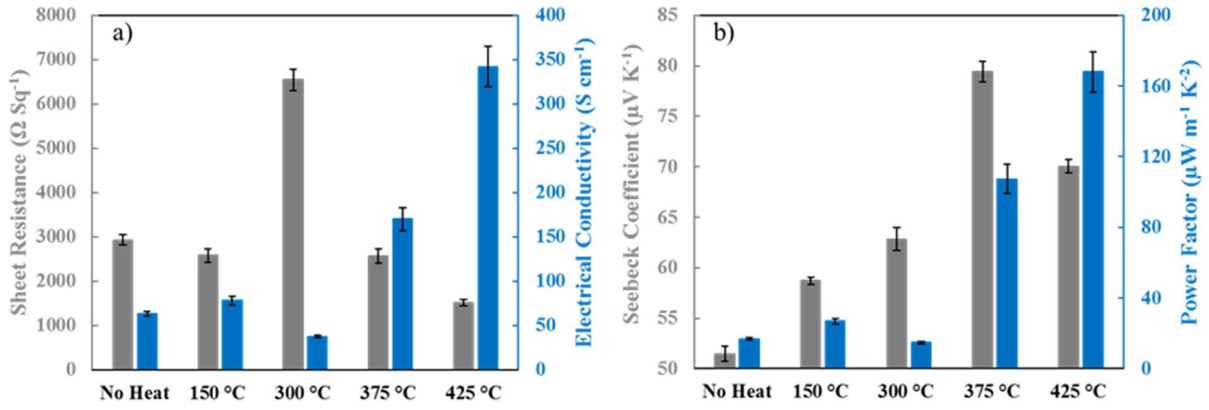

Figure 3.6. (a) Sheet resistance and electrical conductivity, and **(b)** Seebeck coefficient and power factor for 20 QL films as a function of thermal treatment temperature.

The electrical conductivity (σ) for a metallic conductor can be found using $\sigma = ne\mu$, where n is the carrier concentration, e is the elementary charge of an electron, and μ is the carrier mobility. This equation suggests only changes in the carrier concentration and carrier mobility influence the electrical conductivity of the material. It is well established that the Seebeck coefficient for a material that exhibits metallic conduction decreases as carrier concentration increases.[3,8] If the Seebeck coefficient and electrical conductivity improve simultaneously, it suggests that increased

carrier mobility is the primary driver for this behavior. In the present nanocomposite thin films, the Hall Effect measured carrier concentration increases by about 7x after the PDDA:PSS complex is degraded with heating (relative to the unheated control), as shown in **Figure 3.7**. This increased carrier concentration results in a slightly lower carrier mobility, which typically correlates to a lower Seebeck coefficient. When taken together, these results suggest that these films do not exhibit metallic conduction, so considerations such as the change in the density of states near the Fermi level must be accounted for.[86,158]

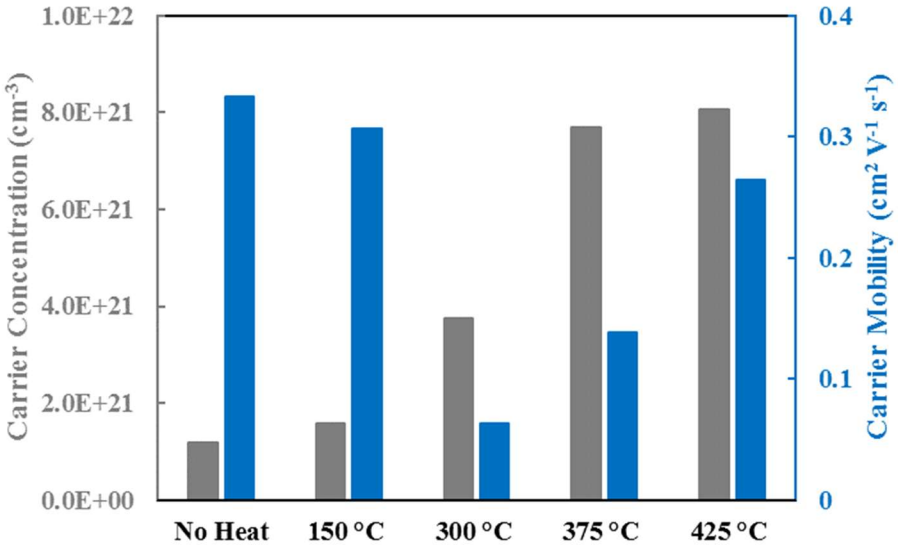

Figure 3.7. Carrier concentration and carrier mobility of 20 QL films, as a function of thermal treatment temperature, from Hall Effect measurements.

Ultraviolet photoelectron spectroscopy (UPS) was used to observe how changes in the density of valence electronic states near the Fermi level are connected to changes in the Seebeck coefficient. According to the Mott formula, $S \propto \left(\frac{d\{\ln \sigma(E)\}}{dE}\right)_{E=E_F}$,[7,159] and S can be shown to have an energy-dependent conductivity term and an energy-dependent carrier mobility term. As a result, this relationship provides a direct connection between the Seebeck coefficient and the shape of the

valence density of states at the Fermi level, assuming the charge carrier mobility has a negligible effect. UPS curves show the density of valence electronic states near E_F, so variances in the slope near E_F are indicative of changes in S. Twenty quadlayer films coated onto silicon wafers with a 50 nm thick Au overcoat (and heated to 150, 300, 375, and 425 °C) were used for UPS analysis. As shown in **Figure 3.8**, progressively steeper slopes occur with increasing temperature, suggesting larger Seebeck coefficients. The fact that the 425 °C sample has a slope greater than the 375 °C one, despite having a lower Seebeck coefficient, means the carrier mobility term in the Mott relation must be taken into account.[160] The complete removal of PDDA achieved at 425 °C may result in a net increase in carrier mobility despite a small amount of PEDOT degradation, which is suggested by its maximum conductivity value. To further understand these changes in the Seebeck coefficient, work function and highest molecular orbital (HOMO) edges were calculated, as shown in **Table 3.2**. A lower HOMO edge with increasing work function is indicative of a lower E_F, which is observed for 20 QL samples heated to 375 and 425 °C.[136] The lower E_F value indicates stronger p-type conversion that corresponds to a larger S value.[161]

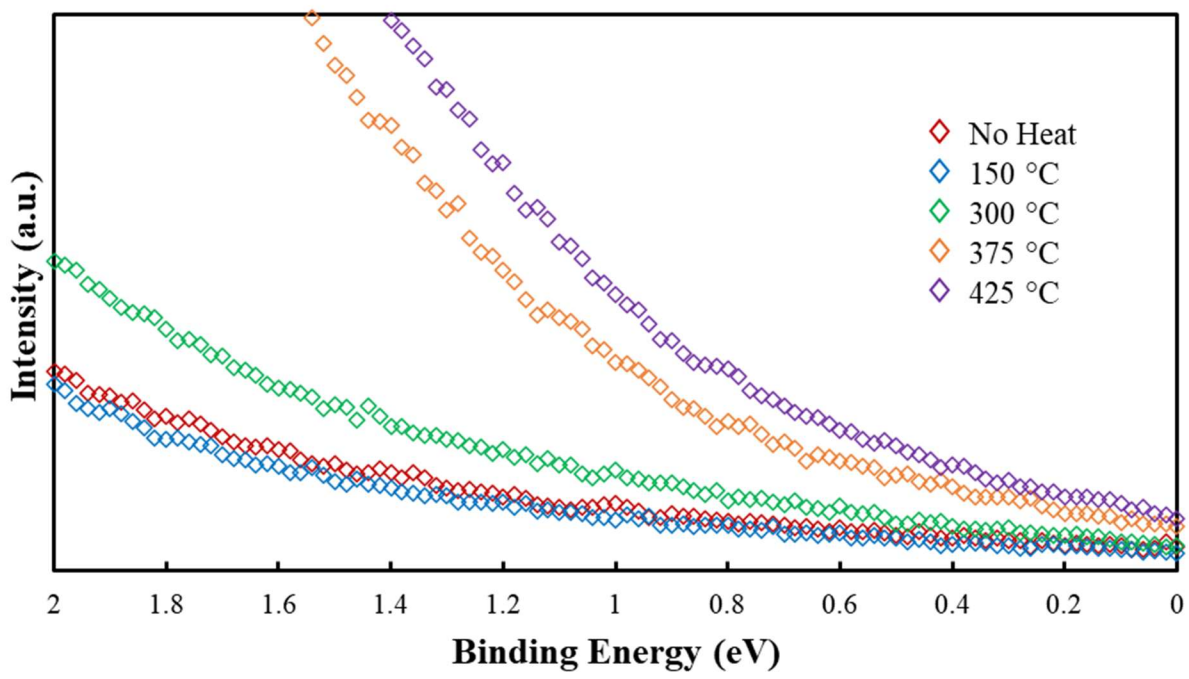

Figure 3.8. UPS spectra of 20 QL films treated at various temperatures. The Fermi level is normalized to 0 eV.

Table 3.2. Valence band edge and work function calculated for each 20 QL sample.*

Thermal Treatment Temperature	$E_{HOMO,Onset}$ (eV)	Work Function (eV)
No Heat	3.3	4.7
150 °C	2.9	4.8
300 °C	2.8	3.6
375 °C	1.4	4.9
425 °C	1.2	4.0

*HOMO edges and work functions were calculated using previously reported methods.[162,163]

3.4 Conclusions

A layer-by-layer assembled film was heated at varying temperatures in an inert atmosphere to study how degradation of the film components affects the thermoelectric properties of the film. A 20 QL film (~20 nm thick) composed of PDDA, PEDOT:PSS, graphene, and DWNT, heated to 425 °C for 60 minutes, achieved an electrical conductivity of 342 ± 23 S cm^{-1} and a Seebeck coefficient of 70 ± 2 μV K^{-1}, which results in a power factor of 168 ± 11 μW m^{-1} K^{-2}. This power factor is an order of magnitude greater than the unheated control, and is believed to be due to the removal of insulating PDDA and PSS, while maintaining the conductive network of DWNT and graphene formed during film assembly. This simple post-treatment could potentially be employed more broadly to fabricate high performing, polymer-based thermoelectric materials for numerous lightweight, low power applications.

CHAPTER IV

SALT DOPING TO IMPROVE THERMOELECTRIC POWER FACTOR OF POLYMER NANOCOMPOSITE THIN FILMS*

4.1 Introduction

PEDOT:PSS is one of the most important organics used to prepare p-type thermoelectric materials. PEDOT:PSS is a water soluble polymer complex where hydrophobic and electron conducting PEDOT chains are stabilized in water by the sulfonic acid and sulfonate moieties on PSS.[85,86] From these attractive stabilizing forces, PSS tends to encapsulate aggregates of PEDOT chains in water, and the large distance between PEDOT chains in this native conformation lends itself to very poor thermoelectric properties.[92,164–166] Strategies that weaken the interactions between PEDOT and PSS are imperative to improve the thermoelectric properties of PEDOT:PSS-based thermoelectric materials. While many strategies focus on modifying the carrier concentration on PEDOT chains through acid-base chemistry,[82,87] one strategy that simultaneously improves the Seebeck coefficient and electrical conductivity is the exposure of an inorganic salt (*e.g.* $CuCl_2$, $ZnCl_2$, etc.) solvated in a polar organic solvent (*e.g.* DMF).[92,95] Softer, more polarizable cations were found to be more effective at simultaneously increasing the Seebeck coefficient and electrical conductivity of PEDOT:PSS films due to their ability to remove PSS more efficiently from the film through charge screening effects.

---

*Reprinted with permission from Stevens, D. L.; Gamage, G. A.; Ren, Z.; and Grunlan, J. C., Salt Doping to Improve Thermoelectric Power Factor of Organic Nanocomposite Thin Films, *RSC Adv.* **2020**, *10*, 11800-11807 – Published by The Royal Society of Chemistry.

Removing more PSS results in larger carrier mobilities, which is consistent with a simultaneous improvement in the Seebeck coefficient and electrical conductivity.

In this chapter, salt was used to separate PEDOT and PSS prior to LbL deposition to prepare polymer nanocomposite thin films. KBr was added to a PEDOT:PSS solution to weaken the interactions between the two components, followed by DWNT dispersion by means of ultra-sonication. The thermoelectric properties of a 20 bilayer (BL) thin film were analyzed as a function of the concentration of KBr dopant. A 20 BL PDDA/PEDOT:PSS – DWNT film doped with 3 mmol of KBr (~46 nm thick) exhibits an electrical conductivity of 1,479 S cm^{-1} and a Seebeck coefficient of 65.1 μV K^{-1}, which results in a power factor of 626 μW m^{-1} K^{-2}. This power factor is six times larger than the undoped control, and is attributed to an increase in electrical conductivity without a decrease in the Seebeck coefficient from the greater proportion of DWNT that is deposited as a result of doping. This work demonstrates the ability of salt to improve the power factor of multilayer polyelectrolyte nanocomposites, which can be utilized for low temperature thermoelectric power generation applications.

4.2 Experimental

4.2.1 Materials

Poly (diallyldimethylammonium chloride) (PDDA) (M_w = 200,000 – 350,000 g/mol, 20 wt % aqueous solution) and KBr (>99%) were purchased from Millipore-Sigma (Milwaukee, WI). Poly(3,4-ethylenedioxythiophene): poly (styrene sulfonate) (PEDOT:PSS) was purchased from Heraeus Precious Metals (Clevios PH 1000, Hanau, Germany). Double-walled carbon nanotubes

(DWNT) were purchased from Continental Carbon Nanotechnologies Inc. (XB type, 1 μm length and 2 nm diameter, Houston, TX). Each chemical was used as received and all solutions were prepared using 18 MΩ deionized (DI) water. Silicon wafers (p-type, 100, University Wafer, Boston, MA) and 179 μm poly (ethylene terephthalate) (PET) (ST 505, Tekra Crop., New Berlin, WI) were used as the substrates in this study.

4.2.2 Preparation of PEDOT:PSS (KBr) – DWNT Suspensions

KBr (1-4 mmol) was added to 5 g of Clevios PH 1000, similar to a previous report.[73] After doping PEDOT:PSS with KBr, 0.05 g of DWNT was suspended in the KBr-PEDOT:PSS solution using a mortar and pestle. DI water was added to adjust the concentration of PEDOT:PSS and DWNT to 0.06 wt % and 0.05 wt %, respectively. These DWNT suspensions were bath sonicated for 30 minutes, followed by tip sonication in an ice bath for 30 minutes at 15 W. This sonication cycle was repeated to ensure the suspensions were completely homogenized. The PEDOT:PSS (KBr)-DWNT solutions were centrifuged at 4000 rpm for 20 minutes. The supernatant was separated from the gelatinous precipitate using a pipet and used for coating.

4.2.3 Layer-by-Layer Assembly

All substrates were cleaned using a sequence of rinses (DI water, methanol, DI water), and then dried with compressed air. Silicon wafers and PET substrates were subsequently cleaned in a plasma chamber (Atto Plasma System, Thierry, Royal Oak, MI) or by corona treatment (BD-20C, Electro-Technic Products Inc., Chicago, IL), respectively, to impart a negative surface charge before film deposition. LbL assembly was conducted using an automated coating system.[148] The

substrate was initially submerged in a 0.25 wt % PDDA solution for five minutes, followed by rinsing with DI water and drying with compressed air. This initial deposition procedure was followed identically for the PEDOT:PSS (KBr) – DWNT solution. The end of this sequence results in one PDDA/PEDOT:PSS (KBr) – DWNT bilayer (BL). For subsequent cycles, all depositions times were one minute and the pH of both solutions were unadjusted. This coating procedure was followed identically for all substrates used in this study.

4.2.4 Film Characterization

Thickness and refractive index of films deposited on Si wafers were measured using an α-SE ellipsometer (J.A. Woolam Co. Lincoln, NE), with a 632.8 nm laser held at a 70 ° angle. Raman spectra on 20 BL films deposited on silicon wafers were collected using a Jobin-Yvon Horiba Labram HR instrument (Piscataway, NJ), equipped with a 514.5 Ar-ion laser and paired with an Olympus BX41 optical microscope (Waltham, MA). Topology of 20 BL films deposited on a silicon wafer were collected using a Dimension Icon atomic force microscope (AFM) (Bruker, Billerica, MA). AFM probes (HQ:NSC35/Al BS, Micromasch USA Watsonville, CA) had a force constant of 5.5 – 16 N/m and a tip radius of ~8 nm. Topographic AFM images were collected over a 5 x 5 μm area, with a scan speed of 0.5 Hz and 512 scans per line. XPS spectra of 20 BL films deposited on Si wafers were taken with an Omicron XPS/UPS system (Denver, CO), using a monochromatic DAR Mg X-ray source at 1253.6 eV, with an energy resolution of 0.8 eV. Reported XPS peaks were calibrated to the adventitious carbon peak in the C 1s region at 284.8 eV.

4.2.5 Thermoelectric Measurements

Film resistance of 8 x 12 mm nanocomposite thin films, deposited on PET, were measured using a Signatone Pro 4 four-point probe (Gilroy, CA) connected using a SCB-68 I/O connector block (National Instruments, Austin, TX) to a E3644A DC Power Supply and a 2400 Keithley multimeter (Cleveland, OH) at an operating voltage of 10 V. The probe tips were 0.4 mm in diameter with a separation of 1.0 mm between the tips. The sheet resistance was calculated using $R_s = 4.23(V/I)$, where 4.23 is the correction factor based on the dimensions of the substrate relative to the spacing between the probes.[48] Electrical conductivity was found by taking the inverse of the product of the thickness and the sheet resistance. Temperature-dependent resistance data were acquired using a commercial Dynacool Physical Property Measurement System (PPMS) (Quantum Design, San Diego, CA) using a four-point probe setup. The resistivity was calculated by multiplying the measured resistance by the ratio of the area divided by the length of the sample. The inverse of the resistivity is the electrical conductivity of the sample. Temperature-dependent carrier densities were acquired by Hall Effect measurements in a van der Pauw geometry using the same PPMS Dynacool instrument, with a magnetic field of ± 3 T and an electrical current of 500 μA. Carrier mobility values were acquired by using: $\sigma = ne\mu$, where σ is the electrical conductivity (S cm^{-1}), n is the carrier concentration (cm^{-3}), e is the elementary charge (C), and μ is the carrier mobility ($cm^2\ V^{-1}\ s^{-1}$). The Seebeck coefficient was measured with a home-built setup using a previously reported method.[28,29] The thermoelectric voltage across the film was measured at eight different temperature differentials between 0 and 10 K. Reported Seebeck coefficients

came from the slope of the linear fit to the voltage vs. temperature gradient across the film, with its y-intercept fixed at 0 V. The correlation coefficient for each linear fit was at least 0.99.

4.3 Results and Discussion

4.3.1 Film Thickness and Composition

Figure 4.1a shows the layer-by-layer deposition process used in this study, as well as an illustration of the resulting multilayer film. **Figure 4.1b** shows the chemical structures of the ingredients used to prepare these films. LbL films comprised of PDDA and PEDOT:PSS-DWNT were used as a model system that has exhibited excellent thermoelectric behavior.[28,29,50] PEDOT:PSS was used as a conductive constituent and anionic polymer surfactant to effectively disperse DWNT in water. KBr was chosen as a dopant for this system due to its prevalence in polyelectrolyte multilayer, its study in LbL-assembled films, and its larger atomic size of K^+ relative to Na^+.[27,92] Larger salt ions have a larger doping efficiency on polyelectrolyte multilayers due to their effects on the surrounding water structure.[22,27]

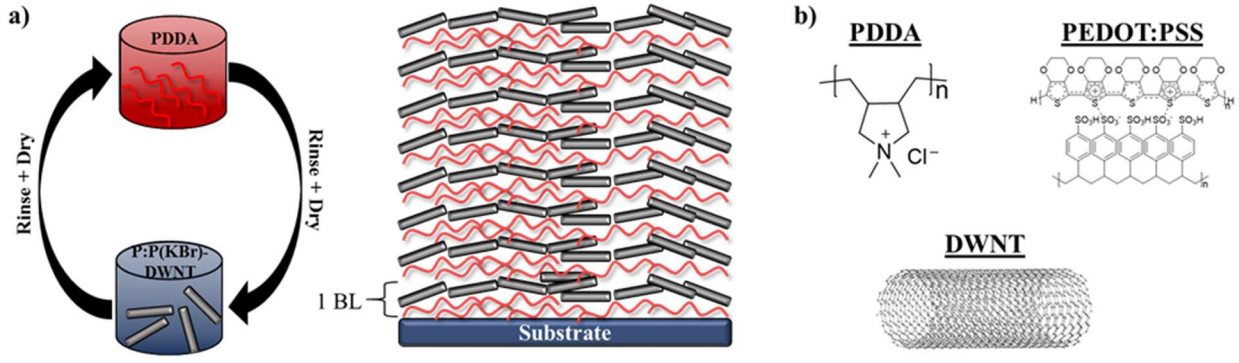

Figure 4.1. (a) Schematic of layer-of-layer deposition and **(b)** chemical structures of each major film component.

The influence of KBr concentration on the growth of PDDA/PEDOT:PSS (KBr)-DWNT films is shown in **Figure 4.2a**. Doping PEDOT:PSS with KBr results in thicker films as compared to the undoped control due to salt-induced charge screening. In the preparation of polyelectrolyte multilayers, salt is used to screen charged repeat units, which requires more polymer to overcompensate the surface charge of the previously deposited layer and results in thicker films. Interestingly, adding more KBr to the PEDOT:PSS-DWNT solution decreases film thickness, which may be due to PSS being removed from solution after centrifuging. Previous reports have shown that when PEDOT:PSS films are treated with a salt or ionic liquid, PEDOT and PSS disassociate from one another due to an ion exchange reaction (KBr + PEDOT:PSS → K:PSS + PEDOT:Br), which results in PSS removal.[92,95,159] Furthermore, increasing the amount of KBr results in larger refractive indices up to a concentration of 3 mmol KBr **(Fig. 4.2b)**. The decreased film thickness coupled with a larger refractive index, with increasing the amount of KBr, suggest greater film density.[167]

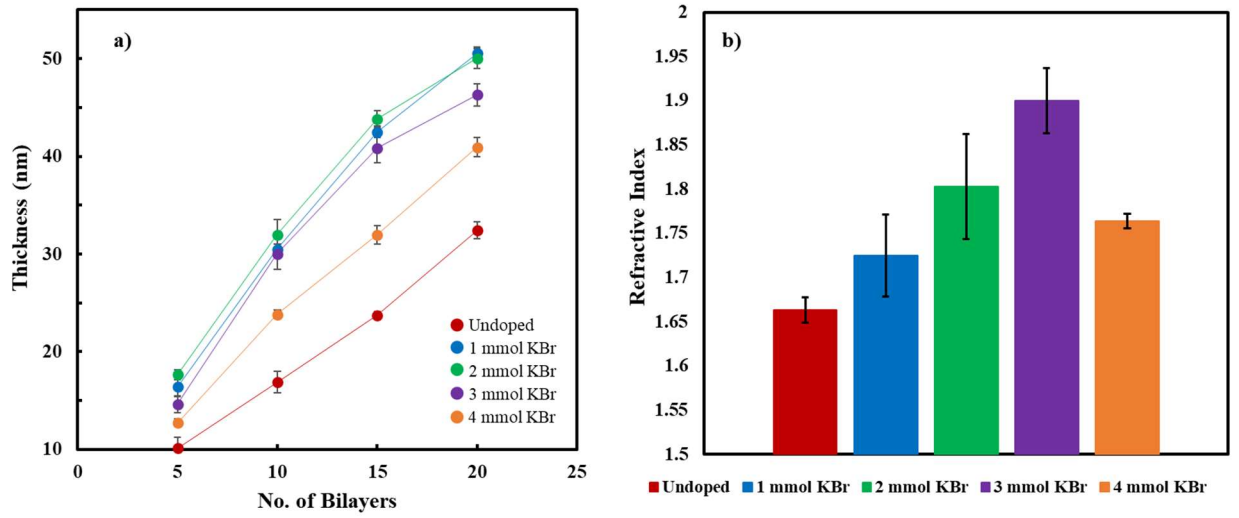

Figure 4.2. (a) Film thickness as a function of bilayers deposited, with varying KBr concentration. **(b)** Refractive index of 20 BL films as a function of KBr concentration.

Raman and XPS S 2p spectra were collected to probe any variations in film composition. XPS measurements conducted on PEDOT:PSS result in two peaks that correspond to the different local bonding environments of sulfur (the thiophene ring in PEDOT (~163.9 eV) and the sulfonate group in PSS (~ 167.6 eV)). Normalized XPS spectra of 20 BL films show that an increase in the PEDOT:PSS ratio is achieved with the addition of KBr **(Fig. 4.3a)**. Some PSS is being removed during centrifugation due to the ion exchange reaction between PEDOT:PSS and KBr. This observation is consistent with the thickness data, and may account for the steadily decreasing thickness as a function of KBr concentration. The maximum PEDOT:PSS ratio is achieved with 2 mmol KBr. Adding 3 mmol KBr does not substantially change the PEDOT:PSS ratio in the film, which suggests the changes in film thickness and density are due to a different amount of DWNT. Further increasing the KBr concentration to 4 mmol begins to decrease the PEDOT:PSS ratio, which may suggest that there is less PEDOT:PSS in the multilayer film.

Raman spectra normalized to the G band (~ 1590 cm^{-1}) of DWNT gathered on 20 BL films are shown in **Figure 4.3b**. The peak near 1430 cm^{-1} corresponds to the C=C symmetric stretch in PEDOT, so these spectra compare the relative amounts of DWNT to PEDOT.[87] The amount of PEDOT relative to DWNT gradually increases and reaches a maximum proportion at 2 mmol KBr, but then drastically decreases when comparing the 2 mmol to 3 mmol KBr-doped samples, indicating that a greater proportion of DWNT is deposited relative to PEDOT:PSS in tandem with an increase in film density **(Figure 4.2b, Figure4. 3b-c)**. It is noteworthy that increasing the KBr concentration from 3 mmol to 4 mmol KBr results in a lower PEDOT:PSS ratio, but a higher amount of DWNT relative to PEDOT, which suggests that much less PEDOT:PSS is incorporated in the film than the other KBr-doped films.

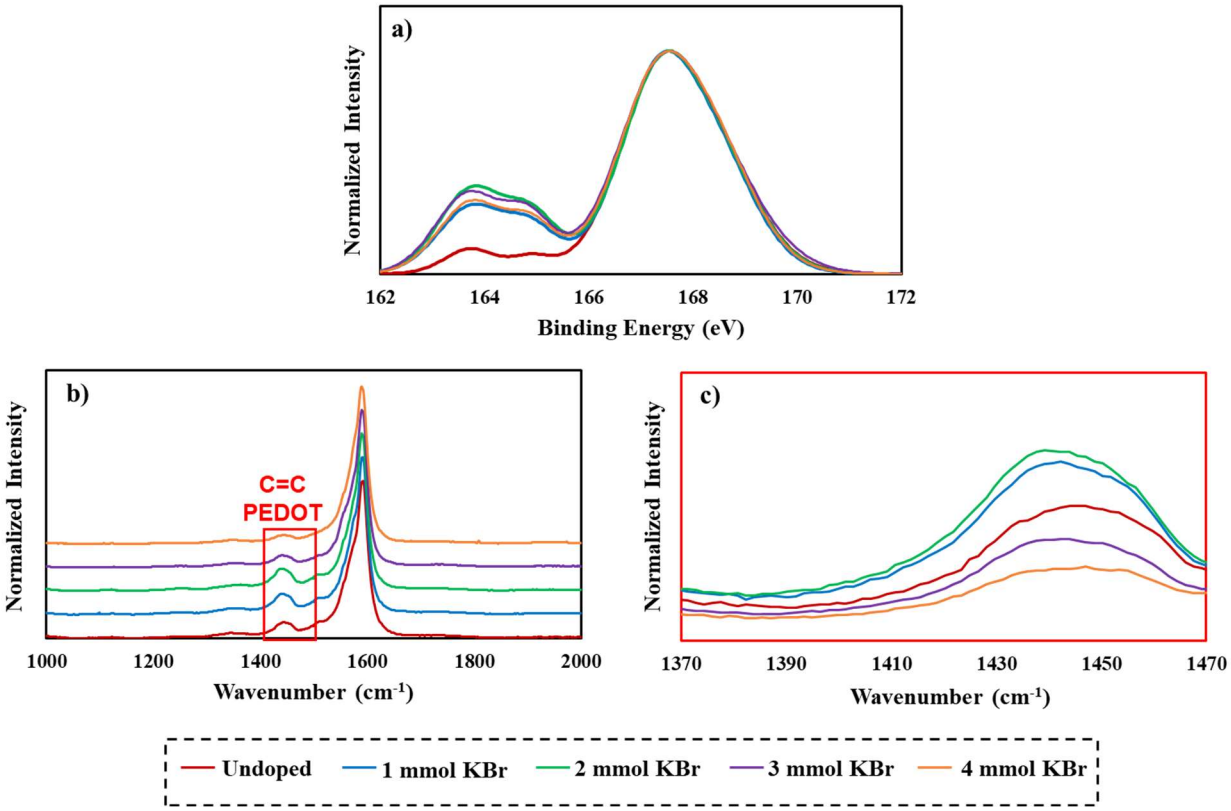

Figure 4.3. (a) Normalized XPS S 2p spectra and **(b)** Raman spectra of 20 BL films as a function of KBr concentration. **(c)** Normalized Raman spectra of 20 BL films, focusing on the peak corresponding to the C=C symmetric stretch in PEDOT.

4.3.2 Thermoelectric Properties of KBr-Doped Films

Thermoelectric properties were evaluated as a function of KBr concentration to investigate how the amount of dopant affects thermoelectric performance. **Figure 4.4a** shows the sheet resistance and electrical conductivity acquired at room temperature. The electrical conductivity of the undoped sample increases from 238 ± 10 S cm^{-1} to 471 ± 30 S cm^{-1} after adding 1 mmol KBr. The conductivity at 2 mmol KBr increases modestly to 544 ± 15 S cm^{-1}. The maximum conductivity of 1,479 ± 78 S cm^{-1} is achieved with 3 mmol KBr, which is ~6x larger than the undoped control. This improvement is attributed to a large increase in the carrier density **(Fig.**

4.4b). Adding 4 mmol KBr results in a lower electrical conductivity value of 1068 ± 28 S cm^{-1}, which is likely due to the lower amount of PEDOT and PSS in solution to effectively disperse DWNT. Insufficient PSS in the DWNT solution may lead to excessive bundling, resulting in a lower electrical conductivity.

The Seebeck coefficient and power factor as a function of KBr concentration is shown in **Figure 4.4c**. Interestingly, the maximum Seebeck coefficient of 72 ± 4.4 μV K^{-1} is achieved at 1 mmol KBr. The value of the Seebeck coefficient slightly decreases at 2 and 3 mmol KBr (68.1 ± 1.4 μV K^{-1} and 65.1 ± 1.5 μV K^{-1}, respectively). When adding 4 mmol KBr, the Seebeck coefficient significantly decreases to 57.4 ± 1.4 μV K^{-1}. Relatively large Seebeck coefficients for LbL-assembled thermoelectric nanocomposites containing DWNT and graphene have been attributed to increased carrier mobility, but these films used polyaniline as the polycationic component. Recently, a thermoelectric film using PDDA exhibited an improved Seebeck coefficient due to a greater instantaneous rate of change of the energy-dependent conductivity near E_F, even with a slightly lower carrier mobility.[168] This observation also resulted in a greater asymmetry in the density of states near E_F, which is another established method of increasing the Seebeck coefficient.[8] Previous reports for PEDOT:PSS films show an increase in the Seebeck coefficient with the removal of insulating PSS, which has been attributed to an increase in carrier mobility with the decreased π-π stacking distances between PEDOT chains. PSS removal is accompanied by a large increase in carrier density, so the similar Seebeck coefficients observed as a function of KBr concentration may be a result of the increasing energy-dependent electrical conductivity near E_F and the increasing carrier density canceling each other out. The significant decrease in the Seebeck coefficient from adding 4 mmol KBr might be where the drawbacks in carrier density outweigh the greater asymmetry observed in the density of states. Increased power factors were

observed as a function of KBr concentration primarily due to the improvement in the electrical conductivity. The maximum power factor of 626 ± 39 μW $m^{-1}K^{-2}$ is achieved using 3 mmol KBr, which is 6x larger than the undoped control. It is noteworthy that the electrical conductivity improves six-fold with minimal decrease in the Seebeck coefficient, suggesting that this salt doping strategy decouples these parameters.

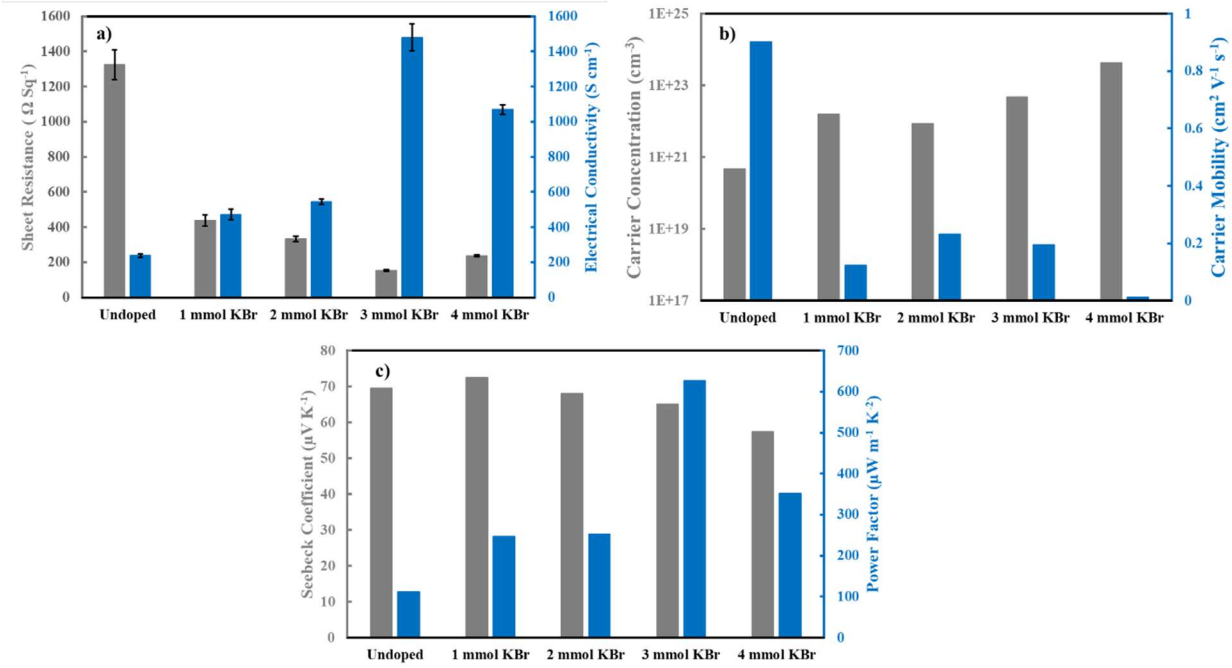

Figure 4.4. (a) Sheet resistance and electrical conductivity, **(b)** Seebeck coefficient and power factor, and **(c)** carrier concentration and carrier mobility of 20 BL films as a function of added KBr.

4.3.3 Temperature-Dependent Electrical Conductivity

Temperature-dependent electrical conductivity of the KBr-doped samples normalized to the electrical conductivity at 300 K show it increases as temperature increases, indicating a thermally-activated conductivity mechanism **(Fig. 4.5a)**. Disordered semiconductors containing

carbon nanotubes typically follow a 3D variable range hopping (3D VRH) conduction model, where thermal energy assists charge carriers hopping to and from conduction sites.[80,81] The 3D VRH model is $\sigma\sqrt{T} = \sigma_0 e^{\left(\frac{T_0}{T}\right)^{-\frac{1}{4}}}$, where σ is the electrical conductivity, T is the absolute temperature, σ_0 is a pre-exponential factor, and T_0 is the characteristic Mott temperature. T_0 directly correlates to the energy barrier for the hopping conduction to occur, where a lower value indicates a lower barrier for electron transport.[47,169] **Figure 4.5a** shows that T(σ) exhibits less variation with an increasing KBr concentration. The influence of temperature on electrical conductivity progressively weakens as a function of added KBr dopant. This change in T(σ) is likely due to the greater proportion of DWNT incorporated in the films, as shown in **Figure 4.3**, which is consistent with the gradual increase in carrier density as a function of KBr concentration. The T_0 values were calculated from the regression data found from a plot of ln(σ√T) vs. $K^{-0.25}$ **(Fig. 4.5c-g)**. As more KBr is added, the characteristic Mott temperature gets smaller, which is likely due to a greater amount of metallic conduction as a result of more DWNT being deposited **(Fig. 4.5b)**.[81]

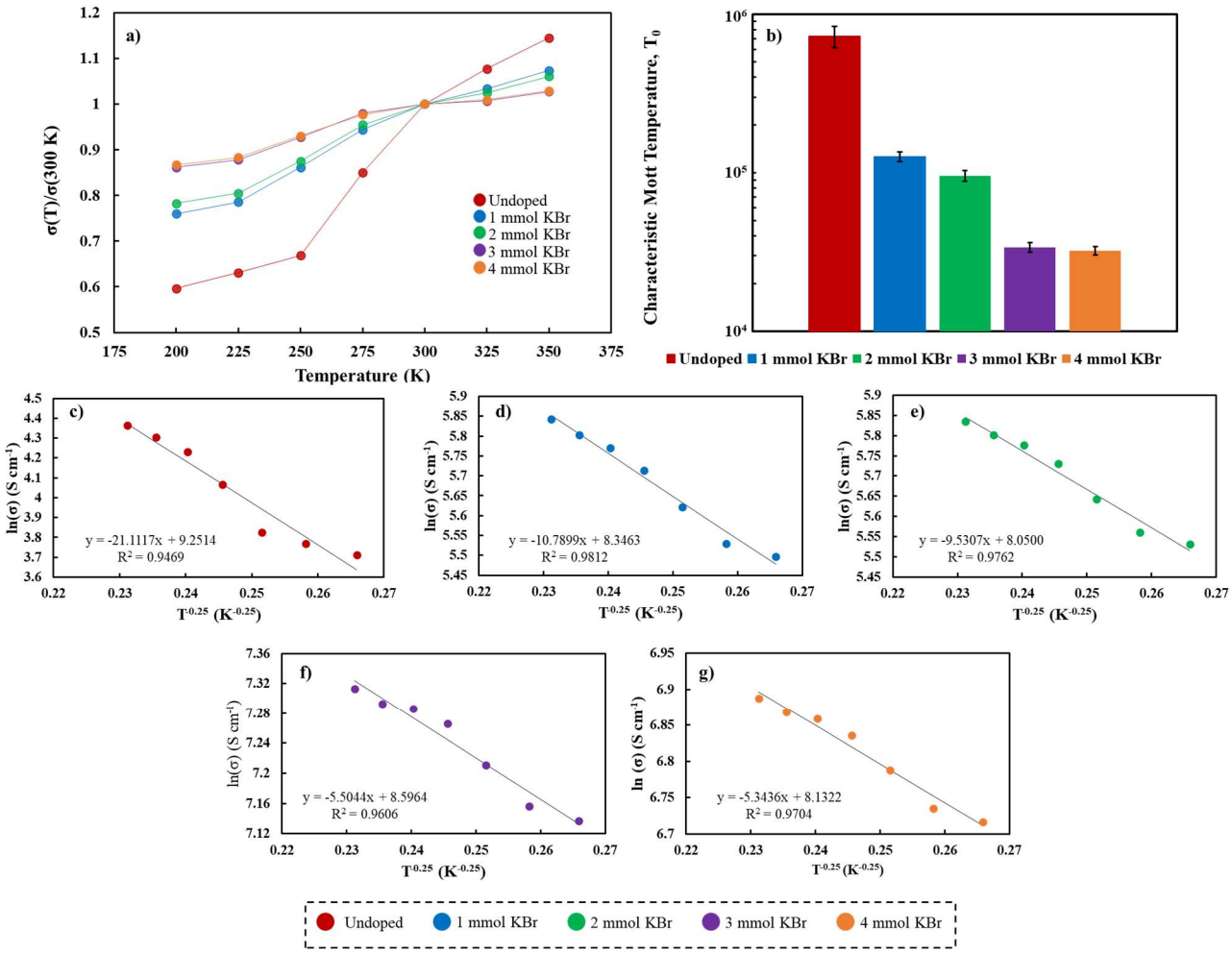

Figure 4.5. (a) Temperature-dependent electrical conductivity of 20 BL films with varying concentration of KBr. The electrical conductivity values were normalized to the room temperature (300 K) electrical conductivity. **(b)** Characteristic Mott temperature of each 20 BL film determined after applying a 3D VRH fit to the σ(T) data. Individual 3D VRH plots of 20 BL films: **(c)** undoped, **(d)** 1 mmol KBr, **(e)** 2 mml KBr, **(f)** 3 mmol KBr, and **(g)** 4 mmol KBr.

There are additional reasons why varying the proportions of PEDOT, PSS, and DWNT improve thermoelectric behavior. In addition to improving electrical conductivity, KBr addition increases carrier density due to the removal of insulating material (i.e. PSS) in the multilayer film.[168] Another contribution to improved thermoelectric performance may be due to the presence of residual Br^- as a result of PSS removal in the film that provides additional p-type doping.[106] It

is also possible that K^+ resides closer to carbon nanotubes than Na^+, which may provide more potent p-type doping (*i.e.* greater increase in carrier density) by bringing more oxygen molecules in water closer to the wall of the carbon nanotubes.[170] To investigate this notion further, films doped with 3 mmol NaBr were prepared and the TE properties were measured **(Fig. 4.7)**. The 20 BL film doped with 3 mmol KBr yields a Seebeck coefficient and an electrical conductivity of 65.1 ± 1.5 μV K^{-1} and 1479 ± 78 S cm^{-1}, while the same film doped with 3 mmol NaBr yields values of 67.2 ± 1.7 μV K^{-1} and 464 ± 14 S cm^{-1}. The larger electrical conductivity and slightly lower Seebeck coefficient for the KBr-doped film suggests a greater carrier density relative to the NaBr-doped film.

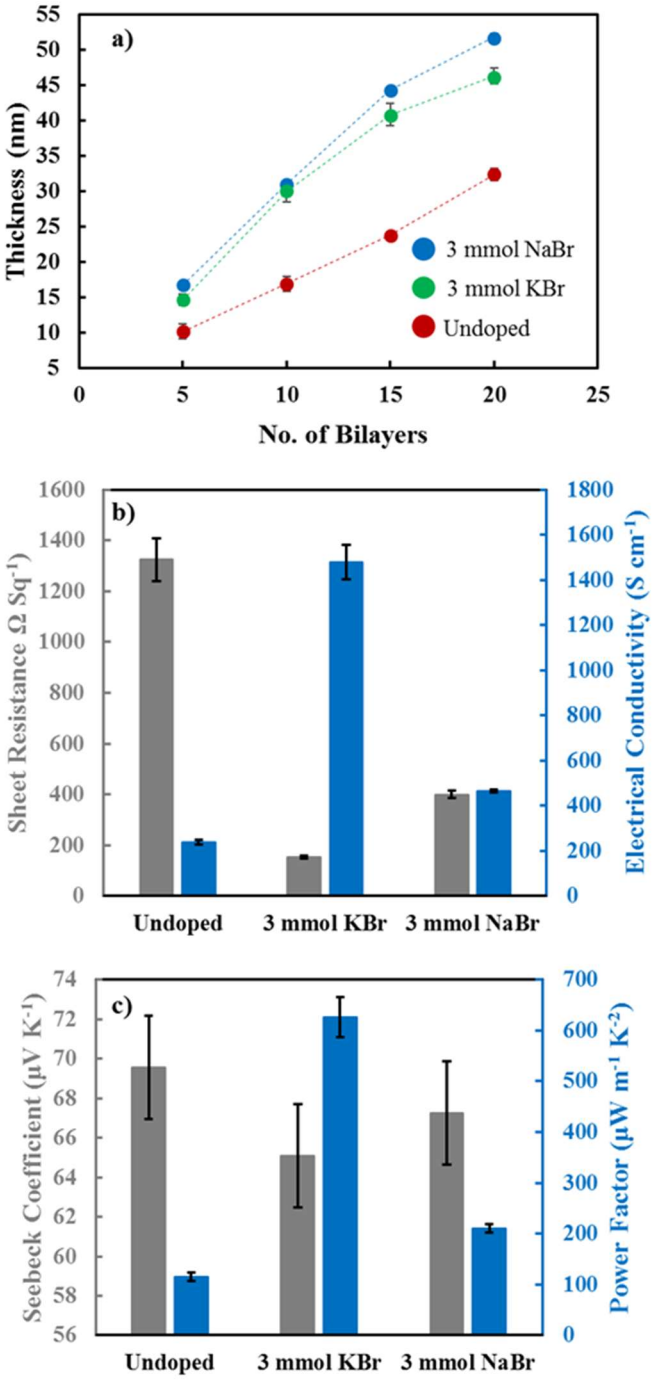

Figure 4.6. (a) Film thickness, **(b)** sheet resistance and electrical conductivity, and **(c)** Seebeck coefficient and power factor of 20 BL PDDA/PEDOT:PSS-DWNT films doped with 3 mmol KBr and 3 mmol NaBr.

The surface morphology of 20 BL films of films doped with 1, 2, or 3 mmol KBr was measured using AFM in tapping mode **(Figure 4.7a-d)**. All of these images show many carbon nanotube bundles that facilitate electron transport. As more KBr is added to these solutions, films with progressively greater surface roughness values are formed. Doping with 1 mmol KBr increases the surface roughness from 5.4 ± 0.5 to 5.8 ± 0.4 nm, relative to the undoped film. Increasing the concentration of KBr to 2 and 3 mmol results in a further increase in surface roughness to 11.2 ± 0.5 and 14.9 ± 1.1 nm, respectively. These rougher surfaces are due to larger DWNT bundles that are the result of having less PSS available to stabilize/disperse the nanotubes in solution. These bundles may contribute to increased electrical conductivity due to the decreased distance between DWNT junctions that facilitates better electron transport, which is suggested by the lower T_0 obtained from the 3D VRH model.[171]

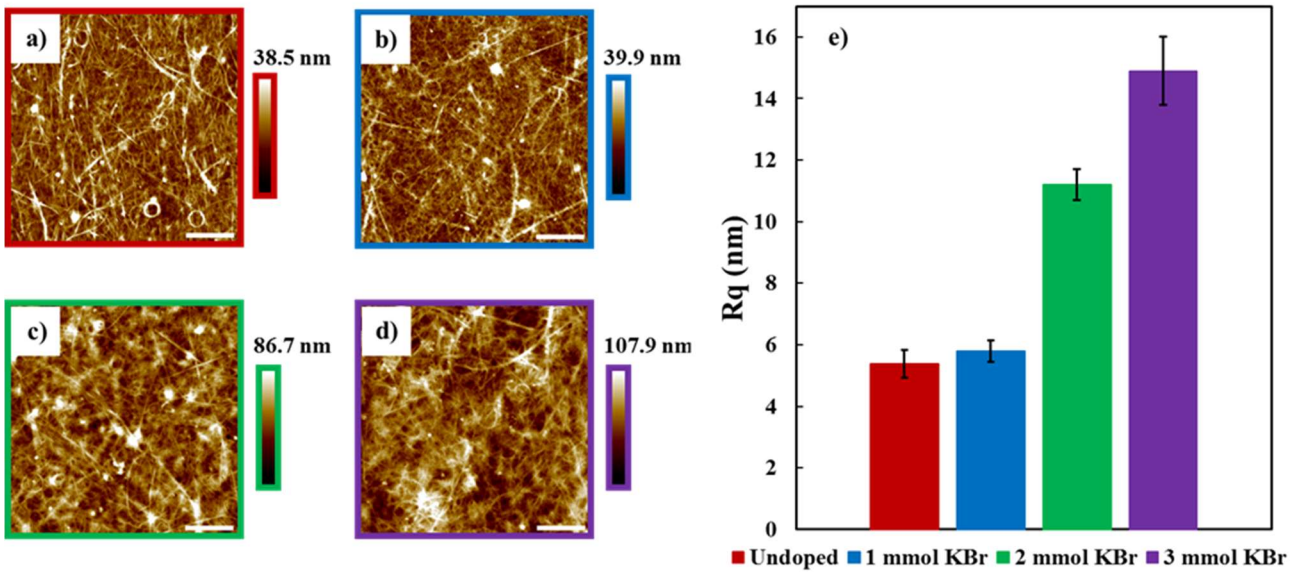

Figure 4.7. AFM surface images of 20 BL films: **(a)** undoped, **(b)** 1 mmol KBr, **(c)** 2 mmol KBr, and **(d)** 3 mmol KBr. **(e)** Rq surface roughness values of these 20 BL films. The white scale bars in these images correspond to 1 μm.

4.4 Conclusions

Doping PEDOT:PSS with KBr prior to dispersing DWNT, when depositing thin films using layer-by-layer assembly, was investigated. Thermoelectric properties were measured as a function of KBr concentration. A 20 BL PDDA/PEDOT:PSS-DWNT doped with 3 mmol KBr has an electrical conductivity of 1479 ± 78 S cm^{-1} and a Seebeck coefficient of 65.1 ± 1.5 μV K^{-1}, which translates to a power factor of 626 ± 39 μW m^{-1} K^{-2}. This is a six-fold improvement in PF relative to the undoped control due to the greater proportion of DWNT that is deposited during film deposition. DWNT content in the film coincides with a reduction in PSS, which also serves to promote greater connectivity amongst PEDOT chains. KBr weakens the strength of interaction between PEDOT and PSS, which allows for a greater amount of conductive PEDOT and DWNT to be deposited. This study demonstrates that salt can be used to tailor the amount of carbon nanotubes that are deposited during LbL assembly, resulting in a larger electrical conductivity without altering the Seebeck coefficient (*i.e.* these values are decoupled). Future work includes investigating how the size of the alkali metal in the salt dopant affects the thermoelectric properties of this system. This strategy demonstrates another tool for multilayer polymer nanocomposite preparation can be used to prepare high performance, low temperature thermoelectric materials.

CHAPTER V

THE EFFECT OF MONOVALENT SALT CATION SIZE ON THERMOELECTRIC PROPERTIES OF POLYMER NANOCOMPOSITES

5.1 Introduction

In addition to PEDOT:PSS-based materials, carbon nanotube-based materials have also exhibited improved thermoelectric properties when exposed to salt by charge transfer doping.[50,106] In one example, SWNT films exposed to $AuCl_3$ displayed a lower sheet resistance due to the adsorption of chloride ions onto the outer wall of the carbon nanotubes that extract charge from the carbon nanotubes.[106] The more charge that is extracted, the lower the sheet resistance due to the greater proportion of holes that are created from this process. Furthermore, computations suggest that the amount of extracted charge can be increased if these chloride ions are hydrated.[172] Improved electrical conductivity has been observed for LbL-assembled nanocomposites prepared from alternating depositions of PDDA and carbon nanotubes stabilized by sodium deoxycholate (DOC) that have been doped using nitric acid vapor.[50] This strategy ultimately serves to improve the electrical properties by charge transfer doping and removing the insulating DOC surfactant. Both of these factors were shown to be important in a recent study reporting the improvement in thermoelectric properties of LbL-assembled nanocomposites that were doped with KBr.[173] It was shown that adding up to 3 mmol KBr results in a greater proportion of DWNT being deposited in the film that likely results in residual doping from remaining bromide ions. In addition to studying the influence of salt concentration, the influence of other variables such as the salt identity must

be systematically investigated in order to fully elucidate the mechanisms that go into increasing thermoelectric performance.

This chapter expands on the work described in Chapter IV by investigating the influence of the salt cation on the thermoelectric performance of this salt doping strategy to a carbon nanotube-based nanocomposite. Bilayer (BL) films of PDDA/PEDOT:PSS-DWNT were prepared using LbL assembly after PEDOT:PSS was doped with 3 mmol LiCl, NaCl, KCl, or CsCl. The best thermoelectric properties were achieved by doping a 20 BL PDDA/PEDOT:PSS-DWNT with 3 mmol of CsCl (~40 nm in thickness), resulting in has an electrical conductivity of 1,123 ± 60 S cm^{-1} and a Seebeck coefficient of 65.8 ± 3.9 μV K^{-1}, yielding a power factor of 486 ± 29 μW m^{-1} K^{-2}. This power factor is approximately 4.5 times greater than the undoped control as a result of improving the electrical conductivity without decreasing the Seebeck coefficient. Doping this bilayer system with a larger cation does not appear to be due to the changes in film composition, as previously observed for the dopant concentration. Instead, the improvements from the larger cation are attributed to the downward shift in E_F as a result of a greater carrier density. This greater carrier density is likely due to the larger cations residing closer to the carbon nanotubes as a result of their increased hydrophobic solubility. This systematic investigation of the cation size further elucidates the mechanisms that factor into the improved thermoelectric properties.

5.2 Experimental

5.2.1 Materials

LiCl, NaCl, KCl, and CsCl were purchased from Millipore-Sigma (> 99 % purity, Milwaukee, WI). Poly (diallyldimethylammonium chloride) (PDDA) (M_w = 200,000 – 350,000 g/mol, 20 wt % aqueous solution) was also purchased from Millipore Sigma. Poly (3,4, -

ethylenedioxythiophene): poly (styrene sulfonate) (PEDOT:PSS) was purchased from Heraeus Precious Metals (Clevios PH 1000, Hanau, Germany) and double-walled carbon nanotubes (DWNT) were purchased from Continental Carbon Nanotechnologies Inc. (XB type, 1 μm length, 2 nm diameter, Houston, TX). All salts were heated at 120 °C overnight to remove any residual water, while PDDA, PEDOT:PSS, and DWNT were used as received. Each solution used in this study was prepared using 18 MΩ deionized (DI) water. Silicon wafers (p-type, 1 0 0, University Wafer, Boston, MA) and 179 μm poly (ethylene terephthalate) (PET) (ST505, Tekra Crop., New Berlin, WI) were the substrates used in this study.

5.2.2 Preparation of Salt-Doped PEDOT:PSS-DWNT Solutions

Salt-doped PEDOT:PSS-DWNT solutions were prepared according to previous reports.[73,173] Briefly, 3 mmol of LiCl, NaCl, KCl, or CsCl was added to 5 g of PEDOT:PSS, which was stirred vigorously overnight. Then, 0.05 g of DWNT was suspended in the salt-doped PEDOT:PSS solution using a mortar and pestle. After exfoliating the DWNT, DI water was added to dilute the concentration of PEDOT:PSS and DWNT to 0.06 wt% and 0.05 wt%, respectively. These PEDOT:PSS-DWNT solutions were bath sonicated followed by tip sonication (15 W) for 30 minutes each. These sonication steps were repeated to ensure the solutions were completely homogenized. After sonication, the solutions were centrifuged for 20 minutes at 4,000 rpm. The supernatant was separated from the gelatinous precipitate using a pipet, and the decanted solution was used for film deposition. The undoped control did not contain any additional salt.

5.2.3 Layer-by-Layer Assembly

All substrates were cleaned using a series of DI water, methanol, DI water, and dried with compressed air. Silicon wafers were subsequently cleaned in a plasma chamber (Atto Plasma System, Thierry Corporation, Royal Oak, MI) for 5 minutes. Clean PET substrates were subjected to corona treatment (BD-20C, Electro Technic Products Inc., Chicago, IL) for the same rationale as the plasma treatment. A home-built automated film preparation system was used for LbL film deposition.[148] The cleaned substrate was initially immersed in a 0.25 wt % PDDA solution for five minutes, followed by spray rinsing with DI water and drying with compressed air. This initial deposition procedure was followed exactly for the salt-doped PEDOT:PSS-DWNT solution. The completion of this sequence is referred to as one bilayer (BL). For subsequent cycles, all deposition times were reduced to one minute and the pH of both solutions were unchanged.

5.2.4 Film Characterization

The film thickness of samples deposited on Si wafers was measured using an α-SE ellipsometer (J.A. Woolam Co. Lincoln, NE), with a 632.8 nm laser held at 70 °. Raman spectra of 20 BL films deposited on Si wafers were collected using a Jobin-Yvon Horiba Labram HR instrument (Piscataway, NJ) connected to an Olympus BX41 optical microscope (Waltham, MA), with a 514.5 Ar-ion laser used as the excitation source. X-ray photoelectron spectroscopy (XPS) was conducted on 20 BL films deposited on Si wafers with an Omicron XPS/UPS system (Denver, CO), using a monochromatic DAR Mg X-ray source (1253.6 eV), with an energy resolution of 0.8 eV. Reported XPS peaks were calibrated to the Au $4f_{7/2}$ peak at 84.0 eV. The resulting XPS spectra were analyzed using Casa (version 2.3.22) software. Topographical images of 20 BL films deposited on Si wafers were measured over a 5 x 5 μm scan area using a Dimension Icon atomic

force microscope (AFM) (Bruker, Billerica, MA). AFM probes (HQ:NSC35/Al BS, Micromasch USA Watsonville, CA) had a force constant of 5.5 – 16 N/m and a tip radius of approximately 8 nm. Reported surface roughness (R_q) values were the average of three separate images, processed with the Bruker 1.9 Nanoscope software.

5.2.5 Thermoelectric Measurements

The sheet resistance of 8 x 12 mm 20 BL films deposited on PET were measured using a Signatone Pro four-point probe (Gilroy, CA) connected to a E3644A DC power supply and a 2400 Keithley multimeter (Cleveland, OH), using a SCB-68 I/O connector block (National Instruments, Austin, TX). The operating voltage for the multimeter was 10 V. The probe tips were 0.4 mm in diameter with a 1.0 mm separation between them. The sheet resistance (Rs) was calculated using $R_s = 4.23$ (V/I), where 4.23 us the correction factor based on the dimensions of the substrate relative to the spacing between the probes.[48] The electrical conductivity (S cm^{-1}) was found by taking the inverse of the product of the sheet resistance (Ω Sq^{-1}) and the thickness (cm) of the film. Temperature-dependent resistivity measurements were acquired using a Dynacool Physical Property Measurement System (Quantum Design, San Diego, CA), using a current of 2 mA. The Seebeck coefficient was gathered with a home-built setup that measured the in-plane thermoelectric voltage across eight distinct temperature differentials between 0 and 10 K.[28,29] Reported Seebeck coefficients were calculated from the slope of the linear fit to the voltage vs. temperature gradient plot with its y-intercept fixed at 0 V. The correlation coefficient of each slope was at least 0.99.

5.3 Results and Discussion

5.3.1 Film Growth and Characterization

A schematic outlining the PEDOT:PSS(salt) – DWNT suspension and the schematic for layer-by-layer (LbL) deposition is shown in **Figure 5.1a**. PEDOT:PSS has been previously utilized as a polymeric, conductive surfactant for DWNT in water.[29,168] The chemical structures of the components used in this study are shown in **Figure 5.1b**. Salts mitigate the intermolecular forces between PEDOT and PSS, which creates a longer electron conduction pathway of PEDOT chains by separating these two polymers.[92] Film thickness as a function of bilayers for the salt-doped samples is shown in **Figure 5.1c**. Doping PEDOT:PSS with salt results in a thicker film due to charge screening of the charged repeat units of PSS, due to the creation of more extrinsic charge compensation (*i.e.* polymer-ion pairings) in the multilayer assembly.[21,27] Additional salt lowers the charge density of polyelectrolytes, which requires more material to be deposited to overcompensate the surface charge contributed by the previous deposition step.[22,150] The amount of extrinsic compensation can be increased by increasing the salt concentration and salt identity. This doping efficiency typically follows the Hofmeister series,[174] and is a function of how these ions perturb the surrounding water structure. Larger and more hydrophobic ions generally disrupt the surrounding water structure to a greater degree, which increases the doping efficiency of these salts (*i.e.* it requires less salt to achieve a certain level of extrinsic compensation) that usually results in a more potent thickening effect.[21,22,174] However, these films show a decrease in film thickness when salts with larger cations are employed, which is counterintuitive to pervious reports.

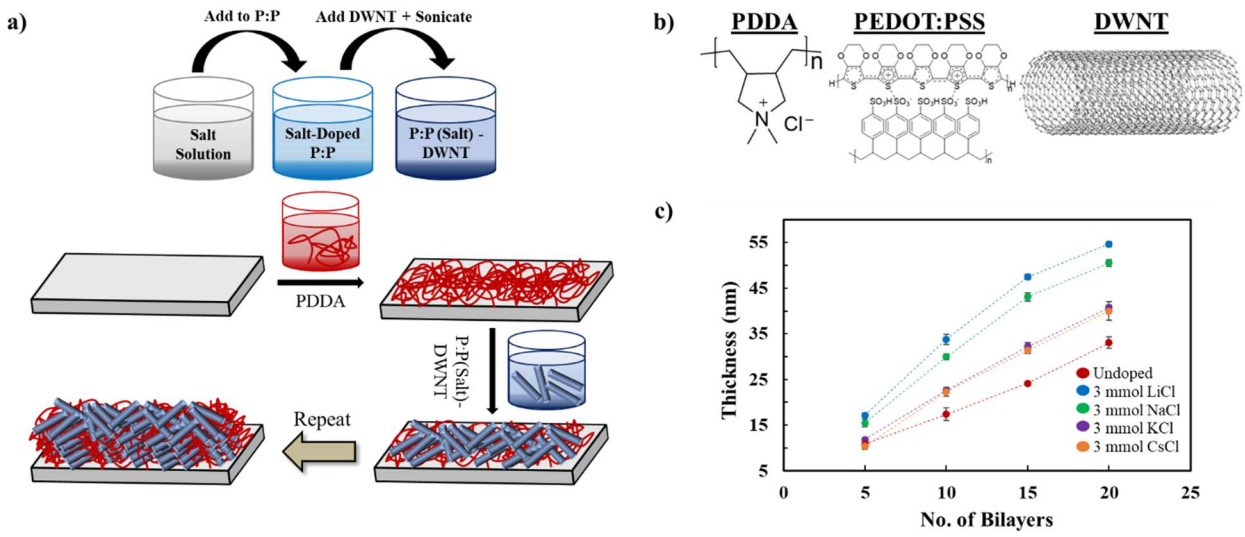

Figure 5.1. (a) Schematics of nanoparticle suspensions and layer-by-layer deposition used in this study, and **(b)** chemical structures of the film components. **(c)** Film thickness of PDDA/PEDOT:PSS (salt) – DWNT films as a function of bilayers deposited and varying cation size.

A previous investigation of how the KBr concentration affects the thermoelectric performance of PDDA/PEDOT:PSS-DWNT films revealed that the performance was due to the greater ratio of conductive components (*i.e.* PEDOT and DWNT) deposited.[168] To investigate the relative amounts of PEDOT, PSS, and DWNT in the film as a function of salt identity, XPS S 2p spectra were collected to examine the relative amount of PEDOT and PSS, while Raman spectra were used to compare the relative amount of PEDOT and DWNT in the film. PEDOT:PSS exhibits two large peaks in the S 2p region that correspond to PSS (~ 168 eV) and PEDOT (~164 eV) due to the different binding environments of sulfur in these two polymers.[154–156] **Figure 5.2a-b** indicate that doping PEDOT:PSS with salt increases the relative ratio of PEDOT to PSS in the multilayer film, which suggests that PSS is removed from an ion exchange reaction with the salt that is likely separated during the final decanting step of the PEDOT:PSS(salt) – DWNT preparation procedure. The influence of the size of the salt cation is insignificant on the ratio of PEDOT to PSS in the multilayer film. Additionally, C 1s spectra of these salt-doped films reveal a progressive downward

shift in the binding energy, where the maximum intensity occurs as salts with larger cations are employed **(Figure 5.2c-d)**. This observation for carbon nanotube-based thermoelectrics corresponds to the E_F shifting towards the valance band, which suggests that a greater dopant concentration is found in samples doped with a larger cation.[109,175] Raman spectra of 20 BL PDDA/PEDOT:PSS(salt)-DWNT films were used to compare the relative amounts of PEDOT to DWNT. These spectra are normalized to the G Band (~ 1590 cm^{-1}) of DWNT, which corresponds to the sp^2 hybridization of the carbon nanotubes.[151] At a dopant concentration of 3 mmol, the changes in the DWNT to PEDOT ratio in the multilayer film do not reveal a correlation with the size of the salt cation **(Figure 5.3)**.

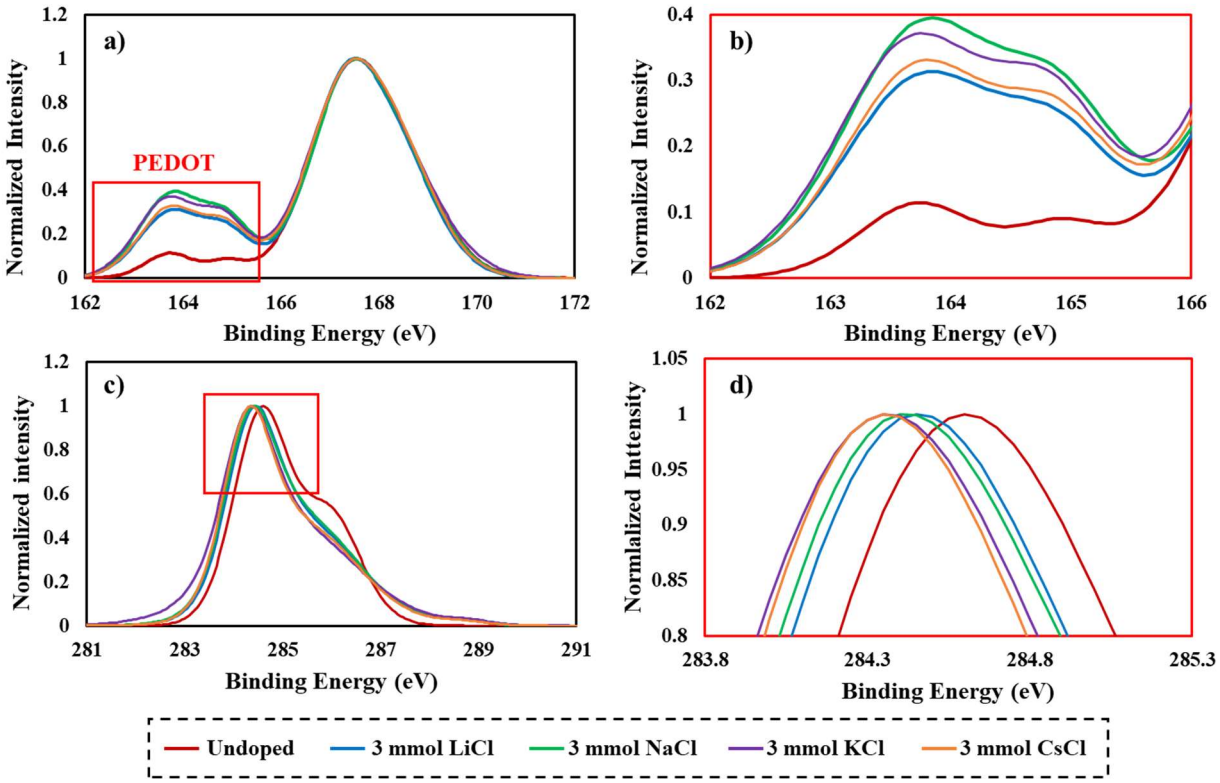

Figure 5.2. (a) XPS S 2p spectra of a 20 BL PDDA/PEDOT:PSS (salt) – DWNT film normalized to the PSS peak, and **(b)** the same spectra focused on the region corresponding to the sulfur in PEDOT. **(c)** XPS C 1s spectra of a 20 BL PDDA/PEDOT:PSS (salt) – DWNT film normalized to the maximum intensity, and (d) the same spectra focused on these maxima.

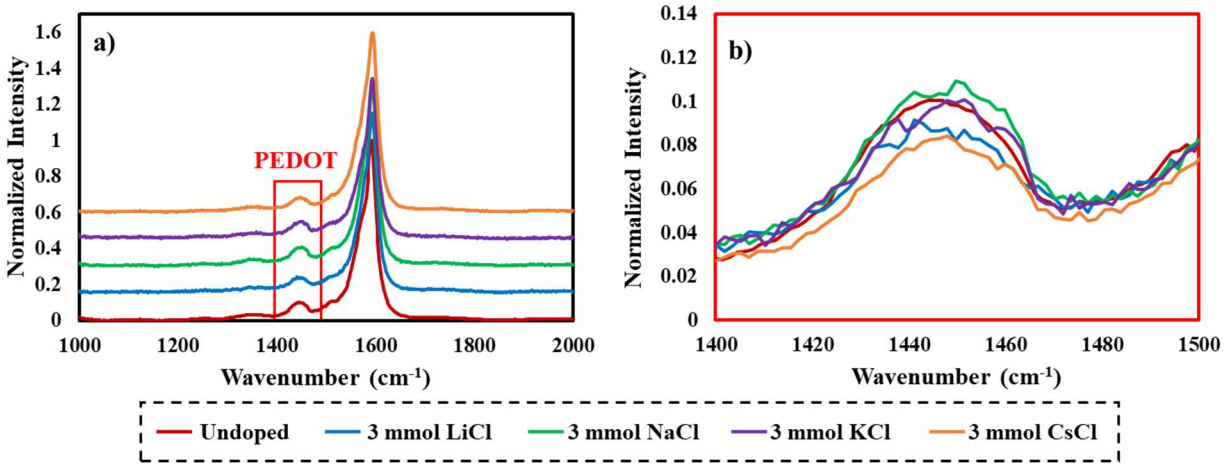

Figure 5.3. (a) Raman spectra of a 20 BL PDDA/PEDOT:PSS (salt) – DWNT film normalized to the G-band of DWNT (~1590 cm-1), and **(b)** the same Raman spectra focused on the C=C symmetric stretch of PEDOT.

5.3.2 Thermoelectric Behavior

Sheet resistance and electrical conductivity of 20 BL PDDA/PEDOT:PSS(salt)-DWNT films measured are shown in **Figure 5.4a**. The electrical conductivity steadily increases when salts containing larger cations are used as dopants. A 20 BL film doped with 3 mmol LiCl increases to 472 ± 34 S cm^{-1}, from the 238.3 ± 9.7 S cm^{-1} exhibited by the undoped sample. Doping with NaCl yields a similar electrical conductivity value (419 ± 23 S cm^{-1}) as compared to using LiCl. Further increasing the cation size by using KCl and CsCl result in larger electrical conductivity values of 937 ± 32 S cm^{-1} and 1,123 ± 60 S cm^{-1}, respectfully. The gradual improvement in electrical conductivity is likely due to the lowering of the E_F toward the conduction band as the result of more hole carriers in the film, which is consistent with the binding energy of the maximum peak in the XPS C 1s spectra shifting to a lower value.

Figure 5.4b shows the Seebeck coefficient and power factor of 20 BL PDDA/PEDOT:PSS – DWNT films. Doping these films with salts containing progressively larger cations results in very similar Seebeck coefficients relative to the undoped sample, which suggests that this doping

strategy results in the decoupling of conductivity and the Seebeck coefficient Previous reports show increasing Seebeck coefficients are accompanied by an increase in the carrier mobility.[29] Specifically, for PEDOT:PSS-based thermoelectrics, removing the insulating polymer allows for greater π-π stacking between PEDOT chains that serve to increase carrier mobility. Recently, an LbL-assembled nanocomposite prepared using PDDA and PEDOT:PSS was shown to exhibit a simultaneous increase in the electrical conductivity and the Seebeck coefficient after removing insulating material through post-deposition thermal treatments exceeding 375 °C. The carrier density in this film increases by a factor of seven when the insulating material is expelled from the film. This observation traditionally corresponds to a lower Seebeck coefficient,[3,43] but these films exhibit a greater asymmetric density of states near E_F after the insulating material which removed, which is the likely reason for the improvement in Seebeck coefficient. Utilizing salts with larger cations adds a more potent doping effect according to XPS C 1s measurements, which is most likely due to the increase in carrier density.

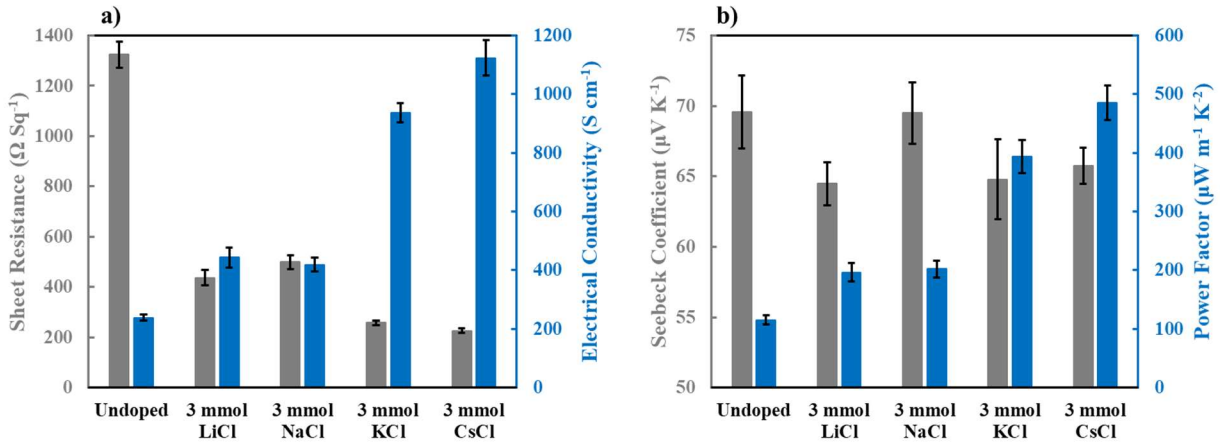

Figure 5.4. (a) Sheet resistance and electrical conductivity of 20 BL PDDA/PEDOT:PSS (salt) – DWNT films as a function of cation size. **(b)** Seebeck coefficient and power factor of 20 BL PDDA/PEDOT:PSS (salt) – DWNT films as a function of cation size. These measurements were conducted under ambient conditions.

The power factor in **Figure 5.4b** progressively increases for salts containing larger cations due to the increase in electrical conductivity. The maximum power factor of 485 ± 29 μW m^{-1} K^{-2} was achieved when using 3 mmol CsCl to dope PEDOT:PSS prior to depositing a 20 BL film. This power factor is a factor of 4.5 larger than the power factor of the undoped control. In a previous report that investigated similar films as a function of added KBr concentration, the improvement in the electrical conductivity was due to the greater proportion of DWNT that was deposited during deposition.[173] As the thermoelectric power factor progressively improves for larger cation dopants, insignificant changes in the composition of PEDOT, PSS, and DWNT were observed with XPS and Raman spectroscopy. Normalized temperature-dependent conductivity measurements of the undoped and salt-doped samples are shown in **Figure 5.5a.** Conductivity increases to a lesser relative degree when doped with salts containing larger cations. This observation suggests a heavier doping effect with larger cations, which is consistent with XPS C 1s measurements. Noncrystalline semiconductors typically follow a 3D Variable Range Hopping (3D VRH) mechanism, which describes a particular energy barrier in the system that must be overcome to allow for a charge carrier to move to the next conduction site in the material.[80,81] The magnitude of the energy barrier is incorporated into the Characteristic Mott Temperature (T_0) term. However, conducting 3-D variable range hopping analysis on these samples indicates that the increase in electrical conductivity is not simply due to a decrease in the height of the energy barrier by 3D VRH modeling **(Fig. 5.5b)**.

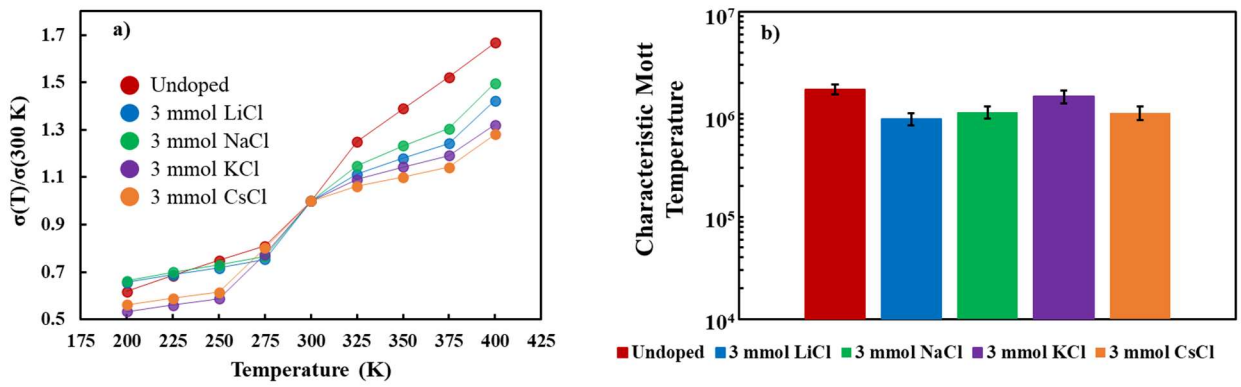

Figure 5.5. (a) Temperature-dependent electrical conductivity of 20 BL PDDA/PEDOT:PSS (salt) – DWNT films doped with salts of varying cation size. The electrical conductivity values were normalized to the room temperature (300 K) electrical conductivity. **(b)** The Characteristic Mott temperature of each 20 BL film was determined after fitting the data to a 3D VRH model.

5.3.3 Mechanism for Improved Thermoelectric Performance

Polymer nanocomposites prepared by LbL assembly that are doped with KBr exhibit improved thermoelectric performance due to the greater deposition of metallically conducting carbon nanotubes.[173] Despite this result, a significant increase in DWNT incorporation is not observed when the salt cation is varied, suggesting an alternative mechanism for observed improvements. As mentioned previously, adding salt to the deposition solutions in the preparation of polyelectrolyte multilayers serves to screen the charged repeat units on the polymers through extrinsic compensation, lowering their charge density. As a result, more polymer needs to be deposited to overcompensate the surface charge established by the previous deposition step. The type of salt also plays a significant role in the extent of intrinsic compensation in polyelectrolyte multilayer buildup. The "doping efficiency" (*i.e.* lower salt concentration needed to achieve greater extents of extrinsic compensation) closely follow the Hofmeister series, where ions that exhibit greater perturbations in the surrounding water structure are more efficient "dopants".

Another way of investigating this problem is by investigating the softness parameter of the individual cations, which is related to its ionization energy in the solvation medium.[176] **Table 5.1** compares these reported softness parameters and oxygen coordination numbers of the cations solvated in water that are investigated in this work.[177] These data suggest that the larger cations are softer and have a greater number of water molecules coordinated to them. In addition, recent studies examining the interaction between Na^+ or K^+ and the π-interaction of a carbon nanotube in a water environment. This work demonstrates that K^+ resides closer to carbon nanotubes than Na^+, which suggests that that the greater hydrophobicity of the larger cations may sit closer to carbon nanotubes than smaller cations.[170,176] When considering the larger oxygen coordination numbers and hydrophobic solubility of the larger cations, they likely bring forth a greater negative partial charge from the coordinated water molecules. A plausible result of this observation would be a greater increase in the carrier density from the greater p-type doping effect imparted by the water molecules. Previously reported computational work comparing the binding energies of alkali metal-benzene complexes to alkali metals as a function of associated water molecules suggests that larger alkali metals like K^+ prefer to associate with benzene as more water molecules are introduced.[170] The difference in binding energy would be due to the larger alkali metals (K^+ and Cs^+) imparting a greater doping effect as a result of their greater hydrophobic solubility than smaller ones (Li^+ and Na^+).

Table 5.1. Summary of computed oxygen coordination numbers of various cations in water.[177] Adapted with permission from Yu, H.; Whitfield, T. W.; Harder, E.; Lamoureux, G.; Vorobyov, I.; Anisimov, V. M.; MacKerell, A. D.; Roux, B. Simulating Monovalent and Divalent Ions in Aqueous Solution Using a Drude Polarizable Force Field. *J. Chem. Theory Comput.* **2010**, *6* (3), 774 – 786.

Cation	N_{CO}
Li^+	4.0
Na^+	5.6
K^+	6.9
Cs^+	9.7

Topographical imaging was used to investigate how the surface morphology changes when salt containing larger cations are used as dopants **(Fig. 5.6)**. Previous work on thermoelectric carbon nanotube-based composites suggest that a slight increase in carbon nanotube bundling is advantageous for the electrical conductivity due to the decreased space between the nanotubes, which is reflected as a modest increase in the surface roughness.[171] Doping a 20 BL film with 3 mmol LiCl and 3 mmol NaCl have Rq surface roughness values of 7.07 ± 0.40 nm and 7.59 ± 0.29, respectively. These are both larger than the surface roughness of the 20 BL undoped control, which is 5.38 ± 0.46 nm. Using salts with more hydrophobic alkali metal cations such as KCl and CsCl show drastically larger surface roughness values of 11.2 ± 2.2 nm and 12.4 ± 2.4, respectively. The increased surface roughness for salt-doped films is in part due to having less PSS present in the deposition solution to exfoliate DWNT. The progressively increasing surface roughness is likely due to the increasing softness and hydrophobicity of the larger cations, which directly correlates to the increasing electrical conductivity. These observations in tandem suggest that salts

with more hydrophobic ions may be more effective at promoting DWNT bundling, which has been correlated previously with greater electron transport.

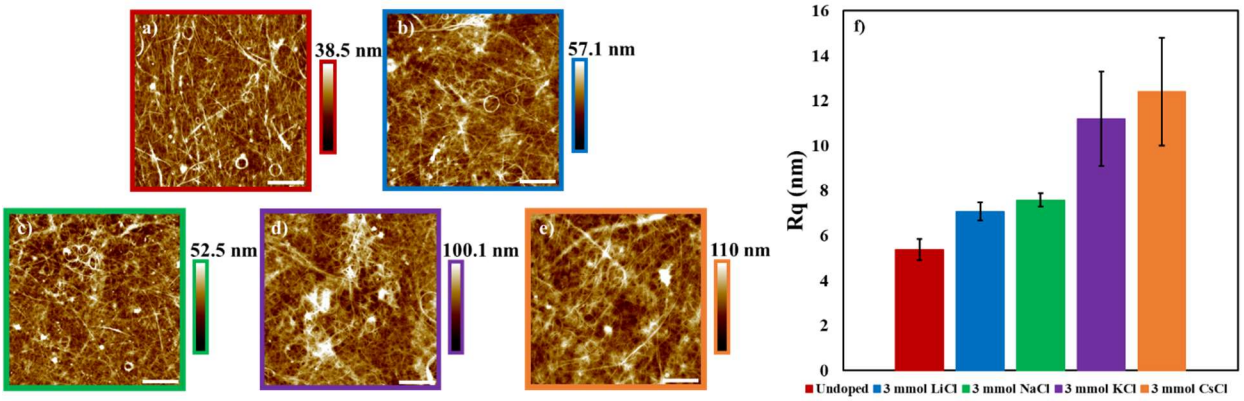

Figure 5.6. AFM surfaces images (5 µm x 5 µm in size) of 20 BL films: **(a)** undoped, **(b)** 3 mmol LiCl, **(c)** 3 mmol NaCl, **(d)** 3 mmol KCl, and **(e)** 3 mmol CsCl doped. **(f)** Rq surface roughness values of these 20 BL films. The white scale bars in these images correspond to 1 µm.

5.4 Conclusions

The influence of the salt cation size was systematically investigated as a dopant for LbL-assembled films to elucidate the mechanism of thermoelectric improvement. The electrical conductivity and Seebeck coefficient were examined as a function of cation size. A 20 BL PDDA/PEDOT:PSS – DWNT film doped with 3 mmol CsCl has an electrical conductivity of 1,123 ± 60 S cm^{-1}, and a Seebeck coefficient of 65.8 ± 3.8 µV K^{-1}, which results in a power factor of 485 ± 29 µW m^{-1} K^{-2}. This improvement in the power factor was realized by improving the electrical conductivity without depreciating the Seebeck coefficient, which suggests that these values are decoupled and attributed to the greater electrical conductivity as a heavier doping effect by the salts with larger cations. As a result, E_F shifts closer to the valence band and the larger relative hydrophobicity of K^+ and Cs^+ result in the observed heavier doping effects. These results

suggest that the overall doping effect is influenced by the energetic balance between the hydrophobic interaction between the salt ions and the carbon nanotubes. This study provides experimental evidence of the importance of balancing hydrophobic interactions in the preparation of multilayer polymer nanocomposites. These types of materials can be used to prepare high performing thermoelectric devices that operate at low temperatures.

CHAPTER VI

CONCLUSIONS AND OUTLOOK

6.1 Thermoelectric Multilayer Polymer Nanocomposites

Novel thermal treatment and salt doping strategies for LbL-assembled thin films were studied in an effort to improve the thermoelectric performance of these polymer nanocomposites. Both of these strategies rely on decreasing the amount of insulating material incorporated into the films through facile post- and pre-deposition methods. In addition to increasing thermoelectric performance, fundamental and systematic investigations into the thermal treatment and salt doping strategies uncover how the relative degradation and solubility characteristics of the salts affect the attractive interactions utilized to buildup these multilayer assemblies.

In Chapter III, a post-deposition thermal treatment that removes insulating polymer that is necessary to fix the morphology of a graphene-DWNT network was described. This study demonstrated that the degradation of the insulating complex rather than the individual polyelectrolytes was the main factor for improved thermoelectric performance. In Chapter IV, doping PEDOT:PSS with varying concentrations of KBr was shown to not only improve the thermoelectric properties, but also provide a simple way to tune the ratio of the PEDOT, PSS, and DWNT that are incorporated into the multilayer film. This strategy improves the thermoelectric performance by increasing the electrical conductivity without lowering the Seebeck coefficient. In Chapter V, the influence of the size of the alkali metal in the doping salt was described. While the cation size did not yield a strong correlation in terms of film composition, larger and more hydrophobic cations result in better thermoelectric performance and a heavier doping effect. Systematically investigating the salt concentration and identity reveals a delicate balance of

hydrophilic and hydrophobic interactions that alters the proportion of the different exfoliated ingredients that are deposited.

6.2 Future Directions for Thermoelectric Polymer Nanocomposites

6.2.1 Air-Stable N-type Carbon Filler Stabilizers

Improving the thermoelectric performance of n-type organic composites is important for generating the maximum voltage from a thermoelectric device. As described in Chapter II, air-stable n-type transport is challenging due to the demanding requirements of a high HOMO energy level and electron affinity for the dopant. Cho et al. reported two LbL-assembled air-stable n-type polymer nanocomposites that exhibit power factors of 190 and 400 μW m^{-1} K^{-2},[24,140] but these strategies require a larger amount of insulating material to provide this air stability. In order to provide less insulating material, while delivering improved n-type transport, incorporating a rylene diimide molecule as an aqueous stabilizer for DWNT may result in improved thermoelectric performance. Spin-coated films of a perylene diimide yield Seebeck coefficients in excess of 100 μV K^{-1},[178] while CNT composites prepared with a rylene diimide (RD) give a larger Seebeck coefficient than ones prepared with polyethylenimine (PEI) **(Fig. 6.1)**.[179] Its higher Seebeck coefficient, thermal stability, water solubility, and air stability make RD a more promising candidate than PEI for thermoelectric applications.

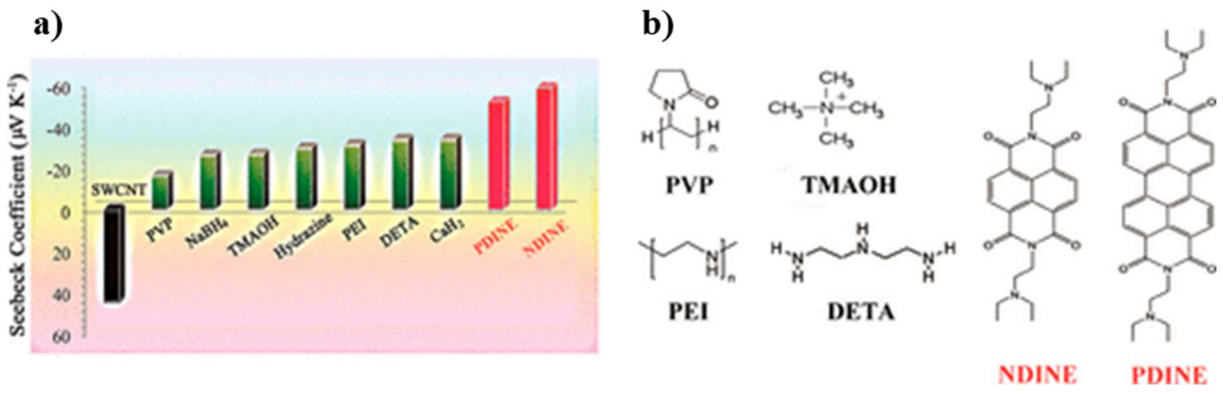

Figure 6.1. (a) Seebeck coefficients of common n-type dopants and surfactants for carbon nanotube composites. **(b)** Chemical structures of the n-type surfactants with the rylene diimide (NDINE and PDINE) surfactants.[179] Adapted with permission from Wu, G.; Zhang, Z-G.; Li, Y. Gao, C.; Wang, X, Chen, G. Exploring High-Performance n-Type Thermoelectric Composites Using Amino-Substituted Rylene Diimides and Carbon Nanotubes. *ACS Nano* **2017**, *11* (6), 5746 – 5752.

6.2.2 Additive Effect of Thermal Treatment and Salt Doping Strategies

Thermal treating of these nanocomposites increases the number of high energy charge carriers near the Fermi level, while KBr doping causes a greater amount of conductive materials to be deposited. Since these mechanisms do not seem interdependent on one another, the additive effect of combining these strategies for 20 QL films doped with 3 mmol KBr was investigated. The PEDOT:PSS(KBr) – graphene and PEDOT:PSS(KBr) – DWNT solutions were prepared similarly to the solutions described in Chapter IV, and the films were deposited identically to the ones prepared in Chapter III. Since the optimal thermoelectric performance was observed at 375 and 425 °C, these were the only temperatures investigated.

Doping with KBr in either the PEDOT:PSS – graphene or PEDOT:PSS – DWNT results in a greater film thickness due to a lower charge density on charged repeat units from charge screening effects,[27,173] as shown in **Figure 6.2a**. Salt-doped films also have higher refractive indices **(Fig. 6.2b)** that suggest a greater film density. Density has been previously correlated with

improved thermoelectric properties.[173] Lastly, quadlayers prepared from KBr-doped PEDOT:PSS – graphene and PEDOT:PSS – DWNT solutions result in the greatest relative change in thickness, which suggests that more PDDA is deposited **(Fig. 6.2c)**. Considering that this sample grows the thickest and has a similar refractive index to the other quadlayer samples, it also suggests that more graphene and DWNT are deposited in the film when KBr is added.

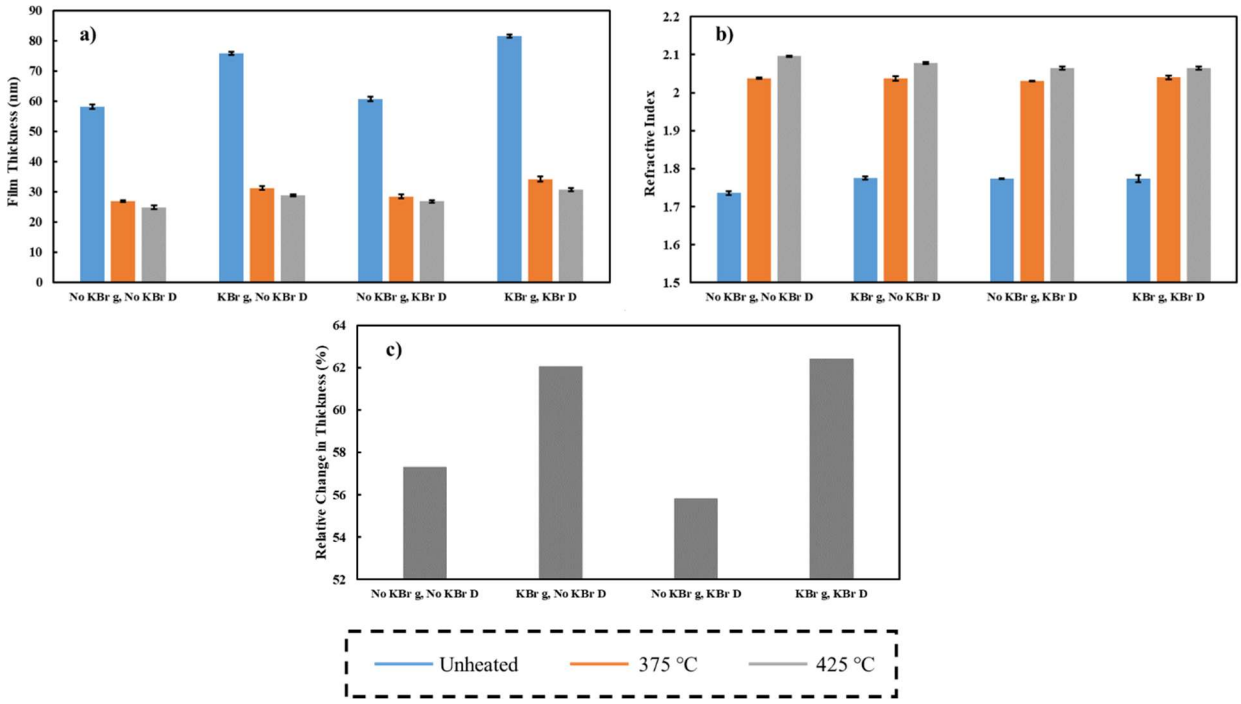

Figure 6.2. (a) Film thickness and **(b)** refractive index of 20 QL PDDA/ PEDOT:PSS – graphene/ PDDA/ PEDOT:PSS – DWNT films as a function of thermal treatment temperature and KBr doping. **(c)** Relative change in thickness after subjecting these 20 QL films to a 60 minute thermal treatment at 425 °C.

Depositing more graphene and DWNT in each deposition cycle correlates with improved thermoelectric performance **(Fig. 6.3)**. As observed in Chapter III, unheated films exhibit low Seebeck coefficients and electrical conductivities. Of the unheated samples, the maximum power factor of 36.8 ± 4.4 μW m^{-1} K^{-2} was achieved for the film deposited from KBr-doped PEDOT:PSS

– graphene and PEDOT:PSS – DWNT solutions. This film continues to have the greatest power factor after 60 minutes thermal treatments at 375 and 425 °C, yielding power factors of 114 ± 9 μW m^{-1} K^{-2} and 330 ± 30 μW m^{-1} K^{-2}, respectively. This increased thermoelectric performance suggests that these strategies can be used in tandem to improve the thermoelectric performance of quadlayer films. It should be noted that while these films exhibit power factors lower than LbL films prepared with polyaniline as the polycation, these films are simpler and faster to prepare. Greater thermoelectric performance can likely be achieved with deposition cycles.

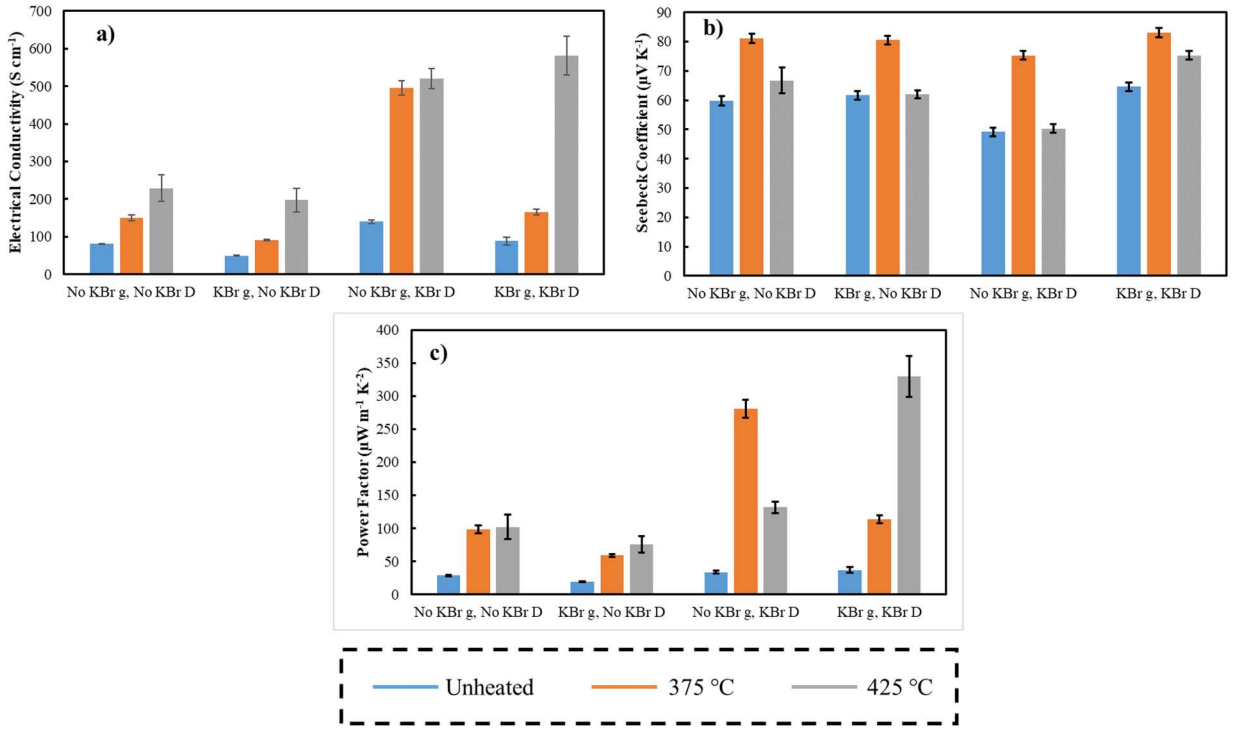

Figure 6.3. (a) Electrical conductivity, **(b)** Seebeck coefficient, and **(c)** power factor of 20 QL PDDA/ PEDOT:PSS – graphene/ PDDA/ PEDOT:PSS – DWNT films. These films reveal the additive benefit of KBr doping and a post-deposition thermal treatment.

6.2.3 Salt Doping of Multilayer Thin Films Using Polyaniline as the Polycation

For the studies described in Chapters IV and V, PDDA was used as a model polycation as a model system to study the influence of salt concentration and cation size. The largest thermoelectric power factor for a polymer nanocomposite prepared by LbL assembly was achieved using PANi as the polycation.[29] Incorporating salt doping into the preparation of this film would likely further improve the thermoelectric performance by depositing a greater relative amount of conductive materials. While different salts of varying concentration would likely be required to fully optimize this system, KBr is a good first candidate based on the work described in this dissertation. This system contains different concentrations of PEDOT:PSS and DWNT than the systems described in Chapters IV and V, so an optimal concentration would need to be determined. If this film yields a larger power factor than the undoped film, or the same properties with fewer deposition cycles, this will be a large step forward toward implementation of polymer nanocomposites into commercial devices.

REFERENCES

(1) Singer, L. E.; Peterson, D. *International Energy Outlook 2016*; 2011; Vol. 0484.

(2) Administration, U. S. E. I. Annual Energy Outlook https://www.eia.gov/outlooks/aeo/ (accessed May 12, 2020).

(3) Blackburn, J. L.; Ferguson, A. J.; Cho, C.; Grunlan, J. C. Carbon-Nanotube-Based Thermoelectric Materials and Devices. *Adv. Mater.* **2018**, *30* (11), 1704386. https://doi.org/10.1002/adma.201704386.

(4) Little, A. B.; Garimella, S. Comparative Assessment of Alternative Cycles for Waste Heat Recovery and Upgrade. *Energy* **2011**, *36* (7), 4492–4504. https://doi.org/10.1016/j.energy.2011.03.069.

(5) United States Department of Energy. Transparent Cost Database. OpenEI. *Natl. Renew. Energy Lab.* **2017**, 1–10.

(6) Forman, C.; Muritala, I. K.; Pardemann, R.; Meyer, B. Estimating the Global Waste Heat Potential. *Renew. Sustain. Energy Rev.* **2016**, *57*, 1568–1579. https://doi.org/10.1016/j.rser.2015.12.192.

(7) Russ, B.; Glaudell, A.; Urban, J. J.; Chabinyc, M. L.; Segalman, R. A. Organic Thermoelectric Materials for Energy Harvesting and Temperature Control. *Nat. Rev. Mater.* **2016**, *1*, 16050. https://doi.org/10.1038/natrevmats.2016.50.

(8) Dresselhaus, M. S.; Chen, G.; Tang, M. Y.; Yang, R.; Lee, H.; Wang, D.; Ren, Z.; Fleurial, J. P.; Gogna, P. New Directions for Low-Dimensional Thermoelectric Materials. *Adv. Mater.* **2007**, *19* (8), 1043–1053. https://doi.org/10.1002/adma.200600527.

(9) Poudel, B.; Hao, Q.; Ma, Y.; Lan, Y.; Minnich, A.; Yu, B.; Yan, X.; Wang, D.; Muto, A.; Vashaee, D.; Chen, X.; Liu, J.; Dresselhaus, M. S.; Chen, G.; Ren, Z. High-Thermoelectric Performance of Nanostructured Bismuth Antimony Telluride Bulk Alloys. *Science* **2008**, *320* (5876), 634–638. https://doi.org/10.1126/science.1156446.

(10) Li, D.; Luo, C.; Chen, Y.; Feng, D.; Gong, Y.; Pan, C.; He, J. High Performance Polymer Thermoelectric Composite Achieved by Carbon-Coated Carbon Nanotubes Network. *ACS Appl. Energy Mater.* **2019**, *2* (4), 2427–2434. https://doi.org/10.1021/acsaem.9b00334.

(11) Biswas, K.; He, J.; Blum, I. D.; Wu, C. I.; Hogan, T. P.; Seidman, D. N.; Dravid, V. P.; Kanatzidis, M. G. High-Performance Bulk Thermoelectrics with All-Scale Hierarchical Architectures. *Nature* **2012**, *489* (7416), 414–418. https://doi.org/10.1038/nature11439.

(12) Hochbaum, A. I.; Chen, R.; Delgado, R. D.; Liang, W.; Garnett, E. C.; Najarian, M.; Majumdar, A.; Yang, P. Enhanced Thermoelectric Performance of Rough Silicon Nanowires. *Nature* **2008**, *451* (7175), 163–167. https://doi.org/10.1038/nature06381.

(13) Sun, H.; Zhao, L.-D.; Kanatzidis, M. G.; Wolverton, C.; Uher, C.; Tan, G.; Lo, S.-H.; Dravid, V. P.; Zhang, Y. Ultralow Thermal Conductivity and High Thermoelectric Figure of Merit in SnSe Crystals. *Nature* **2014**, *508* (7496), 373–377. https://doi.org/10.1038/nature13184.

(14) Goldsmid, H. J.; Douglas, R. W. The Use of Semiconductors in Thermoelectric Refrigeration. *Br. J. Appl. Phys.* **1954**, *5* (11), 386–390. https://doi.org/10.1088/0508-3443/5/11/303.

(15) Weller, D. P.; Stevens, D. L.; Kunkel, G. E.; Ochs, A. M.; Holder, C. F.; Morelli, D. T.; Anderson, M. E. Thermoelectric Performance of Tetrahedrite Synthesized by a Modified Polyol Process. *Chem. Mater.* **2017**, *29* (4), 1656–1664. https://doi.org/10.1021/acs.chemmater.6b04950.

(16) Liu, W.; Yan, X.; Chen, G.; Ren, Z. Recent Advances in Thermoelectric Nanocomposites. *Nano Energy* **2012**, *1* (1), 42–56. https://doi.org/10.1016/j.nanoen.2011.10.001.

(17) Feng, J.; Zhu, W.; Deng, Y.; Song, Q.; Zhang, Q. Enhanced Antioxidation and Thermoelectric Properties of the Flexible Screen-Printed Bi_2Te_3 Films through Interface Modification. *ACS Appl. Energy Mater.* **2019**, *2* (4), 2828–2836. https://doi.org/10.1021/acsaem.9b00178.

(18) Bounioux, C.; Díaz-Chao, P.; Campoy-Quiles, M.; Martín-González, M. S.; Goñi, A. R.; Yerushalmi-Rozen, R.; Müller, C. Thermoelectric Composites of Poly(3-Hexylthiophene) and Carbon Nanotubes with a Large Power Factor. *Energy Environ. Sci.* **2013**, *6* (3), 918–925. https://doi.org/10.1039/c2ee23406h.

(19) Zhang, K.; Zhang, Y.; Wang, S. Enhancing Thermoelectric Properties of Organic Composites through Hierarchical Nanostructures. *Sci. Rep.* **2013**, *3* (1), 3448. https://doi.org/10.1038/srep03448.

(20) Wang, H.; Yi, S. I.; Pu, X.; Yu, C. Simultaneously Improving Electrical Conductivity and Thermopower of Polyaniline Composites by Utilizing Carbon Nanotubes as High Mobility Conduits. *ACS Appl. Mater. Interfaces* **2015**, *7* (18), 9589–9597. https://doi.org/10.1021/acsami.5b01149.

(21) Decher, G.; Schlenoff, J. B. *Multilayer Thin Films*; Decher, G., Schlenoff, J. B., Eds.; Wiley-VCH Verlag GmbH & Co. KGaA: Weinheim, Germany, 2012. https://doi.org/10.1002/9783527646746.

(22) Dubas, S. T.; Schlenoff, J. B. Factors Controlling the Growth of Polyelectrolyte Multilayers. *Macromolecules* **1999**, *32* (24), 8153–8160. https://doi.org/10.1021/ma981927a.

(23) Xiang, F.; Ward, S. M.; Givens, T. M.; Grunlan, J. C. Structural Tailoring of Hydrogen-Bonded Poly(Acrylic Acid)/Poly(Ethylene Oxide) Multilayer Thin Films for Reduced Gas Permeability. *Soft Matter* **2015**, *11* (43), 1001-1007. https://doi.org/10.1039/c4sm02363c

(24) Cho, C.; Culebras, M.; Wallace, K. L.; Song, Y.; Holder, K.; Hsu, J. H.; Yu, C.; Grunlan, J. C. Stable N-Type Thermoelectric Multilayer Thin Films with High Power Factor from Carbonaceous Nanofillers. *Nano Energy* **2016**, *28*, 426–432. https://doi.org/10.1016/j.nanoen.2016.08.063.

(25) Bergbreiter, D. E.; Chance, B. S. "Click"-Based Covalent Layer-by-Layer Assembly on Polyethylene Using Water-Soluble Polymeric Reagents. *Macromolecules* **2007**, *40* (15), 5337–5343. https://doi.org/10.1021/ma0701134.

(26) Blomberg, E.; Poptoshev, E.; Claesson, P. M.; Caruso, F. Surface Interactions during Polyelectrolyte Multilayer Buildup. 1. Interactions and Layer Structure in Dilute Electrolyte Solutions. *Langmuir* **2004**, *20* (13), 5432–5438. https://doi.org/10.1021/la049636k.

(27) Borges, J.; Mano, J. F. Molecular Interactions Driving the Layer-by-Layer Assembly of Multilayers. *Chem. Rev.* **2014**, *114* (18), 8883–8942. https://doi.org/10.1021/cr400531v.

(28) Cho, C.; Stevens, B.; Hsu, J. H.; Bureau, R.; Hagen, D. A.; Regev, O.; Yu, C.; Grunlan, J. C. Completely Organic Multilayer Thin Film with Thermoelectric Power Factor Rivaling Inorganic Tellurides. *Adv. Mater.* **2015**, *27* (19), 2996–3001. https://doi.org/10.1002/adma.201405738.

(29) Cho, C.; Wallace, K. L.; Tzeng, P.; Hsu, J. H.; Yu, C.; Grunlan, J. C. Outstanding Low Temperature Thermoelectric Power Factor from Completely Organic Thin Films Enabled by Multidimensional Conjugated Nanomaterials. *Adv. Energy Mater.* **2016**, *6* (7), 1502168. https://doi.org/10.1002/aenm.201502168.

(30) Brandt, J. *Snap-21 Program, Phase Ii*; 1968.

(31) Panson, A. J.; Johnston, W. D. A Study of Substituted MnTe. *J. Inorg. Nucl. Chem.* **1964**, *26*, 705–710.

(32) Saito, R.; Fujita, M.; Dresselhaus, G.; Dresselhaus, M. S. Electronic Structure of Graphene Tubules Based on C60. *Phys. Rev. B* **1992**, *46* (3), 1804–1811. https://doi.org/10.1103/PhysRevB.46.1804.

(33) Hicks, L.; Dresselhaus, M. S. Thermoelectric Figure of Merit of a One-Dimensional Conductor. *Phys. Rev. B* **1993**, *47* (24), 8–11. https://doi.org/10.1103/PhysRevB.47.16631

(34) Hicks, L. D.; Dresselhaus, M. S. Effect of Quantum-Well Structures on the Thermoelectric Figure of Merit. *Phys. Rev. B* **1993**, *47* (19), 12727–12731. https://doi.org/10.1103/PhysRevB.47.12727

(35) Vineis, C. J.; Shakouri, A.; Majumdar, A.; Kanatzidis, M. G. Nanostructured Thermoelectrics: Big Efficiency Gains from Small Features. *Adv. Mater.* **2010**, *22* (36), 3970–3980. https://doi.org/10.1002/adma.201000839.

(36) Leal, F. I.; Rego, E. E.; de Oliveira Ribeiro, C. Levelized Cost Analysis of Thermoelectric Generation in Brazil: A Comparative Economic and Policy Study with Environmental Implications. *J. Nat. Gas Sci. Eng.* **2017**, *44*, 191–201. https://doi.org/10.1016/j.jngse.2017.04.017.

(37) Heremans, J. P.; Dresselhaus, M. S.; Bell, L. E.; Morelli, D. T. When Thermoelectrics Reached the Nanoscale. *Nat. Nanotechnol.* **2013**, *8* (7), 471–473. https://doi.org/10.1038/nnano.2013.129.

(38) Seebeck, T. J. Ueber Die Magnetische Polarisation Der Metalle Und Erze Durch Temperatur-Differenz. *Ann. Phys.* **1826**, *82* (2), 133–160. https://doi.org/10.1002/andp.18260820202.

(39) DiSalvo, F. J. Thermoelectric Cooling and Power Generation. *Science* **1999**, *285* (5428), 703–706. https://doi.org/10.1126/science.285.5428.703.

(40) Goldsmid, H. J. *Thermoelectric Refrigeration*; Springer US: Boston, MA, 1964. https://doi.org/10.1007/978-1-4899-5723-8.

(41) Shakouri, A. Recent Developments in Semiconductor Thermoelectric Physics and Materials. *Annu. Rev. Mater. Res.* **2011**, *41* (1), 399–431. https://doi.org/10.1146/annurev-matsci-062910-100445.

(42) Poehler, T. O.; Katz, H. E. Innovative Thermoelectric Materials. In *Innovative Thermoelectric Materials*; Imperial College Press, 2016; pp 1–37. https://doi.org/10.1142/9781783266067_0001.

(43) Snyder, G. J.; Toberer, E. S. Complex Thermoelectric Materials. *Nat. Mater.* **2008**, *7* (2), 105–114. https://doi.org/10.1038/nmat2090.

(44) Rowe, D. M. *CRC Handbook of Thermoelectrics*; Rowe, D. M., Ed.; CRC Press, 2018. https://doi.org/10.1201/9781420049718.

(45) Fritzsche, H. A General Expression for the Thermoelectric Power. *Solid State Commun.* **1971**. https://doi.org/10.1016/0038-1098(71)90096-2.

(46) Gersten, J. I.; Smith, F. W. *The Physics and Chemistry of Materials*; 2001. https://doi.org/10.1063/1.1506755.

(47) Mott, N. F.; Davis, E. A. *Electronic Processes in Non-Crystalline Materials*, 2nd ed.; Clarendon: Oxford, U. K., 1979. https://doi.org/10.1080/00107514.2014.933254

(48) Smits, F. M. Measurement of Sheet Resistivities with the Four-Point Probe. *Bell Syst. Tech. J.* **1958**, *37* (3), 711–718. https://doi.org/10.1002/j.1538-7305.1958.tb03883.x.

(49) Park, Y. T.; Ham, A. Y.; Grunlan, J. C. High Electrical Conductivity and Transparency in Deoxycholate-Stabilized Carbon Nanotube Thin Films. *J. Phys. Chem. C* **2010**, *114* (14), 6325–6333. https://doi.org/10.1021/jp911985g.

(50) Park, Y. T.; Ham, A. Y.; Yang, Y. H.; Grunlan, J. C. Fully Organic ITO Replacement through Acid Doping of Double-Walled Carbon Nanotube Thin Film Assemblies. *RSC Adv.* **2011**, *1* (4), 662–671. https://doi.org/10.1039/c1ra00225b.

(51) Moriarty, G. P.; Briggs, K.; Stevens, B.; Yu, C.; Grunlan, J. C. Fully Organic Nanocomposites with High Thermoelectric Power Factors by Using a Dual-Stabilizer Preparation. *Energy Technol.* **2013**, *1* (4), 265–272. https://doi.org/10.1002/ente.201300018.

(52) Nolas, G. S.; Morelli, D. T.; Tritt, T. M. Skutterudites: A Phonon-Glass-Electron Crystal Approach to Advanced Thermoelectric Energy Conversion Applications. *Annu. Rev. Mater. Sci.* **1999**, *29* (1), 89–116. https://doi.org/10.1146/annurev.matsci.29.1.89.

(53) Wu, L.; Meng, Q.; Jooss, C.; Zheng, J.-C.; Inada, H.; Su, D.; Li, Q.; Zhu, Y. Origin of Phonon Glass-Electron Crystal Behavior in Thermoelectric Layered Cobaltate. *Adv. Funct. Mater.* **2013**, *23* (46), 5728–5736. https://doi.org/10.1002/adfm.201301098.

(54) Mao, J.; Liu, Z.; Ren, Z. Size Effect in Thermoelectric Materials. *npj Quantum Mater.* **2016**, *1* (1), 16028. https://doi.org/10.1038/npjquantmats.2016.28.

(55) Jorio, A.; Saito, R.; Hafner, J. H.; Lieber, C. M.; Hunter, M.; McClure, T.; Dresselhaus, G.; Dresselhaus, M. S. Structural (n, m) Determination of Isolated Single-Wall Carbon Nanotubes by Resonant Raman Scattering. *Phys. Rev. Lett.* **2001**, *86* (6), 1118–1121. https://doi.org/10.1103/PhysRevLett.86.1118.

(56) Tang, J.; Wang, H.-T.; Lee, D. H.; Fardy, M.; Huo, Z.; Russell, T. P.; Yang, P. Holey Silicon as an Efficient Thermoelectric Material. *Nano Lett.* **2010**, *10* (10), 4279–4283. https://doi.org/10.1021/nl102931z.

(57) Qian, F.; Li, Y.; Gradečak, S.; Park, H.-G.; Dong, Y.; Ding, Y.; Wang, Z. L.; Lieber, C. M. Multi-Quantum-Well Nanowire Heterostructures for Wavelength-Controlled Lasers. *Nat. Mater.* **2008**, *7* (9), 701–706. https://doi.org/10.1038/nmat2253.

(58) Lewis, J. E.; Rodot, H.; Haen, P. The Low-Temperature Thermoelectric Power and Thermal Conductivity of GeTe and of Some GeTe-MnTe Alloys. *Phys. Status Solidi* **1968**, *29* (2), 743–754. https://doi.org/10.1002/pssb.19680290224.

(59) Rogers, L. M. The Hall Mobility and Thermoelectric Power of P-Type Lead Telluride. *Br. J. Appl. Phys.* **1967**, *18* (9), 1227–1235. https://doi.org/10.1088/0508-3443/18/9/302.

(60) Greenaway, D. L.; Harbeke, G. Band Structure of Bismuth Telluride, Bismuth Selenide and Their Respective Alloys. *J. Phys. Chem. Solids* **1965**, *26* (10), 1585–1604. https://doi.org/10.1016/0022-3697(65)90092-2.

(61) Zhao, H.; Sui, J.; Tang, Z.; Lan, Y.; Jie, Q.; Kraemer, D.; McEnaney, K.; Guloy, A.; Chen, G.; Ren, Z. High Thermoelectric Performance of MgAgSb-Based Materials. *Nano Energy* **2014**, *7*, 97–103. https://doi.org/10.1016/j.nanoen.2014.04.012.

(62) He, R.; Kraemer, D.; Mao, J.; Zeng, L.; Jie, Q.; Lan, Y.; Li, C.; Shuai, J.; Kim, H. S.; Liu, Y.; Broido, D.; Chu, C-W.; Chen, G.; Ren, Z. Achieving High Power Factor and Output Power Density in P-Type Half-Heuslers $Nb_{1-x}Ti_xFeSb$. *Proc. Natl. Acad. Sci.* **2016**, *113* (48), 13576–13581. https://doi.org/10.1073/pnas.1617663113.

(63) Takas, N. J.; Sahoo, P.; Misra, D.; Zhao, H.; Henderson, N. L.; Stokes, K.; Poudeu, P. F. P. Effects of Ir Substitution and Processing Conditions on Thermoelectric Performance of P-Type $Zr_{0.5}Hf_{0.5}Co_{1-x}Ir_xSb_{0.99}Sn_{0.01}$ Half-Heusler Alloys. *J. Electron. Mater.* **2011**, *40* (5), 662–669. https://doi.org/10.1007/s11664-010-1501-0.

(64) Yan, X.; Joshi, G.; Liu, W.; Lan, Y.; Wang, H.; Lee, S.; Simonson, J. W.; Poon, S. J.; Tritt, T. M.; Chen, G.; Ren, Z. F. Enhanced Thermoelectric Figure of Merit of P-Type Half-Heuslers. *Nano Lett.* **2011**, *11* (2), 556–560. https://doi.org/10.1021/nl104138t.

(65) Zhu, H.; Mao, J.; Li, Y.; Sun, J.; Wang, Y.; Zhu, Q.; Li, G.; Song, Q.; Zhou, J.; Fu, Y.; et al. Discovery of TaFeSb-Based Half-Heuslers with High Thermoelectric Performance. *Nat. Commun.* **2019**, *10* (1), 270. https://doi.org/10.1038/s41467-018-08223-5.

(66) He, T.; Chen, J.; Rosenfeld, H. D.; Subramanian, M. A. Thermoelectric Properties of Indium-Filled Skutterudites. *Chem. Mater.* **2006**, *18* (3), 759–762. https://doi.org/10.1021/cm052055b.

(67) Lu, X.; Morelli, D. T.; Xia, Y.; Zhou, F.; Ozolins, V.; Chi, H.; Zhou, X.; Uher, C. High Performance Thermoelectricity in Earth-Abundant Compounds Based on Natural Mineral Tetrahedrites. *Adv. Energy Mater.* **2013**, *3* (3), 342–348. https://doi.org/10.1002/aenm.201200650.

(68) Weller, D. P.; Morelli, D. T. Rapid Synthesis of Zinc and Nickel Co-Doped Tetrahedrite Thermoelectrics by Reactive Spark Plasma Sintering and Mechanical Alloying. *J. Alloys Compd.* **2017**, *710*, 794–799. https://doi.org/10.1016/j.jallcom.2017.03.272.

(69) Lu, X.; Morelli, D. T. Natural Mineral Tetrahedrite as a Direct Source of Thermoelectric Materials. *Phys. Chem. Chem. Phys.* **2013**, *15* (16), 5762–5766. https://doi.org/10.1039/c3cp50920f.

(70) Li, D.; Zhao, H.; Li, S.; Wei, B.; Shuai, J.; Shi, C.; Xi, X.; Sun, P.; Meng, S.; Gu, L.; Ren, Z.; Chen, X. Atomic Disorders Induced by Silver and Magnesium Ion Migrations Favor High Thermoelectric Performance in α-MgAgSb-Based Materials. *Adv. Funct. Mater.* **2015**, *25* (41), 6478–6488. https://doi.org/10.1002/adfm.201503022.

(71) Harman, T. C. Quantum Dot Superlattice Thermoelectric Materials and Devices. *Science.* **2002**, *297* (5590), 2229–2232. https://doi.org/10.1126/science.1072886.

(72) Winder, E. J.; Ellis, A. B.; Lisensky, G. C. Thermoelectric Devices: Solid-State Refrigerators and Electrical Generators in the Classroom. *J. Chem. Educ.* **1996**, *73* (10), 940. https://doi.org/10.1021/ed073p940.

(73) Kee, S.; Kim, N.; Kim, B. S.; Park, S.; Jang, Y. H.; Lee, S. H.; Kim, J.; Kim, J.; Kwon, S.; Lee, K. Controlling Molecular Ordering in Aqueous Conducting Polymers Using Ionic Liquids. *Adv. Mater.* **2016**, *28* (39), 8625–8631. https://doi.org/10.1002/adma.201505473.

(74) Xu, K.; Sun, H.; Ruoko, T. P.; Wang, G.; Kroon, R.; Kolhe, N. B.; Puttisong, Y.; Liu, X.; Fazzi, D.; Shibata, K.; Yang, C-Y.; Sun, N.; Persson, G.; Yankovich, A. B.; Olsson, E.; Yoshida, H.; Chen, W. M.; Fahlman, M.; Kemerink, M.; Jenekhe, S. A.; Müller, C.; Berggren, M.; Fabiano, S. Ground-State Electron Transfer in All-Polymer Donor–Acceptor Heterojunctions. *Nat. Mater.* **2020**, *19*, 738–744. https://doi.org/10.1038/s41563-020-0618-7.

(75) Liu, J.; Ye, G.; van der Zee, B.; Dong, J.; Qiu, X.; Liu, Y.; Portale, G.; Chiechi, R. C.; Koster, L. J. A. N-Type Organic Thermoelectrics of Donor–Acceptor Copolymers: Improved Power Factor by Molecular Tailoring of the Density of States. *Adv. Mater.* **2018**, *30* (44), 1804290. https://doi.org/10.1002/adma.201804290.

(76) Cowen, L. M.; Atoyo, J.; Carnie, M. J.; Baran, D.; Schroeder, B. C. Review—Organic Materials for Thermoelectric Energy Generation. *ECS J. Solid State Sci. Technol.* **2017**, *6* (3), N3080–N3088. https://doi.org/10.1149/2.0121703jss.

(77) McDearmon, B.; Page, Z. A.; Chabinyc, M. L.; Hawker, C. J. Organic Electronics by Design: The Power of Minor Atomic and Structural Changes. *J. Mater. Chem. C* **2018**, *6* (14), 3564–3572. https://doi.org/10.1039/C7TC05052F.

(78) Thomas, E. M.; Davidson, E. C.; Katsumata, R.; Segalman, R. A.; Chabinyc, M. L. Branched Side Chains Govern Counterion Position and Doping Mechanism in Conjugated Polythiophenes. *ACS Macro Lett.* **2018**, *7* (12), 1492–1497. https://doi.org/10.1021/acsmacrolett.8b00778.

(79) Poehler, T. O.; Katz, H. E. Prospects for Polymer-Based Thermoelectrics: State of the Art and Theoretical Analysis. *Energy Environ. Sci.* **2012**, *5* (8), 8110–8115. https://doi.org/10.1039/c2ee22124a.

(80) Paasch, G.; Lindner, T.; Scheinert, S. Variable Range Hopping as Possible Origin of a Universal Relation between Conductivity and Mobility in Disordered Organic Semiconductors. *Synth. Met.* **2002**, *132* (1), 97–104. https://doi.org/10.1016/S0379-6779(02)00236-9.

(81) Luo, S.; Liu, T.; Benjamin, S. M.; Brooks, J. S. Variable Range Hopping in Single-Wall Carbon Nanotube Thin Films: A Processing-Structure-Property Relationship Study. *Langmuir* **2013**, *29* (27), 8694–8702. https://doi.org/10.1021/la401264r.

(82) Fan, Z.; Li, P.; Du, D.; Ouyang, J. Significantly Enhanced Thermoelectric Properties of PEDOT:PSS Films through Sequential Post-Treatments with Common Acids and Bases. *Adv. Energy Mater.* **2017**, *7* (8), 1602116. https://doi.org/10.1002/aenm.201602116.

(83) Nogami, Y.; Kaneko, H.; Ishiguro, T.; Takahashi, A.; Tsukamoto, J.; Hosoito, N. On the Metallic States in Highly Conducting Iodine-Doped Polyacetylene. *Solid State Commun.* **1990**, *76* (5), 583–586. https://doi.org/10.1016/0038-1098(90)90093-Q.

(84) Kaiser, A. B. Electronic Transport Properties of Conducting Polymers and Carbon Nanotubes. *Reports Prog. Phys.* **2001**, *64* (1), 1–49. https://doi.org/10.1088/0034-4885/64/1/201.

(85) Choi, K.; Kim, S. L.; Yi, S.; Hsu, J.-H.; Yu, C. Promoting Dual Electronic and Ionic Transport in PEDOT by Embedding Carbon Nanotubes for Large Thermoelectric Responses. *ACS Appl. Mater. Interfaces* **2018**, *10* (28), 23891–23899. https://doi.org/10.1021/acsami.8b06850.

(86) Bubnova, O.; Khan, Z. U.; Wang, H.; Braun, S.; Evans, D. R.; Fabretto, M.; Hojati-Talemi, P.; Dagnelund, D.; Arlin, J.-B.; Geerts, Y. H.; Desbief, S.; Breiby, D. W.; Andreasen, J. W.; Lazzaroni, R.; Chen, W. M.; Zozoulenko, I.; Fahlman, M.; Murphy, P. J.; Berggren, M.; Cirspin, X. Semi-Metallic Polymers. *Nat. Mater.* **2014**, *13* (2), 190–194. https://doi.org/10.1038/nmat3824.

(87) Lee, S. H.; Park, H.; Kim, S.; Son, W.; Cheong, I. W.; Kim, J. H. Transparent and Flexible Organic Semiconductor Nanofilms with Enhanced Thermoelectric Efficiency. *J. Mater. Chem. A* **2014**, *2* (20), 7288–7294. https://doi.org/10.1039/C4TA00700J.

(88) Bubnova, O.; Berggren, M.; Crispin, X. Tuning the Thermoelectric Properties of Conducting Polymers in an Electrochemical Transistor. *J. Am. Chem. Soc.* **2012**, *134* (40), 16456–16459. https://doi.org/10.1021/ja305188r.

(89) Park, T.; Park, C.; Kim, B.; Shin, H.; Kim, E. Flexible PEDOT Electrodes with Large Thermoelectric Power Factors to Generate Electricity by the Touch of Fingertips. *Energy Environ. Sci.* **2013**, *6* (3), 788–792. https://doi.org/10.1039/c3ee23729j.

(90) Zhu, Z.; Liu, C.; Jiang, F.; Xu, J.; Liu, E. Effective Treatment Methods on PEDOT:PSS to Enhance Its Thermoelectric Performance. *Synth. Met.* **2017**, *225*, 31–40. https://doi.org/10.1016/j.synthmet.2016.11.011.

(91) Kim, G.-H.; Shao, L.; Zhang, K.; Pipe, K. P. Engineered Doping of Organic Semiconductors for Enhanced Thermoelectric Efficiency. *Nat. Mater.* **2013**, *12* (8), 719–723. https://doi.org/10.1038/nmat3635.

(92) Fan, Z.; Du, D.; Yu, Z.; Li, P.; Xia, Y.; Ouyang, J. Significant Enhancement in the Thermoelectric Properties of PEDOT:PSS Films through a Treatment with Organic Solutions of Inorganic Salts. *ACS Appl. Mater. Interfaces* **2016**, *8* (35), 23204–23211. https://doi.org/10.1021/acsami.6b07234.

(93) Taggart, D. K.; Yang, Y.; Kung, S.-C.; McIntire, T. M.; Penner, R. M. Enhanced Thermoelectric Metrics in Ultra-Long Electrodeposited PEDOT Nanowires. *Nano Lett.* **2011**, *11* (1), 125–131. https://doi.org/10.1021/nl103003d.

(94) Liu, C.; Lu, B.; Yan, J.; Xu, J.; Yue, R.; Zhu, Z.; Zhou, S.; Hu, X.; Zhang, Z.; Chen, P. Highly Conducting Free-Standing Poly(3,4-Ethylenedioxythiophene)/Poly(Styrenesulfonate) Films with Improved Thermoelectric Performances. *Synth. Met.* **2010**, *160* (23–24), 2481–2485. https://doi.org/10.1016/j.synthmet.2010.09.031.

(95) Xia, Y.; Ouyang, J. Salt-Induced Charge Screening and Significant Conductivity Enhancement of Conducting Poly(3,4-Ethylenedioxythiophene): Poly(Styrenesulfonate). *Macromolecules* **2009**, *42* (12), 4141–4147. https://doi.org/10.1021/ma900327d.

(96) Zhang, B.; Sun, J.; Katz, H. E.; Fang, F.; Opila, R. L. Promising Thermoelectric Properties of Commercial PEDOT:PSS Materials and Their Bi_2Te_3 Powder Composites. *ACS Appl. Mater. Interfaces* **2010**, *2* (11), 3170–3178. https://doi.org/10.1021/am100654p.

(97) See, K. C.; Feser, J. P.; Chen, C. E.; Majumdar, A.; Urban, J. J.; Segalman, R. A. Water-Processable Polymer−Nanocrystal Hybrids for Thermoelectrics. *Nano Lett.* **2010**, *10* (11), 4664–4667. https://doi.org/10.1021/nl102880k.

(98) Bergman, D. J.; Levy, O. Thermoelectric Properties of a Composite Medium. *J. Appl. Phys.* **1991**, *70* (11), 6821–6833. https://doi.org/10.1063/1.349830.

(99) Coates, N. E.; Yee, S. K.; McCulloch, B.; See, K. C.; Majumdar, A.; Segalman, R. A.; Urban, J. J. Effect of Interfacial Properties on Polymer-Nanocrystal Thermoelectric Transport. *Adv. Mater.* **2013**, *25* (11), 1629–1633. https://doi.org/10.1002/adma.201203915.

(100) Hsu, I.-K.; Pettes, M. T.; Bushmaker, A.; Aykol, M.; Shi, L.; Cronin, S. B. Optical Absorption and Thermal Transport of Individual Suspended Carbon Nanotube Bundles. *Nano Lett.* **2009**, *9* (2), 590–594. https://doi.org/10.1021/nl802737q.

(101) Mintmire, J. W.; Dunlap, B. I.; White, C. T. Are Fullerene Tubules Metallic? *Phys. Rev. Lett.* **1992**, *68* (5), 631–634. https://doi.org/10.1103/PhysRevLett.68.631.

(102) Kiang, C. H.; Devries, M. S.; Gorman, G.; Savoy, R.; Bethune, D. S.; Klang, C. H.; de-Vries, M. S.; Vazquez, J.; Beyers, R. Cobalt-Catalysed Growth of Carbon Nanotubes with Single-Atomic-Layer Walls. *Nature* **1993**, *363* (6430), 605–607. https://doi.org/10.1038/363605a0

(103) Iijima, S.; Ichihashi, T. Single-Shell Carbon Nanotubes of 1-Nm Diameter. *Nature* **1993**, *363* (6430), 603–605. https://doi.org/10.1038/363603a0.

(104) Odom, T. W.; Huang, J. L.; Kim, P.; Lieber, C. M. Atomic Structure and Electronic Properties of Single-Walled Carbon Nanotubes. *Nature* **1998**, *391* (6662), 62–64. https://doi.org/10.1038/34145.

(105) O'Connell, M. J. Band Gap Fluorescence from Individual Single-Walled Carbon Nanotubes. *Science.* **2002**, *297* (5581), 593–596. https://doi.org/10.1126/science.1072631.

(106) Kim, S. M.; Kim, K. K.; Jo, Y. W.; Park, M. H.; Chae, S. J.; Duong, D. L.; Yang, C. W.; Kong, J.; Lee, Y. H. Role of Anions in the AuCl3 -Doping of Carbon Nanotubes. *ACS Nano* **2011**, *5* (2), 1236–1242. https://doi.org/10.1021/nn1028532.

(107) Diao, S.; Blackburn, J. L.; Hong, G.; Antaris, A. L.; Chang, J.; Wu, J. Z.; Zhang, B.; Cheng, K.; Kuo, C. J.; Dai, H. Fluorescence Imaging in Vivo at Wavelengths beyond 1500 Nm. *Angew. Chemie - Int. Ed.* **2015**, *54* (49), 14758–14762. https://doi.org/10.1002/anie.201507473.

(108) Arnold, M. S.; Blackburn, J. L.; Crochet, J. J.; Doorn, S. K.; Duque, J. G.; Mohite, A.; Telg, H. Recent Developments in the Photophysics of Single-Walled Carbon Nanotubes for Their Use as Active and Passive Material Elements in Thin Film Photovoltaics. *Phys. Chem. Chem. Phys.* **2013**, *15* (36), 14896–14918. https://doi.org/10.1039/c3cp52752b.

(109) Avery, A. D.; Zhou, B. H.; Lee, J.; Lee, E.-S.; Miller, E. M.; Ihly, R.; Wesenberg, D.; Mistry, K. S.; Guillot, S. L.; Zink, B. L.; Kim, Y-H.; Blackburn, J. L.; Ferguson, A. J. Tailored Semiconducting Carbon Nanotube Networks with Enhanced Thermoelectric Properties. *Nat. Energy* **2016**, *1* (4), 16033. https://doi.org/10.1038/nenergy.2016.33.

(110) Zong, P.; Liang, J.; Zhang, P.; Wan, C.; Wang, Y.; Koumoto, K. Graphene-Based Thermoelectrics. *ACS Appl. Energy Mater.* **2020**, *3* (3), 2224–2239. https://doi.org/10.1021/acsaem.9b02187.

(111) Labulo, A. H.; Martincigh, B. S.; Omondi, B.; Nyamori, V. O. Advances in Carbon Nanotubes as Efficacious Supports for Palladium-Catalysed Carbon–Carbon Cross-Coupling Reactions. *J. Mater. Sci.* **2017**, *52* (16), 9225–9248. https://doi.org/10.1007/s10853-017-1128-0.

(112) Yu, C.; Choi, K.; Yin, L.; Grunlan, J. C. Light-Weight Flexible Carbon Nanotube Based Organic Composites with Large Thermoelectric Power Factors. *ACS Nano* **2011**, *5* (10), 7885–7892. https://doi.org/10.1021/nn202868a.

(113) Yu, C.; Kim, Y. S.; Kim, D.; Grunlan, J. C. Thermoelectric Behavior of Segregated-Network Polymer Nanocomposites. *Nano Lett.* **2008**, *8* (12), 4428–4432. https://doi.org/10.1021/nl802345s.

(114) Kim, D.; Kim, Y.; Choi, K.; Grunlan, J. C.; Yu, C. Improved Thermoelectric Behavior of Nanotube-Filled Polymer Composites with Poly(3,4-Ethylenedioxythiophene) Poly(Styrenesulfonate). *ACS Nano* **2010**, *4* (1), 513–523. https://doi.org/10.1021/nn9013577.

(115) Yang, X.; Hu, J.; Chen, S.; He, J. Understanding the Percolation Characteristics of Nonlinear Composite Dielectrics. *Sci. Rep.* **2016**, *6*, 30597. https://doi.org/10.1038/srep30597.

(116) Straley, J. P. Critical Phenomena in Resistor Networks. *J. Phys. C Solid State Phys.* **1976**, *9*, 783–786. https://doi.org/10.1088/0022-3719/9/5/017.

(117) Miriyala, S. M.; Kim, Y. S.; Liu, L.; Grunlan, J. C. Segregated Networks of Carbon Black in Poly(Vinyl Acetate) Latex: Influence of Clay on the Electrical and Mechanical Behavior. *Macromol. Chem. Phys.* **2008**, *209* (23), 2399–2409. https://doi.org/10.1002/macp.200800384.

(118) Tsentalovich, D. E.; Headrick, R. J.; Mirri, F.; Hao, J.; Behabtu, N.; Young, C. C.; Pasquali, M. Influence of Carbon Nanotube Characteristics on Macroscopic Fiber Properties. *ACS Appl. Mater. Interfaces* **2017**, *9* (41), 36189–36198. https://doi.org/10.1021/acsami.7b10968.

(119) Abad, B.; Alda, I.; Díaz-Chao, P.; Kawakami, H.; Almarza, A.; Amantia, D.; Gutierrez, D.; Aubouy, L.; Martín-González, M. Improved Power Factor of Polyaniline Nanocomposites with Exfoliated Graphene Nanoplatelets (GNPs). *J. Mater. Chem. A* **2013**, *1* (35), 10450–10457. https://doi.org/10.1039/c3ta12105d.

(120) Wang, L.; Yao, Q.; Bi, H.; Huang, F.; Wang, Q.; Chen, L. Large Thermoelectric Power Factor in Polyaniline/Graphene Nanocomposite Films Prepared by Solution-Assistant Dispersing Method. *J. Mater. Chem. A* **2014**, *2* (29), 11107–11113. https://doi.org/10.1039/c4ta01541j.

(121) Ren, G.-K.; Butt, S.; Liu, Y.-C.; Lan, J.-L.; Lin, Y.-H.; Nan, C.-W.; Fu, F.; Tang, X.-F. Enhanced Thermoelectric Performance of Zn-Doped Oxyselenides: $BiCu_{1-x}Zn_xSeO$. *Phys. Status Solidi* **2014**, *211* (11), 2616–2620. https://doi.org/10.1002/pssa.201431347.

(122) Li, F.; Cai, K.; Shen, S.; Chen, S. Preparation and Thermoelectric Properties of Reduced Graphene Oxide/PEDOT:PSS Composite Films. *Synth. Met.* **2014**, *197*, 58–61. https://doi.org/10.1016/j.synthmet.2014.08.014.

(123) Ube, T.; Koyanagi, J.; Kosaki, T.; Fujimoto, K.; Yokozeki, T.; Ishiguro, T.; Nishio, K. Fabrication of Well-Isolated Graphene and Evaluation of Thermoelectric Performance of Polyaniline–Graphene Composite Film. *J. Mater. Sci.* **2019**, *54* (5), 3904–3913. https://doi.org/10.1007/s10853-018-3129-z.

(124) Xia, K.; Zhan, H.; Gu, Y. Graphene and Carbon Nanotube Hybrid Structure: A Review. *Procedia IUTAM* **2017**, *21*, 94–101. https://doi.org/10.1016/j.piutam.2017.03.042.

(125) Oh, J. Y.; Jun, G. H.; Jin, S.; Ryu, H. J.; Hong, S. H. Enhanced Electrical Networks of Stretchable Conductors with Small Fraction of Carbon Nanotube/Graphene Hybrid Fillers. *ACS Appl. Mater. Interfaces* **2016**, *8* (5), 3319–3325. https://doi.org/10.1021/acsami.5b11205.

(126) Yu, C.; Murali, A.; Choi, K.; Ryu, Y. Air-Stable Fabric Thermoelectric Modules Made of N- and P-Type Carbon Nanotubes. *Energy Environ. Sci.* **2012**, *5* (11), 9481–9486. https://doi.org/10.1039/c2ee22838f.

(127) Freeman, D. D.; Choi, K.; Yu, C. N-Type Thermoelectric Performance of Functionalized Carbon Nanotube-Filled Polymer Composites. *PLoS One* **2012**, *7* (11), e47822. https://doi.org/10.1371/journal.pone.0047822.

(128) Hong, C. T.; Lee, W.; Kang, Y. H.; Yoo, Y.; Ryu, J.; Cho, S. Y.; Jang, K.-S. Effective Doping by Spin-Coating and Enhanced Thermoelectric Power Factors in SWCNT/P3HT Hybrid Films. *J. Mater. Chem. A* **2015**, *3* (23), 12314–12319. https://doi.org/10.1039/C5TA02443A.

(129) Liu, J.; Sun, J.; Gao, L. Flexible Single-Walled Carbon Nanotubes/Polyaniline Composite Films and Their Enhanced Thermoelectric Properties. *Nanoscale* **2011**, *3* (9), 3616–3619. https://doi.org/10.1039/c1nr10386e.

(130) Iler, R. K. Multilayers of Colloidal Particles. *J. Colloid Interface Sci.* **1966**, *21* (6), 569–594. https://doi.org/10.1016/0095-8522(66)90018-3.

(131) Decher, G. Fuzzy Nanoassemblies: Toward Layered Polymeric Multicomposites. *Science.* **1997**, *277* (5330), 1232–1237. https://doi.org/10.1126/science.277.5330.1232.

(132) Fu, J.; Schlenoff, J. B. Driving Forces for Oppositely Charged Polyion Association in Aqueous Solutions: Enthalpic, Entropic, but Not Electrostatic. *J. Am. Chem. Soc.* **2016**, *138* (3), 980–990. https://doi.org/10.1021/jacs.5b11878.

(133) Lazar, S.; Carosio, F.; Davesne, A.-L.; Jimenez, M.; Bourbigot, S.; Grunlan, J. Extreme Heat Shielding of Clay/Chitosan Nanobrick Wall on Flexible Foam. *ACS Appl. Mater. Interfaces* **2018**, *10* (37), 31686–31696. https://doi.org/10.1021/acsami.8b10227.

(134) Yang, Y.-H.; Bolling, L.; Priolo, M. A.; Grunlan, J. C. Super Gas Barrier and Selectivity of Graphene Oxide-Polymer Multilayer Thin Films. *Adv. Mater.* **2013**, *25* (4), 503–508. https://doi.org/10.1002/adma.201202951.

(135) Yang, Y.; Haile, M.; Park, Y. T.; Malek, F. A.; Grunlan, J. C. Super Gas Barrier of All-Polymer Multilayer Thin Films. *Macromolecules* **2011**, *44* (6), 1450–1459. https://doi.org/10.1021/ma1026127.

(136) Kahn, A. Fermi Level, Work Function and Vacuum Level. *Mater. Horizons* **2016**, *3* (1), 7–10. https://doi.org/10.1039/c5mh00160a.

(137) Rivadulla, F.; Mateo-Mateo, C.; Correa-Duarte, M. A. Layer-by-Layer Polymer Coating of Carbon Nanotubes: Tuning of Electrical Conductivity in Random Networks. *J. Am. Chem. Soc.* **2010**, *132* (11), 3751–3755. https://doi.org/10.1021/ja910572b.

(138) Mistry, K. S.; Larsen, B. A.; Bergeson, J. D.; Barnes, T. M.; Teeter, G.; Engtrakul, C.; Blackburn, J. L. N-Type Transparent Conducting Films of Small Molecule and Polymer Amine Doped Single-Walled Carbon Nanotubes. *ACS Nano* **2011**, *5* (5), 3714–3723. https://doi.org/10.1021/nn200076r.

(139) Macleod, B. A.; Stanton, N. J.; Gould, I. E.; Wesenberg, D.; Ihly, R.; Owczarczyk, Z. R.; Hurst, K. E.; Fewox, C. S.; Folmar, C. N.; Holman Hughes, K.; Zink, B. L.; Blackburn, J. L.; Ferguson, A. J. Large N- and p-Type Thermoelectric Power Factors from Doped Semiconducting Single-Walled Carbon Nanotube Thin Films. *Energy Environ. Sci.* **2017**, *10*, 2168–2179. https://doi.org/10.1039/c7ee01130j.

(140) Cho, C.; Bittner, N.; Choi, W.; Hsu, J.; Yu, C.; Grunlan, J. C. Thermally Enhanced N-Type Thermoelectric Behavior in Completely Organic Graphene Oxide-Based Thin Films. *Adv. Electron. Mater.* **2019**, *5* (11), 1800465. https://doi.org/10.1002/aelm.201800465.

(141) Priolo, M. A.; Gamboa, D.; Holder, K. M.; Grunlan, J. C. Super Gas Barrier of Transparent Polymer-Clay Multilayer Ultrathin Films. *Nano Lett.* **2010**, *10* (12), 4970–4974. https://doi.org/10.1021/nl103047k.

(142) Zheng, Y.; Zeng, H.; Zhu, Q.; Xu, J. Recent Advances in Conducting Poly(3,4-Ethylenedioxythiophene):Polystyrene Sulfonate Hybrids for Thermoelectric Applications. *J. Mater. Chem. C* **2018**, *6* (33), 8858–8873. https://doi.org/10.1039/c8tc01900b.

(143) Wang, Y.; Yu, C.; Liu, G.; Sheng, M.; Deng, Y. An Effective Thermal Treatment Strategy for Thermoelectric Performance Enhancement in PANI/Te Nanorod Hybrid Film. *Mater. Lett.* **2018**, *229*, 293–296. https://doi.org/10.1016/j.matlet.2018.07.042.

(144) Pura, A.; Locs, J.; Berzina-Cimdina, L. Effect of Thermal Treatment on Thermoelectric Properties of Extruded TiO_2 Ceramics. *Key Eng. Mater.* **2014**, *604*, 249–253. https://doi.org/10.4028/www.scientific.net/KEM.604.249.

(145) Schrade, M.; Fjeld, H.; Finstad, T. G.; Norby, T. Electronic Transport Properties of $[Ca_2CoO_3{-}\delta]$ q$[CoO_2]$. *J. Phys. Chem. C* **2014**, *118* (6), 2908–2918. https://doi.org/10.1021/jp409581n.

(146) Delorme, F.; Martin, C. F.; Marudhachalam, P.; Guzman, G.; Ovono, D. O.; Fraboulet, O. Synthesis of Thermoelectric $Ca_3Co_4O_9$ Ceramics with High ZT Values from a CoIICoIII-Layered Double Hydroxide Precursor. *Mater. Res. Bull.* **2012**, *47* (11), 3287–3291. https://doi.org/10.1016/j.materresbull.2012.07.037.

(147) Wolfe, R. M. W.; Menon, A. K.; Fletcher, T. R.; Marder, S. R.; Reynolds, J. R.; Yee, S. K. Simultaneous Enhancement in Electrical Conductivity and Thermopower of N-Type NiETT/PVDF Composite Films by Annealing. *Adv. Funct. Mater.* **2018**, *28* (37), 1803275. https://doi.org/10.1002/adfm.201803275.

(148) Gamboa, D.; Priolo, M. A.; Ham, A.; Grunlan, J. C. Note: Influence of Rinsing and Drying Routines on Growth of Multilayer Thin Films Using Automated Deposition System. *Rev. Sci. Instrum.* **2010**, *81* (3), 036103. https://doi.org/10.1063/1.3310088.

(149) Wang, Q.; Schlenoff, J. B. The Polyelectrolyte Complex/Coacervate Continuum. *Macromolecules* **2014**, *47* (9), 3108–3116. https://doi.org/10.1021/ma500500q.

(150) Bieker, P.; Schönhoff, M. Linear and Exponential Growth Regimes of Multilayers of Weak Polyelectrolytes in Dependence on pH. *Macromolecules* **2010**, *43* (11), 5052–5059. https://doi.org/10.1021/ma1007489.

(151) Dresselhaus, M. S.; Dresselhaus, G.; Saito, R.; Jorio, A. Raman Spectroscopy of Carbon Nanotubes. *Phys. Rep.* **2005**, *409* (2), 47–99. https://doi.org/10.1016/j.physrep.2004.10.006.

(152) Fu, J.; Fares, H. M.; Schlenoff, J. B. Ion-Pairing Strength in Polyelectrolyte Complexes. *Macromolecules* **2017**, *50* (3), 1066–1074. https://doi.org/10.1021/acs.macromol.6b02445.

(153) G. Greczynski, Th. Kugler, M. Keil, W. Osikowicz, M. Fahlman, W. R. S. Photoelectron Spectroscopy of Thin Films of PEDOT-PSS Conjugated Polymer Blend: A Mini-Review and Some New Results. *J. Electron Spectroscpy Relat. Ph* **2001**, *121*, 1–17. https://doi.org/10.1016/S0368-2048(01)00323-1.

(154) Crispin, X.; Marciniak, S.; Osikowicz, W.; Zotti, G.; Denier van der Gon, A. W. ; Louwet, F.; Fahlman, M.; Groenendaal, L.; Schryver, F. D. E.; Salaneck, W. R. Conductivity, Morphology, Interfacial Chemistry, and Stability of Poly (3,4-Ethylene Dioxythiophene)– Poly (Styrene Sulfonate): A Photoelectron Spectroscopy Study. *J. Polym. Sci. B Polym. Phys.* **2003**, *41* (21), 2561–2583. https://doi.org/10.1002/polb.10659.

(155) Jin Bae, E.; Hun Kang, Y.; Jang, K. S.; Yun Cho, S. Enhancement of Thermoelectric Properties of PEDOT:PSS and Tellurium-PEDOT:PSS Hybrid Composites by Simple Chemical Treatment. *Sci. Rep.* **2016**, *6*, 18805. https://doi.org/10.1038/srep18805.

(156) Van der Auweraer, M.; Andersson, P.; Volodin, A.; van Haesendonck, C.; Berggren, M.; Crispin, X.; Crispin, A.; Salaneck, W. R.; Grim, P. C. M.; Jakobsson, F. L. E. The Origin of the High Conductivity of Poly(3,4-Ethylenedioxythiophene)−Poly(Styrenesulfonate) (PEDOT−PSS) Plastic Electrodes. *Chem. Mater.* **2006**, *18* (18), 4354–4360. https://doi.org/10.1021/cm061032+.

(157) Francis, S.; Varshney, L.; Sabharwal, S. Thermal Degradation Behavior of Radiation Synthesized Polydiallyldimethylammonium Chloride. *Eur. Polym. J.* **2007**, *43* (6), 2525–2531. https://doi.org/10.1016/j.eurpolymj.2007.03.009.

(158) Yi, C.; Wilhite, A.; Zhang, L.; Hu, R.; Chuang, S. S. C.; Zheng, J.; Gong, X. Enhanced Thermoelectric Properties of Poly(3,4-Ethylenedioxythiophene):Poly(Styrenesulfonate) by Binary Secondary Dopants. *ACS Appl. Mater. Interfaces* **2015**, *7* (17), 8984–8989. https://doi.org/10.1021/acsami.5b01960.

(159) Mazaheripour, A.; Majumdar, S.; Hanemann-Rawlings, D.; Thomas, E. M.; McGuiness, C.; D'Alencon, L.; Chabinyc, M. L.; Segalman, R. A. Tailoring the Seebeck Coefficient of PEDOT:PSS by Controlling Ion Stoichiometry in Ionic Liquid Additives. *Chem. Mater.* **2018**, *30* (14), 4816–4822. https://doi.org/10.1021/acs.chemmater.8b02114.

(160) Petsagkourakis, I.; Pavlopoulou, E.; Cloutet, E.; Chen, Y. F.; Liu, X.; Fahlman, M.; Berggren, M.; Crispin, X.; Dilhaire, S.; Fleury, G.; et al. Correlating the Seebeck Coefficient of Thermoelectric Polymer Thin Films to Their Charge Transport Mechanism. *Org. Electron.* **2018**, *52*, 335–341. https://doi.org/10.1016/j.orgel.2017.11.018.

(161) Kim, S. L.; Choi, K.; Tazebay, A.; Yu, C. Flexible Power Fabrics Made of Carbon Nanotubes for Harvesting Thermoelectricity. *ACS Nano* **2014**, *8* (3), 2377–2386. https://doi.org/10.1021/nn405893t.

(162) Sayed, S. Y.; Fereiro, J. A.; Yan, H.; McCreery, R. L.; Bergren, A. J. Charge Transport in Molecular Electronic Junctions: Compression of the Molecular Tunnel Barrier in the Strong Coupling Regime. *Proc. Natl. Acad. Sci.* **2012**, *109* (29), 11498–11503. https://doi.org/10.1073/pnas.1201557109.

(163) Tippireddy, S.; Chetty, R.; Naik, M. H.; Jain, M.; Chattopadhyay, K.; Mallik, R. C. Electronic and Thermoelectric Properties of Transition Metal Substituted Tetrahedrites. *J. Phys. Chem. C* **2018**, *122* (16), 8735–8749. https://doi.org/10.1021/acs.jpcc.7b12214.

(164) Raja Ashok, R. P.; Thomas, M. S.; Varughese, S. Multi-Region to Single Region Shear Thinning Transitions in Drying PEDOT:PSS Dispersions: Contributions from Charge Density Fluctuations. *Soft Matter* **2015**, *11* (43), 8441–8451. https://doi.org/10.1039/C5SM01000D.

(165) Liu, S.; Deng, H.; Zhao, Y.; Ren, S.; Fu, Q. The Optimization of Thermoelectric Properties in a PEDOT:PSS Thin Film through Post-Treatment. *RSC Adv.* **2015**, *5* (3), 1910–1917. https://doi.org/10.1039/C4RA09147G.

(166) Nardes, A. M.; Kemerink, M.; Janssen, R. A. J.; Bastiaansen, J. A. M.; Kiggen, N. M. M.; Langeveld, B. M. W.; van Breemen, A. J. J. M.; de Kok, M. M. Microscopic Understanding of the Anisotropic Conductivity of PEDOT:PSS Thin Films. *Adv. Mater.* **2007**, *19* (9), 1196–1200. https://doi.org/10.1002/adma.200602575.

(167) Gu, Y.; Huang, X.; Wiener, C. G.; Vogt, B. D.; Zacharia, N. S. Large-Scale Solvent Driven Actuation of Polyelectrolyte Multilayers Based on Modulation of Dynamic Secondary Interactions. *ACS Appl. Mater. Interfaces* **2015**, *7* (3), 1848–1858. https://doi.org/10.1021/am507573m.

(168) Stevens, D. L.; Parra, A.; Grunlan, J. C. Thermoelectric Performance Improvement of Polymer Nanocomposites by Selective Thermal Degradation. *ACS Appl. Energy Mater.* **2019**, *2* (8), 5975–5982. https://doi.org/10.1021/acsaem.9b01079.

(169) Nagels, P. Electronic Transport in Amorphous Semiconductors. In *Amorphous Semiconductors*; Brodsky, M. H., Ed.; Springer Berlin Heidelberg: Berlin, Heidelberg, 1985; pp 113–158. https://doi.org/10.1007/3-540-16008-6_159.

(170) Pham, T. A.; Mortuza, S. M. G.; Wood, B. C.; Lau, E. Y.; Ogitsu, T.; Buchsbaum, S. F.; Siwy, Z. S.; Fornasiero, F.; Schwegler, E. Salt Solutions in Carbon Nanotubes: The Role of Cation−π Interactions. *J. Phys. Chem. C* **2016**, *120* (13), 7332–7338. https://doi.org/10.1021/acs.jpcc.5b12245.

(171) Blackburn, J. L.; Kang, S. D.; Roos, M. J.; Norton-Baker, B.; Miller, E. M.; Ferguson, A. J. Intrinsic and Extrinsically Limited Thermoelectric Transport within Semiconducting Single-Walled Carbon Nanotube Networks. *Adv. Electron. Mater.* **2019**, *5* (11), 1800910. https://doi.org/10.1002/aelm.201800910.

(172) Duong, D. L.; Lee, I. H.; Kim, K. K.; Kong, J.; Lee, S. M.; Lee, Y. H. Carbon Nanotube Doping Mechanism in a Salt Solution and Hygroscopic Effect: Density Functional Theory. *ACS Nano* **2010**, *4* (9), 5430–5436. https://doi.org/10.1021/nn1011489.

(173) Stevens, D. L.; Gamage, G. A.; Ren, Z.; Grunlan, J. C. Salt Doping to Improve Thermoelectric Power Factor of Organic Nanocomposite Thin Films. *RSC Adv.* **2020**, *10* (20), 11800–11807. https://doi.org/10.1039/d0ra00763c.

(174) Ghostine, R. A.; Shamoun, R. F.; Schlenoff, J. B. Doping and Diffusion in an Extruded Saloplastic Polyelectrolyte Complex. *Macromolecules* **2013**, *46* (10), 4089–4094. https://doi.org/10.1021/ma4004083.

(175) Nakashima, Y.; Yamaguchi, R.; Toshimitsu, F.; Matsumoto, M.; Borah, A.; Staykov, A.; Islam, M. S.; Hayami, S.; Fujigaya, T. Air-Stable n-Type Single-Walled Carbon Nanotubes Doped with Benzimidazole Derivatives for Thermoelectric Conversion and Their Air-Stable Mechanism. *ACS Appl. Nano Mater.* **2019**, *2* (8), 4703–4710. https://doi.org/10.1021/acsanm.9b01174.

(176) Marcus, Y. On Enthalpies of Hydration, Ionization Potentials, and the Softness of Ions. *Thermochim. Acta* **1986**, *104*, 389–394. https://doi.org/10.1016/0040-6031(86)85213-3.

(177) Yu, H.; Whitfield, T. W.; Harder, E.; Lamoureux, G.; Vorobyov, I.; Anisimov, V. M.; MacKerell, A. D.; Roux, B. Simulating Monovalent and Divalent Ions in Aqueous Solution Using a Drude Polarizable Force Field. *J. Chem. Theory Comput.* **2010**, *6* (3), 774–786. https://doi.org/10.1021/ct900576a.

(178) Russ, B.; Robb, M. J.; Brunetti, F. G.; Miller, P. L.; Perry, E. E.; Patel, S. N.; Ho, V.; Chang, W. B.; Urban, J. J.; Chabinyc, M. L.; et al. Power Factor Enhancement in Solution-Processed Organic n-Type Thermoelectrics Through Molecular Design. *Adv. Mater.* **2014**, *26* (21), 3473–3477. https://doi.org/10.1002/adma.201306116.

(179) Wu, G.; Zhang, Z. G.; Li, Y.; Gao, C.; Wang, X.; Chen, G. Exploring High-Performance n-Type Thermoelectric Composites Using Amino-Substituted Rylene Dimides and Carbon Nanotubes. *ACS Nano* **2017**, *11* (6), 5746–5752. https://doi.org/10.1021/acsnano.7b01279.